Light-matter interaction in nanostructured materials

Kristensen, Philip Trøst

Publication date:
2010

Document Version
Publisher's PDF, also known as Version of record

Light-matter interaction in nanostructured materials

A dissertation
submitted to the Department of Photonics Engineering
at the Technical University of Denmark
in partial fulfillment of the requirements
for the degree of
philosophiæ doctor

Philip Trøst Kristensen
December 18, 2009

Light-matter interaction in nanostructured materials

Preface

The research described in this PhD thesis was carried out in the Theory and Signal Processing Group at DTU Fotonik in Lyngby, Denmark from October 2006 to December 2009 under the supervision of Professor Jesper Mørk and Associate Professor Peter Lodahl.

The close collaboration between theoretical and experimental activities at DTU Fotonik has resulted in a natural interest in spontaneous emission from quantum dots that is apparent also in this entirely theoretical project. The subjects covered over the course of the project may be divided into three main topics; electromagnetic scattering calculations, decay dynamics of single quantum dots and multiple quantum dot dynamics. At the time of writing, I feel that my study of the last of these topics is less complete than the first two. Nevertheless, I find the results interesting and I am happy to include them in the thesis.

A number of people have helped me throughout the project. First and foremost I am thankful to both my supervisors. Peter for his enthusiasm and experimental inputs and for introducing me to the interesting field of spontaneous emission. Jesper for sharing his impressive physical understanding and for invaluable help and guidance.

Early in the project I had the pleasure of visiting the FOM Institute AMOLF in Amsterdam, the Netherlands, for a short stay. I would like to thank Dr. Femius Koenderink for welcoming me to AMOLF and for sharing his knowledge as well as his numerical code with me, thus enabling the LDOS calculations of three dimensional photonic crystals in the work on fractional decay. Also, I would like to thank Bjarne Tromborg for many helpful discussions and suggestions for the fractional decay analysis.

In the spring of 2009 I visited the research group of Professor Stephen Hughes at Queen's University in Kingston, Canada. I would like to thank all the group members for the good times. A special thank to Steve for showing me the tools of the trade in FDTD and to the rest of the Hughes residence; Euan, Kai and Nanae for their enormous hospitality and for many delicious dinners and barbecues.

I would like to acknowledge the enjoyable working environment in the Theory and Signal Processing Group as well as the stimulating collaboration with the experimental Quantum Photonics Group. A special thank to Mr. Yaohui Chen for pleasant company in the office over the years.

Finally, and most importantly, I am grateful to Lisbet for her help and support and for making me remember that there is more to life than work, and that one should take time off every now and then.

Philip Trøst Kristensen
December 18, 2009

Abstract

Light-matter interaction in nanostructured materials is studied theoretically in relation to spontaneous emission dynamics of quantum dots in photonic crystals.

We present a novel solution method to the Lippmann-Schwinger equation for use in electric field scattering calculations. The method is well suited for multiple scattering problems such as photonic crystals and may be applied to problems with scatterers of arbitrary shape and non-homogeneous background materials. The method is formulated in the general case and details and examples are provided for the implementation in two dimensions. Application of the method is illustrated by calculating light emission from a line source in a finite sized photonic crystal waveguide

Fractional decay from semiconductor quantum dots is investigated. By the introduction of a measure for the degree of fractional decay we quantify to which extent the effect is observable in a given material. We focus on the case of inverse opal photonic crystals and locate the position in the crystal where the effect is most pronounced. Furthermore, we quantify the influence of absorptive loss and give example calculations with experimental parameters for PbSe quantum dots in Si inverse opals showing that absorption has a limiting but not prohibitive effect. In addition, we discuss how the resonant nature of the phenomenon puts rather severe restrictions on the stabilization of the system in possible experiments.

Last, we examine the influence on the decay dynamics of a quantum dot from other quantum dots. Using a self-consistent Dyson equation approach we describe how scattering from other quantum dots can be included in the Green's tensor for a passive material system. We numerically calculate both local and non-local elements of the Green's tensor for a photonic crystallite slab and apply the method for an example calculation with two quantum dots at specific locations in the unit cell. In this way it is explicitly shown how the decay dynamics of one quantum dot is qualitatively changed by the scattering properties of another.

Resumé

Lys-stof vekselvirkning i nanostrukturerede materialer studeres teoretisk med fokus på spontan emission af lys fra kvantepunkter i fotoniske krystaller.

Vi præsenterer en ny metode til løsning af Lippmann-Schwinger ligningen med anvendelser i elektromagnetiske spredningsproblemer. Metoden er velegnet til at undersøge lysudbredelse i fotoniske krystaller og kan benyttes til beregning af spredning fra objekter med vilkårlig form i en inhomogen baggrund. Vi præsenterer metoden i generel form og giver detaljer og eksempler vedrørende implementeringen i to dimensioner. Anvendelse af metoden illustreres ved beregning af lysudbredelse fra en linjekilde i en fotonisk krystal-bølgeleder.

Ved at indføre et mål for spaltede henfald kvantificeres det, i hvor høj grad effekten vil være mulig at observere i et givet materiale. Vi fokuserer på inverse opaler og bestemmer positionen i krystallen, hvor effekten er mest udtalt. Indflydelsen af absorption i materialet analyseres, og vi giver eksempler på udregninger med eksperimentelle parametre for blyselenid kvantepunkter i inverse opaler af silicium, der viser, at absorption har en målbar, men ikke ødelæggende indvirkning. Vi diskuterer hvordan krav til stabilisering af systemet lægger begrænsninger på mulige eksperimenter.

Endeligt studeres indflydelsen på spontan emission fra andre kvantepunkter i en prøve. Ved hjælp af en selvkonsistent metode baseret på Dysons ligning beskrives det, hvordan spredning fra kvantepunkter kan inkluderes i Greens tensor for et passivt materialesystem. Numerisk beregnes både lokale og ikke-lokale elementer af Greens tensor for en fotonisk krystal-membran, og der gives et eksempel på beregninger med to kvantepunkter, der eksplicit viser, at den spontane emission fra et kvantepunkt kan ændres kvalitativt på grund af spredning fra et andet kvantepunkt.

List of publications

Below we list the publications resulting from the work in this PhD project.

Journal publications

J1 Jeppe Johansen, Søren Stobbe, Ivan S. Nikolaev, Toke Lund-Hansen, Philip Trøst Kristensen, Jørn Märcher Hvam, Willem Vos and Peter Lodahl, *Size dependence of the wavefunction of self-assembled InAs quantum dots from time-resolved optical measurements.* Physical Review B **77**, 073303 (2008).

J2 Philip Trøst Kristensen, A. Femius Koenderink, Peter Lodahl, Bjarne Tromborg, and Jesper Mørk, *Fractional decay of quantum dots in real photonic crystals.* Optics Letters **33**, 1557-1559 (2008) .

J3 Andreas Næsby Rasmussen, Troels Suhr Skovgård, Philip Trøst Kristensen and Jesper Mørk, *Influence of pure dephasing on emission spectra from single photon sources.* Physical Review A **78**, 045802 (2008).

J4 Søren Stobbe, Jeppe Johansen, Philip Trøst Kristensen, Jørn Märcher Hvam and Peter Lodahl, *Frequency dependence of the radiative decay rate of excitons in self-assembled quantum dots: Experiment and theory.* Physical Review B **80**, 155307 (2009.)

J5 Philip Trøst Kristensen, Peter Lodahl and Jesper Mørk, *Light propagation in finite-sized photonic crystals: Multiple scattering using an electric field integral equation.* Journal of the Optical Society of America B **27**, 228-237 (2010).

Conference contributions

C1 Philip Trøst Kristensen, Bjarne Tromborg, Peter Lodahl and Jesper Mørk, *Breakdown of Wigner-Weisskopf theory for spontaneous emission: a quantative analysis.* Optical Waveguide Theory and Numerical Modelling. Lyngby, Denmark, 2007

C2 Søren Stobbe, Jeppe Johansen, Ivan S. Nikolaev, Toke Lund-Hansen, Philip Trøst Kristensen, Jørn Märcher Hvam, Willem Vos and Peter Lodahl, *Accurate measurement of the transition dipole moment of self-assembled quantum dots.* CLEO/Europe-IQEC. Munich, Germany, 2007.

C3 Jeppe Johansen, Søren Stobbe, Ivan S. Nikolaev, Toke Lund-Hansen, Philip Trøst Kristensen, Jørgen märcher Hvam, Willem Vos and Peter Lodahl, *Quantum efficiency of self-assembled quantum dots determined by a modified optical local density of states.* QLEO/QELS/PHAST Conference proceedings, Baltimore, Maryland, USA, 2007.

C4 Andreas Næsby Rasmussen, Troels Suhr Jørgensen, Philip Trøst Kristensen, Jesper Mørk, *Influence of Pure Dephasing on Emission Spectra from Quantum Dot-Cavity Systems.* Coherent Optical Technologies and Applications - 2008 Summer Optics and Photonics Congress Abstracts, paper JWE7, Boston, Massachusetts, USA, 2008.

C5 Philip Trøst Kristensen, Femius Koenderink, Peter Lodahl, Bjarne Tromborg and Jesper Mørk, *Fractional decay of quantum dots in photonic crystals.* CLEO/QELS 2008, Technical Digest CD-ROM, paper QFA3, San José, California, USA, 2008.

C6 Philip Trøst Kristensen, A. Femius Koenderink, Peter Lodahl, Bjarne Tromborg and Jesper Mørk, *Fractional decay of quantum dots in photonic crystals.* Danish Optical Society/Danish Physical Society annual meeting 2008, Nyborg Strand, Denmark, 2008.

C7 Andreas Næsby Rasmussen, Troels Suhr Jørgensen, Philip Trøst Kristensen and Jesper Mørk, *Influence of pure dephasing on emission spectra from single photon sources.* Danish Optical Society/Danish Physical Society annual meeting 2008, Nyborg Strand, Denmark, 2008.

C8 Troels Suhr Skovgård, Philip Trøst Kristensen, Lars Hagedorn Frandsen, Martin Schubert, Niels Gregersen and Jesper Mørk, *Nonlinear dynamics in photonic crystal nanocavity lasers.* CLEO/Europe-EQEC 2009 Conference proceedings, paper CB2.3, Munich, Germany, 2009.

C9 Philip Trøst Kristensen, Peter Lodahl and Jesper Mørk, *Fast, Accurate and Stable Scattering Calculation Method with Application to Finite Sized Photonic Crystal Waveguides.* Advances in Optical Sciences: OSA Optics & Photonics Congress 2009 Abstracts, paper ITuD2, Honolulu, Hawaii, USA, 2009.

Popular science

P1 Philip Trøst Kristensen, Peter Lodahl and Jesper Mørk, *To decay or not to decay - or both ! Quantum mechanics of spontaneous emission.* DOPS-Nyt **23**, 1, 4-8 (2008).

P2 Søren Stobbe, Philip Trøst Kristensen and Peter Lodahl, *Kvanteoptik i et farvet vakuum : Anvendelser af nanoteknologi og nanofotonik.* Optiske Horisonter : en rejse på kommunikationsteknologiens vinger, 29-47 (COM•DTU, 2007)

Contributions to journal publications by the author

All research in the articles J2 and J5 was done by the author, as was the development and implementation of the necessary numerical code, with the exception of the plane wave code used in J2. Both articles were written by the author and discussed with the co-authors.

Contributions to articles J1 and J4 were in the form of code and calculation methods originally developed by the author for the calculations of local density-of-states and electron and hole wavefunctions using finite element modeling.

Article J3 resulted from a student project for which the author acted as co-supervisor. Contributions to this work were in the form of guidance and help on the theory and interpretation.

Contents

Chapter 1

Introduction

1.1 Invitation: Spontaneous emission from semiconductor quantum dots

In order to introduce some central concepts in the theory of light-matter interaction in micro- and nanostructured media, we start out by describing an experiment in which spontaneous emission of light from InAs quantum dots (QDs) was investigated using time-resolved measurements. The QDs in the experiment were grown by molecular beam epitaxy resulting in small protrusions of InAs atop a thin so-called wetting layer. Both dots and wetting layer were surrounded by GaAs as illustrated in Fig. 1.1.

Carrier confinement within the QDs leads to quantization of the allowed energy levels as known from atomic physics. Therefore, for most of our purposes we can think of the QDs as artificial atoms with two distinct energy levels that are controlled in the manufacturing process. Fig. 1.1 illustrates the basic ideas of the experiment. Using a pump laser an excitation is created in the system. Subsequently, the system decays to the ground state under the emission of a photon with a frequency corresponding to the energy difference between the excited state and the ground state. Detection of the emitted light thus signifies that a spontaneous emission event has occurred.

1.1.1 Sample preparation and characterization

The experiment was performed by measuring on a single sample that was specially prepared so that nominally identical QDs were located at different distances to a silver mirror. Below, we briefly discuss details of the sample preparation and the

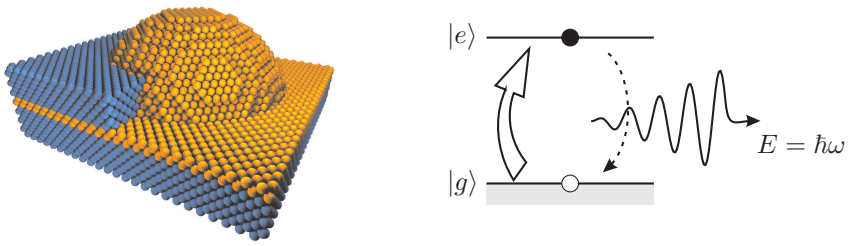

Figure 1.1: Left: Sketch of a self-assembled InAs quantum dot in GaAs. As InAs (yellow atoms) is grown on top of GaAs (blue atoms), the QDs appear as small lumps of InAs on top of a thin so-called wetting layer in order to minimize the surface energy. Subsequently, the QDs are overgrown with another layer of GaAs. Right: Sketch of the decay dynamics. A pump laser creates an excitation in the QD, and subsequently the system decays under emission of a photon with energy $E = \hbar\omega$, corresponding to the energy difference between the two states.

experimental setup. Starting from a GaAs wafer with embedded InAs QDs at a depth 302 nm, a total of 32 terraces were etched into the GaAs to different heights above the QD layer. After the etching process, an optically thick layer of silver was added to cover the terraces, effectively resulting in a silver mirror as seen from the position of the QDs. At a final step, the thin sample (approximately 1 μm) was placed on a block of sapphire (Al_2O_3) for support as illustrated in Fig. 1.2.

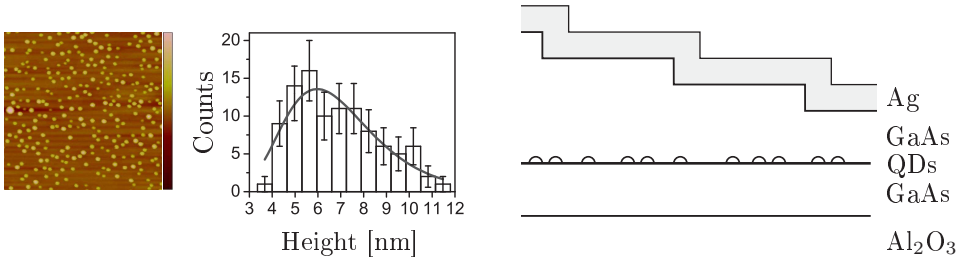

Figure 1.2: Left: Atomic Force Micrograph of a QD sample before overgrowth of GaAs, showing the QDs as nanometer sized bumps on the surface with the height distribution shown in the histogram. Figure from Ref. [1]. Right: Sketch of a cut through the sample showing how the QDs are placed at different distances to the silver mirror.

The sample was kept in a He closed cycle cryostat at constant temperature. Within the cryostat the sample could be translated in all three spatial directions,

so that the focus could be changed through the 32 different terraces on the sample. The system was pumped by a mode-locked laser source producing pulses of femtosecond width at a repetition rate of approximately 80 MHz. The emitted light was collected and sent through a spectrometer with a) a CCD camera for spectral measurements or b) a silicon avalanche photodiode (APD) for time resolved measurements. Fig. 1.3 shows the spectrum of the emitted light. Apart from the pump that is clearly visible at around 850 nm, we notice that the spectrum is broadened, so that light at a continuum of wavelengths is emitted from the sample. This so-called inhomogeneous broadening of the QDs arise from the experimental conditions; the pump laser excited a lot of different QDs in the sample which had slightly different sizes due to the manufacturing process. Since the QD energy levels arise from carrier confinement, the distribution in sizes maps directly onto a distribution in emission energies.

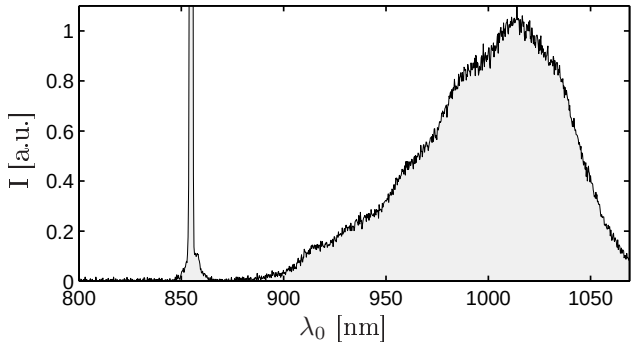

Figure 1.3: Spectrum of the QD sample.

Although the spectrum shows that light was emitted from many QDs, the monochromator in the experimental setup enabled a spectral filtering. This, combined with low pump powers, resulted in the collection of light from QDs of approximately the same size only. Throughout the experiment, measurements were performed at a constant wavelength of $\lambda_0 = 1020\,\text{nm}$, and the pump power was kept sufficiently low that only the lowest lying states in the QDs were excited.

1.1.2 Quantum dot lifetime measurements

After the initial spectral characterization, time correlated measurements were carried out in order to investigate the spontaneous emission. At the repetition rate of 80 MHz, the pump laser was used to excite carriers in the QDs, and a timer was started. The subsequent decay of the carriers back to the ground state was monitored from the emitted photon using the APD which stopped the timer in case

of a detection event. Based on the APD detection events, a histogram of detection times was created that we will refer to as the decay curve. Figure 1.4 shows decay curves obtained from QDs at different distances from the silver mirror.

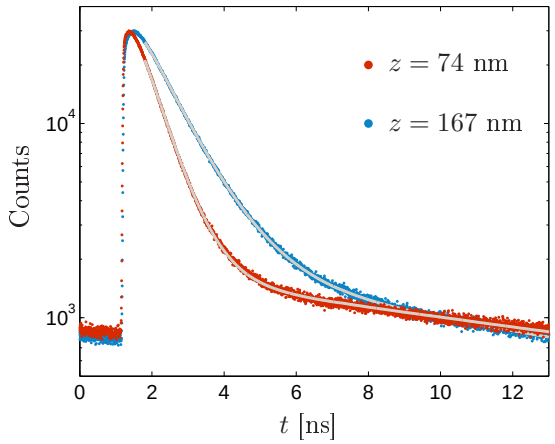

$z = 74$ nm	
Γ_{fast}	$1.52\ \text{ns}^{-1}$
Γ_{slow}	$0.07\ \text{ns}^{-1}$
A_{fast}	45.3×10^3
A_{fast}	1.67×10^3
χ^2_{R}	1.29

$z = 167$ nm	
Γ_{fast}	$0.93\ \text{ns}^{-1}$
Γ_{slow}	$0.09\ \text{ns}^{-1}$
A_{fast}	41.4×10^3
A_{fast}	1.91×10^3
χ^2_{R}	1.19

Figure 1.4: Decay curves from QDs at emission wavelength $\lambda_0 = 1020$ nm and temperature $T = 45$ K. The QDs are placed at different distances from the silver mirror. Solid lines show double exponential fits to the curves with the fitted parameters in the tables to the right.

As with most other decay processes in nature, we expect to find an exponential decrease, characterized by a decay constant. From Fig. 1.4 we recognize that there are (at least) two rates, namely a fast rate, Γ_{fast}, which is evident at times $t \lessapprox 6$ ns, and a slow rate, Γ_{slow}, which becomes pronounced only at longer times. Therefore, we fit the experimental results to a model of the type

$$f(t) = A_{\text{fast}} \exp(-\Gamma_{\text{fast}} t) + A_{\text{slow}} \exp(-\Gamma_{\text{slow}} t).$$

The table in Fig. 1.4 lists the results of the fits for the two decay curves, including the goodness of fit parameter χ^2_{R} [2]. There is a pronounced difference in the fast decay rate which is clearly visible in the figure. Due to the sample preparation and the spectral filtering, we know that the QDs are nominally identical, which means that the difference in decay curves must stem from the difference in distances to the silver mirror. Moreover, these distances are two orders of magnitude larger than the size of the QDs, which means that the carriers are not directly influenced by the silver mirror. This leads us to the somewhat unintuitive conclusion that it is properties of the environment that changes the rate of decay of the QDs. This

phenomenon was first pointed out by Purcell [3] and is a striking feature of the quantum mechanics of spontaneous emission.

1.1.3 Interpretation

Given the solid state nature of the QDs, we expect the total rate of decay from a QD, Γ_T, to be the sum of two contributions, namely a radiative and a non-radiative rate

$$\Gamma_{\mathrm{T}} = \Gamma_{\mathrm{R}} + \Gamma_{\mathrm{NR}}, \tag{1.1}$$

where the non-radiative decay rate, Γ_{NR}, represents the sum of all non-radiative decay channels and is assumed to be independent of the position (as long as it is sufficiently far away from interfaces between different media, such as in the experiment). The non-radiative decay rate is important for applications since it determines the so-called quantum efficiency, i.e. the fraction of initially excited carriers that ultimately leads to emitted photons.

The experiment directly shows that contrary to the non-radiative decay rate, the radiative decay rate Γ_{R} may change with position. It is reasonable to expect that the decay rate depends also on intrinsic properties of the QD (in the same way that the emitted field from a classical dipole depends on the dipole moment), so that

$$\Gamma_{\mathrm{R}} = \alpha_{\mathrm{I}} \rho_x(\mathbf{r}), \tag{1.2}$$

where now α_{I} denotes intrinsic properties of the QD and $\rho_x(\mathbf{r})$ denotes the influence from the surroundings. Since the intrinsic properties are independent of the surroundings, the radiative decay rate can be written as

$$\Gamma_{\mathrm{R}} = \Gamma_{\mathrm{R}}^{\mathrm{hom}} \frac{\rho_x(\mathbf{r})}{\rho_{\mathrm{hom}}}, \tag{1.3}$$

where $\Gamma_{\mathrm{R}}^{\mathrm{hom}}$ is the reference radiative decay rate of the QD in the homogeneous material described by ρ_{hom}. The ratio $\rho_x(\mathbf{r})/\rho_{\mathrm{hom}}$ is known as the Purcell factor. It describes how much faster or slower the decay occurs in a given environment than in the homogeneous medium.

There is a subtle issue in the above interpretation. The measured decay curves fitted well to an exponential function, and we therefore assigned a decay rate to the QD. Implicitly we thus made a model of the excitation in the QD, whereas the experiment measured the intensity of the emitted light and not the excitation. Indeed, each detection event consisted of the absorption of light in which a photon was annihilated, and an electron was promoted to an excited state in the APD semiconductor chip. Using a simple rate equation picture we can readily account for the exponential decay in the measured data. Given that the number of excitations

of the QDs decay exponentially, and that every radiative decay of an excitation results in the creation of a photon, we have the relations

$$\dot{P}_{\mathrm{e}} = -\Gamma_{\mathrm{T}} P_{\mathrm{e}}$$
$$\dot{P}_{\mathrm{ph}} = \Gamma_{\mathrm{R}} P_{\mathrm{e}},$$

where $P_{\mathrm{e}}(t)$ and $P_{\mathrm{ph}}(t)$ denote the number of QD excitations and photons, respectively. From the rate equations it follows that the number of photons that are created between times t and $t + \Delta t$ is given as

$$\Delta P_{\mathrm{ph}}(t) = \Gamma_{\mathrm{R}} \int_{t}^{t+\Delta t} P_{\mathrm{e}}(\tau)\mathrm{d}\tau = \frac{\Gamma_{\mathrm{R}}}{\Gamma_{\mathrm{T}}}(1 - e^{-\Gamma_{\mathrm{T}}\Delta t})e^{-\Gamma_{\mathrm{T}} t}, \tag{1.4}$$

where we have assumed that $P_{\mathrm{e}}(0) = 1$. Using the rate equation picture, we can thus argue that in the case of an exponential decrease in the number of excitations, the number of created photons also decreases exponentially.

The APDs measure intensity $\langle I(t) \rangle$ which is proportional to the number of photons per second impinging on the imaging chip. The measurements in Fig. 1.4 thus represents the integrated intensity, and from Eq. (1.4) we may directly associate the rate of change in the measurement histograms with the total decay rate Γ_{T}. Intensity measurements are convenient from an experimental point of view, but both $P_{\mathrm{e}}(t)$ and $\langle I(t) \rangle$ are in principle measurable quantities. The choice of whether to focus on one or the other relates to the objective of the particular experiment or theory. For the remainder of this section we will focus on the probability $P_{\mathrm{e}}(t)$ that at time t an excitation exists within the QD, and we will refer to $P_{\mathrm{e}}(t)$ as the decay curve.

The experiment is similar to experiments performed by Drexhage in the 1970's using dye molecules [4]. Whereas the focus of the series of experiments by Drexhage was the direct observation of the Purcell effect, experiments similar to the one described has been carried out recently as a means to characterize the QDs. Since the radiative decay rate is proportional to both intrinsic and extrinsic properties, one of the properties can in principle be measured if the other is known. For real QDs, however, there may also be a significant non-radiative contribution to the decay rate, as discussed above. Through systematic measurements of the decay rate for QDs subject to different values of $\rho_x(\mathbf{r})$ one is able to separate the radiative contribution from the non-radiative contribution [1, 5]. Fig. 1.5 shows the results in Ref. [5] in which measurements similar to the one described were fitted to a theoretical prediction for $\rho_x(\mathbf{r})$ in order to determine the values $\Gamma_{\mathrm{R}}^{\mathrm{hom}} = 0.95 \pm 0.03\,\mathrm{ns}^{-1}$ and $\Gamma_{\mathrm{NR}} = 0.11 \pm 0.03\mathrm{ns}^{-1}$.

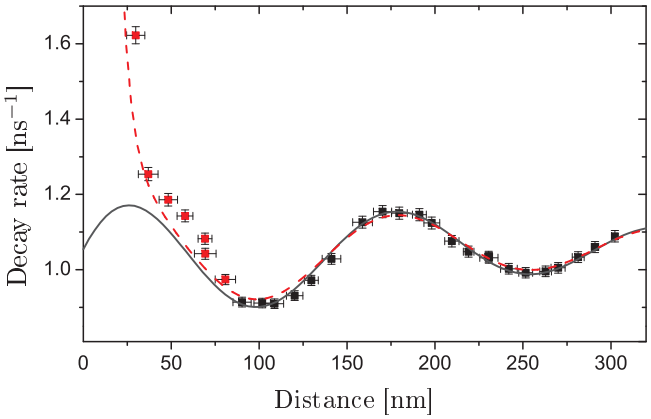

Figure 1.5: Decay rates of InAs QDs in GaAs as a function of distance to an air interface. The data show a clear oscillatory behavior due to $\rho_x(\mathbf{r})$, as shown by the solid curve. The dashed line shows an alternative theoretical $\rho_x(\mathbf{r})$ curve that is designed to account for dissipation close to the interface. Figure from Ref. [5].

1.2 Controlling light emission and scattering: Quantum dots in photonic crystals

Based on the experiment in section 1.1 we will now discuss and motivate the theoretical work in this thesis. For now, we will not discuss the mathematical details but rather focus on a qualitative introduction to the basic elements of light-matter interaction.

1.2.1 Light scattering calculations and the electromagnetic Green's tensor

On distances much larger than the wavelength, light can simply be described as rays - the so-called ray picture of light [6]. This explains how, in the experiment, we could use lenses to focus the emitted light onto the detection part of the setup. At distances that are comparable to the wavelength, however, this picture is no longer valid as the wave nature of light becomes important. Indeed, the difference in decay rate for QDs at different distances from the silver mirror may be interpreted as an interference phenomenon, and we note that the variations in decay rates in Fig. 1.5 is similar to the effective wavelength of light in GaAs.

Fig. 1.6 shows the electric field from a line source in air in the vicinity of two dielectric cylinders of refractive index $n_R = 3.5$ in air. Light is emitted from the line source and scatters off the cylinders. Even with only two cylinders, a complex

interference pattern results.

In order to properly model the propagation of light waves in micro-structured materials, one has to account for scattering from all different obstacles in a coherent way, so that interference effects will be included in the description. In classical electromagnetic theory, this is done using the electromagnetic propagator, or Greens tensor, which may be interpreted as the electric field at point $\mathbf{r}$ due to an oscillating dipole at the point $\mathbf{r}'$. In a theoretical description of the experiment in section 1.1, the Green's tensor is the mathematical object that describes light propagation from the QDs to the detector. The field in Fig. 1.6 is exactly the Green's tensor. Given the complexity of many micro-structures, the calculation of the Green's tensor is a highly non-trivial task in the general case, and usually numerical methods are employed.

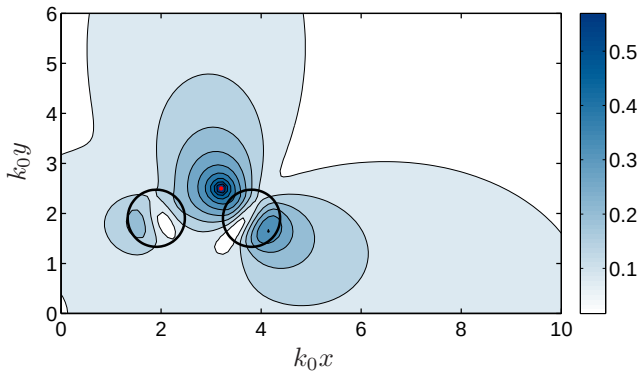

Figure 1.6: Two dimensional Green's tensor describing propagation of light emitted from a line source as indicated by the red dot. Scattering due to the two cylinders results in a complicated interference pattern.

A silver mirror represents a very simple geometry in which to study interference effects. This is convenient from both a theoretical and an experimental point of view. Theoretically, calculations describing the light scattering in case of a simple interface structure are fast due to the symmetry of the problem. Experimentally, the symmetry relaxes the requirements on the sample preparation because only the QD position relative to the interface is important. The simple interface structure, however, limits the number of interfering waves. Other, more advanced, structures exist that exploit the scattering and interference effects arising in periodic structures.

1.2.2 Photonic crystals

Photonic crystals (PCs) are fascinating materials that offer unique possibilities for light-propagation control [7, 8, 9]. As the name suggests, PCs are materials with a periodic structuring on a length scale comparable to the wavelength of light. Multiple scattering from the periodic structure alters the effective properties of the material in a controlled way. In order to achieve as strong scattering as possible, PCs are typically made from a dielectric with a high refractive index such as Silicon. The multiple scattering may even lead to photonic band gaps - frequency intervals in which no electromagnetic field is allowed to propagate in the material. Such materials are ideally suited for the creation of optical circuits and even cavities where light may, in principle, be perfectly confined.

In practice, the manufacturing of full three dimensional PCs has proven to be very difficult. One type of crystal that has been successfully produced is the so-called inverse opals. Fig. 1.7 shows a sketch of the unit cell. Inverse opals are made by infiltrating an fcc crystal of polystyrene spheres with dielectric and subsequently evaporating the polystyrene, leaving a complicated periodic structure [10].

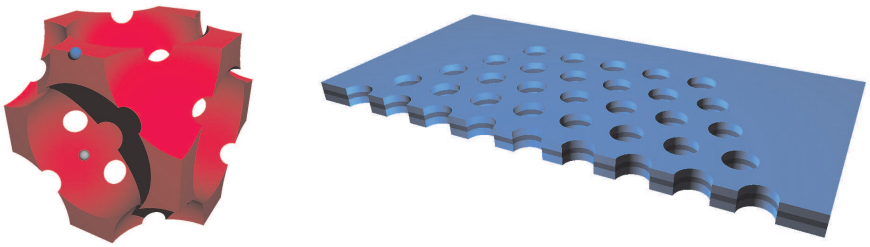

Figure 1.7: Left: Sketch of inverse opal unit cell with two QDs placed at the high-symmetry points Γ (in the center of the air sphere) and H (between six air spheres). Right: Sketch of a PC slab consisting of a periodic array of air holes in a semiconductor membrane.

As an alternative to full three dimensional PCs, so-called PC slabs are made from thin semiconductor membranes by etching periodic arrays of holes as illustrated in Fig. 1.7. The index contrast confines light to in-plane motion through total internal reflection while scattering off the periodic array of air holes affects the spectral distribution of modes in the same way as a Bragg mirror, yet effective in all in-plane directions. The planar nature of these structures makes them compatible with standard semiconductor fabrication techniques. In addition, the material making up the membrane may be conveniently grown using standard epitaxial growth

techniques, thus directly enabling the inclusion of self-assembled QDs. From a theoretical point of view, the confinement to in-plane motion in PC slabs means that many aspects of light propagation in these materials may be understood from two dimensional models. This greatly simplifies the generally very complex scattering calculations. This work is concerned with modeling of inverse opals and PC slabs only. Other experimental realizations of three dimensional PCs include woodpile crystals [11] and the so-called Yablonovite [12, 13].

1.2.3 Quantum optics and the local density-of-states

Whereas many optical phenomena may be adequately described in a semi-classical model, spontaneous decay of an initially excited emitter can only be fully understood in a framework in which both the emitter and the light field is quantized. Early theory of spontaneous emission dates back to Einstein [14] and Dirac [15] as well as Wigner and Weisskopf who used a full quantum optical description, combined with a novel approximation, to show how the coupling of an excited atom to the continuum of modes in vacuum naturally leads to an exponential decay [16]. One can show that given an initial condition in which an electron is in an excited state of an atom, the probability that at time t the electron is still in the excited state decays exponentially with time. The calculations by Wigner and Weisskopf can be applied also to semiconductor QDs to reveal an exponential decay.

In the mathematical framework of quantum optics the electromagnetic modes are described as harmonic oscillators. Therefore, the distribution of modes at the position of the QD is of special importance as it describes the number of oscillators with which the QD can interact. The calculated decay rate turns out to be proportional to the number of electromagnetic modes, and the quantum optical theory of Wigner and Weisskopf thus seems to agree with the measurements in Figs. 1.4 and 1.5 which did indeed show an exponential decay with a rate that we could argue was proportional to properties of the environment. From the theory we can now argue that it is the *electromagnetic* properties of the environment that influences the decay rate. The number of electromagnetic modes at a given position is usually referred to as the local density-of-states (LDOS) [17] and is exactly the parameter $\rho_x(\mathbf{r})$ that we introduced in Eq. (1.3).

The LDOS may be calculated analytically for a very limited set of material structures, and usually numerical methods have to be used. Since the Green's tensor contains naturally contributions from all scattering sites in the material it can be used also to obtain the LDOS. Fig. 1.8 shows the LDOS of a Si inverse opal at the two high-symmetry positions Γ and K. A band gap is clearly visible around $\omega a/2\pi c \approx 0.8$ where the LDOS drops to zero, indicating that no modes exist in the material at this frequency.

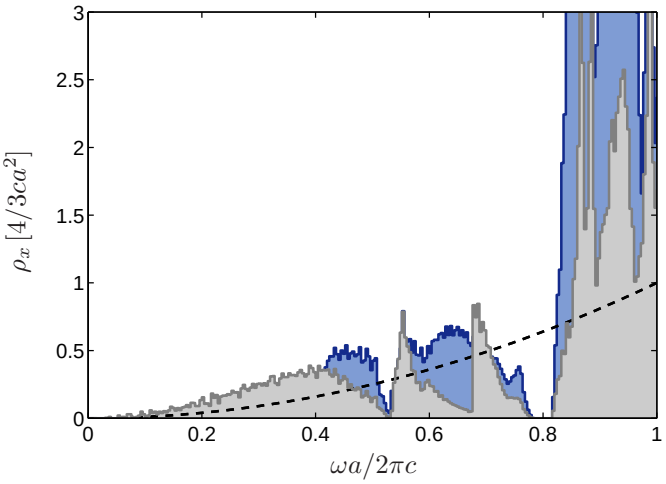

Figure 1.8: LDOS of a Si inverse opal at the two positions Γ *(gray histogram) and* H *(blue histogram) as indicated in Fig. 1.7. Dashed line indicates the free space LDOS,* $\rho_0(\omega) = \omega^2/3\pi^2c^3$.

1.2.4 Quantum dot decay dynamics

Variations in the LDOS may lead to a suppression or an enhancement of the measured decay rate as shown explicitly in Figs. 1.4 and 1.5. It may even change the qualitative behavior of the decay dynamics as the decay needs not always be exponential, and the emitter needs not always to decay fully. Indeed, depending on the variations in the LDOS the decay may happen in a number of fundamentally different ways as illustrated in Fig. 1.9.

When interacting with a continuum of electromagnetic modes, the decay is a Markovian process. Once the energy is transferred from the emitter to the electromagnetic field it is irreversibly lost, and the emitter ends up in the ground state. A continuum of modes in the language of coupled oscillators amounts to a LDOS that varies slowly as a function of frequency. In this case the theory of Wigner and Weisskopf shows that the decay curves are decaying exponentials. It follows directly that the rate may be enhanced relative to the rate in the homogeneous medium by changing the distribution of optical modes at the location of the emitter. This is the famous Purcell effect.

If the emitter can interact only with a single mode of the electromagnetic field there will be an interchange of energy back and forth between the emitter and the field. This may happen in cavities of very high quality, for example in PCs. In this case the LDOS will exhibit a sharp peak at the frequency of the cavity resonance resulting in a coherent interchange of energy between the two leading to oscillations

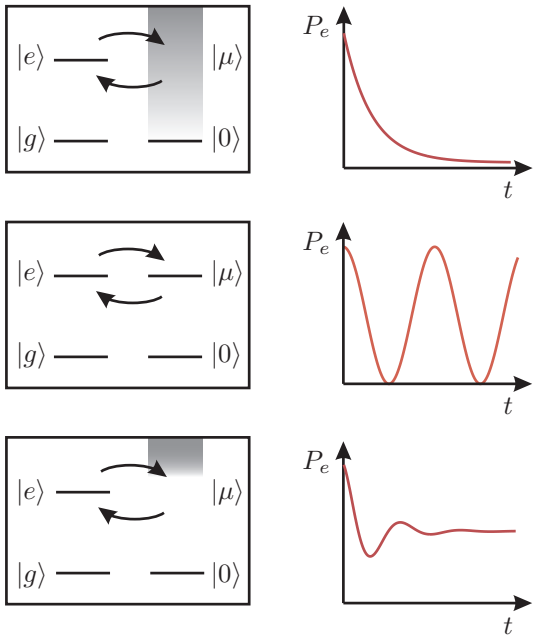

Figure 1.9: Different QD decay dynamics. Top: Exponential decay characteristic of a single oscillator interacting with a continuum of modes. Middle: Interaction of two oscillators leading to continuous interchange of energy between the two known as vacuum Rabi oscillations. Bottom: A single oscillator interacting with a detuned continuum of modes leading to fractional decay. The figure is inspired by a similar illustration by Weisbuch et al. *[18].*

in the decay curve known as vacuum Rabi oscillations.

An interesting situation occurs when the emitter is tuned spectrally very close to the sharp edge of the band gap of a PC. In this case the emitter may undergo a so-called fractional decay in which the probability tends to a finite, non-zero value at long times [19, 20]. The interaction of the QD with modes of low (or even zero) group velocity at the band edge leads to a situation in which some of the energy is preserved in the system and some is lost to the environment. This phenomenon clearly represents a very counter intuitive example of the quantum nature of the decay in which the electron is not fully excited, yet has not fully decayed either.

1.2.5 Experiments and applications

On the experimental side, manipulation of the spontaneous decay rate due to the Purcell effect in PCs has been shown in a number of experiments. These include

both the use of inverse opals [21] and PC slabs [22, 23]. Advances in fabrication have enabled the study of physics of optical microcavities [24]. The high LDOS achievable in a small cavity leads to fast decay due to the Purcell effect as has been demonstrated in cavities in a number of systems including PC slabs [25]. The so-called strong coupling regime of an emitter interacting with a single optical mode has been observed (using spectral analysis) for cavities in photonic crystal slabs [26] as well as in other types of optical cavities [27]. The controlled positioning of a microcavity around a single self-assembled QD in a PC slab was demonstrated in Ref. [28]. These results have spurred a lot of theoretical interest due to an off-resonant coupling of the QD to the optical mode in the microcavity, most likely due to phonon interactions [29, 30, 31]. Fractional decay has yet to be experimentally demonstrated. During this PhD project we have carried out quantitative calculations in order to assess the possible demonstration of this novel quantum effect using QDs in Si inverse opals.

As for applications, the suppression of spontaneous emission in photonic crystals was proposed originally as a means to achieve more efficient solar cells and semiconductor lasers [7, 8].

Light-matter interaction involving a single or a few QDs will find applications in the emerging field of quantum information technologies, especially for secure communication [32] and quantum networks [33]. Single photon sources as well as single photon switches and transistors are key elements in optical quantum networks. The use of single photon sources for quantum cryptography has been demonstrated experimentally [34], and recently the high Purcell factor and the built in directionality of the emitted light achievable in wave guides in photonic crystal slabs has been proposed [35, 36] and experimentally demonstrated [37] as a means to achieve efficient and compact single photon sources.

Deterministic creation of entangled photon pairs are of particular interest for quantum cryptography [38, 39] as well as for quantum imaging [40, 41], quantum teleportation [42] and quantum computing [43, 44]. Entangled photon pairs may in principle be emitted from bi-exciton decay in QDs, and the field has received attention both theoretically [45] and experimentally [46].

1.3 Overview of this thesis

In chapter 2 we set up the theoretical framework that will be used throughout the thesis. Many of the results in the chapter will be well known to the reader, but are repeated here in order to present a coherent overview of the theory and to illustrate how the results relate to each other. For use in the modeling of nanophotonic structures, and in particular in the context of light-matter interaction in photonic

crystals, we focus on a scattering type formulation of light propagation based on the electric field Green's tensor.

Using the Green's tensor for the background medium, one may recast Maxwell's wave equation as a scattering problem, in which case the solution is given in terms of the so-called Lippmann-Schwinger integral equation [47]. During the project we have developed a novel approach to the numerical solution of the Lippmann-Schwinger equation. The method may be applied to systems with scatterers of arbitrary shape and non-homogenous background materials. In chapter 3 we formulate the method in the general case and give details of the implementation in two dimensions as well as example calculations. We illustrate the method by calculating light emission from a line source in a finite sized photonic crystal waveguide.

Depending on the objective, one will naturally focus on properties of either the excitations in the QD or the emitted field as discussed in section 1.1.3. As noted in Ref. [48], this amounts to a choice between two pictures in which to solve a quantum optical problem of light-matter interaction: an all-matter picture or an all-light picture. In chapter 4 we work in the all-matter picture and examine fractional decay in three-dimensional photonic crystals. Working in an all matter picture, the dynamics are governed by the LDOS as illustrated in section 1.2.4. We perform high resolution calculations of the LDOS in a Si inverse opal in order to assess the possible realization of fractional decay in these systems. Furthermore, we quantify the influence of absorptive loss and show that it is a limiting but not prohibitive effect.

For many applications it is desirable to have an interaction between the QDs and the electromagnetic field that is as large as possible. High-quality QDs show an impressive light-matter interaction which is important for applications such as single-photon sources. Likewise, this is important for novel quantum optics experiments aimed, for example, at the experimental demonstration of non-Markovian decay dynamics as described in section 1.2.4. However, if the QD interacts strongly with light it means that it will itself act as a scatterer for the light. This may have consequences for measurements as it may change the LDOS or even result in different decay curves. In chapter 5 we choose an all light approach to study multiple QD dynamics in photonic crystal slabs.

Finally, chapter 6 holds the conclusions.

Chapter 2

Theory of light-matter interaction

2.1 Introduction

This chapter provides an overview of the theory of light-matter interaction used for calculations in this work. It is not the objective to derive the theory from first principles, and we will present derivations only if they serve to clarify particular results. Rather, we refer to the literature for the derivations and focus on a coherent presentation of the parts of the theory important for our purpose.

2.1.1 Overview of Chapter 2

The theory divides naturally into three parts: light propagation and scattering, QD dynamics and the coupling of the two. In section 2.2 we discuss the theory of light propagation and scattering based on Maxwell's equations and the electromagnetic Green's tensor. In addition, we discuss canonical quantization of the field in terms of quantum mechanical field operators and elements of PC theory.

Section 2.3 is concerned with QD models and a proper description of excitations in the form of excitons. Section 2.4 presents the typical coupling formalism employed in the literature, and we derive and solve equations of motion for the QD dynamics as well as for the electric field emitted from a QD.

2.2 Modeling light propagation and scattering

As we aim to model light-matter interaction in semiconductors we will concider only non-magnetic materials with no free charges or currents. Therefore, we start from Maxwell's equations in the form

$$\nabla \cdot \mathbf{D} = 0 \tag{2.1a}$$

$$\nabla \cdot \mathbf{B} = 0 \tag{2.1b}$$

$$\nabla \times \mathbf{E} = -\frac{\partial}{\partial t}\mathbf{B} \tag{2.1c}$$

$$\nabla \times \mathbf{H} = \frac{\partial}{\partial t}\mathbf{D}, \tag{2.1d}$$

where $\mathbf{E}$ and $\mathbf{B}$ are the electric and magnetic fields, respectively, while $\mathbf{D}$ and $\mathbf{H}$ denote the electric displacement and auxiliary magnetic fields, respectively. The fields are related through the constitutive relations

$$\mathbf{D} = \epsilon_0 \mathbf{E} + \mathbf{P} = \epsilon_0 \epsilon_\mathrm{r} \mathbf{E} \tag{2.2}$$

$$\mathbf{H} = \frac{1}{\mu_0}\mathbf{B}, \tag{2.3}$$

where ϵ_0 and μ_0 are free space permittivity and permeability, respectively and ϵ_r is the relative permittivity. For non-magnetic materials we have $\epsilon_\mathrm{r} = n_\mathrm{R}^2$, where n_R is the refractive index. $\mathbf{P}$ denotes the intrinsic polarization of the passive material. In the case of an excitation event in a QD an exciton is formed, and in this case we model the polarization due to the exciton motion as an additional extrinsic polarization as discussed in section 2.2.1.

Eqs. (2.1c) and (2.1d) together with the constitutive relations provide the wave equation for the electric field,

$$\nabla \times \nabla \times \mathbf{E}(\mathbf{r}, t) + \frac{\epsilon_\mathrm{r}}{c^2}\frac{\partial}{\partial t^2}\mathbf{E}(\mathbf{r}, t) = 0, \tag{2.4}$$

with time-harmonic solutions of the form

$$\mathbf{E}(\mathbf{r}, t) = \mathbf{E}(\mathbf{r}) e^{-i\omega t}. \tag{2.5}$$

The position dependent electric field $\mathbf{E}(\mathbf{r})$ solves the vector Helmholtz equation

$$\nabla \times \nabla \times \mathbf{E}(\mathbf{r}) - k_0^2 \epsilon_\mathrm{r}(\mathbf{r}) \mathbf{E}(\mathbf{r}) = 0, \tag{2.6}$$

where $\epsilon_\mathrm{r}(\mathbf{r})$ is the position dependent relative permittivity and $k_0 = |\mathbf{k}_0| = \omega/c$ is the wave number in vacuum. Eq. (2.6) is a generalized eigenvalue equation and we

refer to the vector eigenfunctions and corresponding frequencies as $\mathbf{f}_\mu(\mathbf{r})$ and ω_μ, respectively. The vector eigenfunctions are normalized as

$$\int_V \epsilon_{\mathrm{r}}(\mathbf{r})\, \mathbf{f}_\mu^*(\mathbf{r}) \cdot \mathbf{f}_\lambda(\mathbf{r})\, \mathrm{d}\mathbf{r} \;=\; \delta_{\mu,\lambda}. \tag{2.7}$$

As discussed in section 1.2.3, the LDOS enters naturally in quantum optical calculations of light-matter interaction. The LDOS is a classical property of the electromagnetic field and is calculated as a sum over all electromagnetic modes in the system as

$$\rho_x(\omega, \mathbf{r}) = \sum_\mu |\mathbf{e}_x \cdot \mathbf{f}_\mu(\mathbf{r})|^2\, \delta(\omega - \omega_\mu), \tag{2.8}$$

where we have included a projection of the modes onto the direction $\mathbf{e}_x$. Since all calculations in this work are based on the projected LDOS, Eq. (2.8), we will typically refer to this simply as the LDOS. In a homogeneous material the LDOS is independent of position and projection direction and depends only on frequency as

$$\rho_{\mathrm{hom}}(\omega) = \frac{n_{\mathrm{R}}\omega^2}{3\pi^2 c^3}.$$

This is shown explicitly in appendix D.

2.2.1 Electric field from a point source - the Green's tensor

By the introduction of an extrinsic polarization, $\mathbf{P}_{ex}(\mathbf{r}, t)$, the wave equation for the electric field is rewritten as

$$\nabla \times \nabla \times \mathbf{E}(\mathbf{r}, t) = -\frac{\partial^2}{\partial t^2}\mu_0 \left\{\epsilon_0 \epsilon_{\mathrm{r}}(\mathbf{r})\mathbf{E}(\mathbf{r}, t) + \mathbf{P}_{ex}(\mathbf{r}, t)\right\},$$

which, by transforming to the frequency domain and rearranging, takes on a familiar form with the extrinsic polarization acting as the source:

$$\nabla \times \nabla \times \mathbf{E}(\mathbf{r}, \omega) - k_0^2 \epsilon_{\mathrm{r}}(\mathbf{r})\mathbf{E}(\mathbf{r}, \omega) = \frac{k_0^2}{\epsilon_0}\mathbf{P}_{ex}(\mathbf{r}, \omega). \tag{2.9}$$

In this case the electric field may be calculated as [49, 50]

$$\mathbf{E}(\mathbf{r}, \omega) = \int \mathbf{G}(\mathbf{r}, \mathbf{r}', \omega)\frac{k_0^2}{\epsilon_0}\mathbf{P}_{ex}(\mathbf{r}', \omega)\mathrm{d}\mathbf{r}', \tag{2.10}$$

in which $\mathbf{G}(\mathbf{r}, \mathbf{r}', \omega)$ is the electric field Green's tensor for the material system. The Green's tensor is the solution to the equation

$$\nabla \times \nabla \times \mathbf{G}(\mathbf{r}, \mathbf{r}', \omega) - k_0^2 \epsilon_{\mathrm{r}}(\mathbf{r})\mathbf{G}(\mathbf{r}, \mathbf{r}', \omega) = \mathbf{I}\delta(\mathbf{r} - \mathbf{r}'), \tag{2.11}$$

subject to the Sommerfeld radiation condition [51], and differs depending on the dimensionality. A similar equation defines the magnetic field Green's tensor. We will work only with the electric field version and we will refer to this as the electromagnetic Green's tensor to emphasize the wave nature of the field. Appendix A lists $\mathbf{G}(\mathbf{r}, \mathbf{r}', \omega)$ for homogeneous media in different dimensions. Apart from homogeneous materials, closed form expressions for the Green's tensor are restricted to a limited set of simple geometries such as spherically layered structures [52] and stratified media [53, 54]. A comprehensive theoretical treatment of electric and magnetic field Green's tensors in various geometries is given by Tai [49]. The definition of the Green's tensor in Eq. (2.11) is consistent with that of Refs. [49, 50, 55]. It differs by a factor of (-1) from the Green's tensor in Ref. [48] and by a factor of k_0^2 from that of Refs. [56, 57].

The interpretation of the Green's tensor becomes clear if we use Eq. (2.10) to calculate the field from a point source, $\mathbf{P_{ex}}(\mathbf{r}, \omega) = \mathbf{d}(\omega)\delta(\mathbf{r} - \mathbf{r}')$, as

$$\begin{aligned} \mathbf{E}(\mathbf{r}, \omega) &= \int \mathbf{G}(\mathbf{r}, \mathbf{r}'', \omega) \frac{k_0^2}{\epsilon_0} \mathbf{d}(\omega) \delta(\mathbf{r}'' - \mathbf{r}') \mathrm{d}\mathbf{r}'' \\ &= \mathbf{G}(\mathbf{r}, \mathbf{r}', \omega) \frac{k_0^2}{\epsilon_0} \mathbf{d}(\omega), \end{aligned} \tag{2.12}$$

which shows that the i'th column of the Green's tensor may be interpreted as the electric field at $\mathbf{r}$ due to a point source at $\mathbf{r}'$ oriented in the direction $\mathbf{e}_i$.

For a given material system, as defined by $\epsilon_{\mathrm{r}}(\mathbf{r})$, the Green's tensor may be expanded on the eigenmodes of the wave equation as [50, 58]

$$\mathbf{G}(\mathbf{r}, \mathbf{r}', \omega) = c^2 \sum_{\mu} \frac{\mathbf{f}_\mu(\mathbf{r}) \mathbf{f}_\mu^*(\mathbf{r}')}{\omega_\mu^2 - (\omega + i\eta)^2}, \tag{2.13}$$

where the infinitesimal but positive imaginary part $i\eta$ ensures causality of the Green's tensor [48]. Eq. (2.13), together with the identity

$$\lim_{\epsilon \to 0} \mathrm{Im} \left\{ \frac{1}{\omega_\mu^2 - \omega^2 - i\epsilon} \right\} = \frac{\pi}{2\omega_\mu} \left(\delta(\omega - \omega_\mu) - \delta(\omega + \omega_\mu) \right),$$

may be used to relate the Green's tensor to the LDOS as

$$\rho_x(\omega, \mathbf{r}) = \frac{2\,\omega}{\pi\, c^2} \mathrm{Im} \left\{ \mathbf{e}_x \, \mathbf{G}(\mathbf{r}, \mathbf{r}, \omega) \, \mathbf{e}_x \right\}. \tag{2.14}$$

2.2.2 The Lippmann-Schwinger equation

In section 2.2.1, the solution to the inhomogeneous problem in Eq. (2.9) was found as an integral over the electromagnetic Green's tensor and the source term. The

procedure is not limited to extrinsic sources but may equally well be applied to scattering problems in which the electric field appears on the right hand side. In order to reformulate Eq. (2.6) as a scattering problem, we consider the change in permittivity, $\Delta\varepsilon(\mathbf{r}) = \epsilon_\mathrm{r}(\mathbf{r}) - \epsilon_\mathrm{B}(\mathbf{r})$, caused by the introduction of scattering sites into the background medium described by $\epsilon_\mathrm{B}(\mathbf{r})$. With this definition, Eq. (2.6) is rewritten as

$$\nabla \times \nabla \times \mathbf{E}(\mathbf{r}) - k_0^2 \epsilon_\mathrm{B} \mathbf{E}(\mathbf{r}) = k_0^2 \Delta\epsilon(\mathbf{r}) \mathbf{E}(\mathbf{r}), \tag{2.15}$$

which is an implicit equation since the electric field itself enters on the right hand side. The solution to Eq. (2.6) with $\epsilon_\mathrm{r}(\mathbf{r}) = \epsilon_\mathrm{B}(\mathbf{r})$ is denoted by $\mathbf{E}^\mathrm{B}(\mathbf{r})$ and represents the incoming field. The full solution to Eq. (2.6) is the sum of the incoming field and the scattered field. It is given by the Lippmann-Schwinger equation [47, 55],

$$\mathbf{E}(\mathbf{r}) = \mathbf{E}^\mathrm{B}(\mathbf{r}) + \int_V \mathbf{G}^\mathrm{B}(\mathbf{r}, \mathbf{r}')\, k_0^2 \Delta\varepsilon(\mathbf{r}')\, \mathbf{E}(\mathbf{r}') \mathrm{d}\mathbf{r}', \tag{2.16}$$

in which $\mathbf{G}^\mathrm{B}(\mathbf{r}, \mathbf{r}')$ is the Green's tensor for the background medium. As in Eq. (2.16), we will typically omit the explicit frequency dependence of the Green's tensor to ease notation. In two and three dimensions the real part of the Green's tensor diverges in the limit $\mathbf{r}' = \mathbf{r}$. This means that for integrals in which $\mathbf{r}$ is inside the scattering volume (such as in this work) an alternative formulation of the Lippmann-Schwinger equation must be employed in which the singularity is isolated in an infinitesimal principal volume δV and treated analytically [59]. In this case we follow Ref. [55] and rewrite the Lippmann-Schwinger equation as

$$\mathbf{E}(\mathbf{r}) = \mathbf{E}^\mathrm{B}(\mathbf{r}) + \lim_{\delta V \to 0} \int_{V - \delta V} \mathbf{G}^\mathrm{B}(\mathbf{r}, \mathbf{r}')\, k_0^2 \Delta\varepsilon(\mathbf{r}') \mathbf{E}(\mathbf{r}') \mathrm{d}\mathbf{r}' - \mathbf{L} \frac{\Delta\epsilon_\mathrm{r}(\mathbf{r})}{\epsilon_\mathrm{B}} \mathbf{E}(\mathbf{r}),$$

where the exclusion volume δV is centered on $\mathbf{r}' = \mathbf{r}$ and $\mathbf{L}$ is a dimensionality dependent source dyadic. Expressions for the source dyadic are listed by Yaghjian for various shapes of the exclusion volume [59]. We will work only with circular exclusion areas in two dimensions and spheres in three dimensions for which we have

$$\mathbf{L}^\mathrm{2D} = \frac{1}{2} \begin{pmatrix} 1 & 0 & 0 \\ 0 & 1 & 0 \\ 0 & 0 & 0 \end{pmatrix} \quad \text{and} \quad \mathbf{L}^\mathrm{3D} = \frac{1}{3} \begin{pmatrix} 1 & 0 & 0 \\ 0 & 1 & 0 \\ 0 & 0 & 1 \end{pmatrix}.$$

The Dyson equation

From Eq. (2.12) we may interpret each column in the Green's tensor as an electric field. Therefore, the full Green's tensor for a given material system may be

calculated from a scattering formulation similar to Eq. (2.16) known as the Dyson equation [50, 55],

$$\mathbf{G}(\mathbf{r},\mathbf{r}') = \mathbf{G}^{\mathrm{B}}(\mathbf{r},\mathbf{r}') + \int_V \mathbf{G}^{\mathrm{B}}(\mathbf{r},\mathbf{r}'')\, k_0^2 \Delta\varepsilon(\mathbf{r}'')\, \mathbf{G}(\mathbf{r}'',\mathbf{r}')\mathrm{d}\mathbf{r}''. \tag{2.17}$$

Using the Dyson equation, known results for simple geometries may be used as background Green's tensors in numerical calculations of the Green's tensor for more complicated structures.

2.2.3 Quantization of the electromagnetic field

The physical electric field is real, and in applications one will therefore attribute physical significance only to the real part of Eq. (2.5). In quantum optics the electric field is promoted to an operator. Owing to the fundamental postulates of quantum mechanics, the operator of a dynamical variable must be Hermitian. This means that we must write the field as a sum of positive and negative frequency parts, each of the form of Eq. (2.5), with corresponding annihilation and creation operators, respectively. There is a freedom of choice in the exact form of the fields since any linear combination of solutions to Eq. (2.4) will itself be a solution. In this work we use the following description of the vector potential and the electric and magnetic fields, respectively:

$$\mathbf{A} = \sum_\mu \frac{\varepsilon_\mu}{\omega_\mu} \left(\mathbf{f}_\mu(\mathbf{r})\, a_\mu\, e^{-i\,\omega_\mu t} + \mathbf{f}_\mu^*(\mathbf{r})\, a_\mu^\dagger\, e^{i\,\omega_\mu t} \right) \tag{2.18a}$$

$$\mathbf{E} = -\frac{\partial}{\partial t}\mathbf{A} \;=\; i \sum_\mu \varepsilon_\mu \left(\mathbf{f}_\mu(\mathbf{r})\, a_\mu\; e^{-i\,\omega_\mu t} - \mathbf{f}_\mu^*(\mathbf{r})\, a_\mu^\dagger\; e^{i\,\omega_\mu t} \right) \tag{2.18b}$$

$$\mathbf{B} = \nabla \times \mathbf{A}. \tag{2.18c}$$

Eqs. (2.18) are consistent with Refs [48, 60, 61, 62, 63]. The operators a_μ and $a_\mu^\dagger$ are annihilation and creation operators, respectively, for a photon in mode μ. These satisfy bosonic commutation relations,

$$[a_\mu, a_\lambda^\dagger] \;=\; \delta_{\mu,\lambda}. \tag{2.19}$$

The field distribution functions $\mathbf{f}_\mu(\mathbf{r})$ are eigenfunctions of Eq. (2.6) with eigenvalues $(\omega_\mu/c)^2$ and are normalized according to Eq. (2.7). The field normalization constant ε_μ is given as

$$\varepsilon_\mu = \sqrt{\frac{\hbar\,\omega_\mu}{2\,\epsilon_0}}, \tag{2.20}$$

where $\hbar$ is the reduced Planck constant. The normalization is consistent with the fundamental postulate by Planck that the energy in a given mode of the electromagnetic field is found in quanta of $\hbar\omega_\mu$. Indeed, the Hamiltonian is given as

$$H_{\mathrm{EM}} = \epsilon_0 \int_V \epsilon_{\mathrm{r}}(\mathbf{r})\, \mathbf{E}^\dagger(\mathbf{r}) \cdot \mathbf{E}(\mathbf{r})\, \mathrm{d}\mathbf{r} \tag{2.21}$$

which, by the use of Eqs. (2.18b) and (2.19)-(2.20), we may write as

$$\begin{aligned} H_{\mathrm{EM}} &= \sum_\mu \epsilon_0 \varepsilon_\mu^2 \left(a_\mu^\dagger a_\mu + a_\mu a_\mu^\dagger \right) \\ &= \sum_\mu \hbar\omega_\mu \left(a_\mu^\dagger a_\mu + \frac{1}{2} \right). \end{aligned} \tag{2.22}$$

The terms $\hbar\omega_\mu/2$ are attributed to the electromagnetic vacuum and are usually omitted [60].

2.2.4 Modeling photonic crystals

The theory of PCs is thoroughly described in the textbook by Joannopoulos *et al.* [64]. In this section we discuss only those elements of the theoretical framework that are needed for the present work. PCs are characterized by a periodic lattice with decorations in the form of a change in permittivity. The lattice is defined by a set of basis vectors $\mathbf{a}_i$ which defines also a set of reciprocal basis vectors $\mathbf{b}_i$ through the relation

$$\mathbf{a}_i \cdot \mathbf{b}_j = 2\pi\delta_{ij}. \tag{2.23}$$

All lattice vectors $\mathbf{R}$ and reciprocal lattice vectors $\mathbf{G}$ may be expanded on the basis vectors and reciprocal basis vectors, respectively, as

$$\mathbf{R} = \sum_i^N a_i\, \mathbf{a}_i \quad \text{and} \quad \mathbf{G} = \sum_i^N b_i\, \mathbf{b}_i,$$

where N denotes the dimensionality of the crystal (typically two or three).

With this notation, the PCs of interest may be characterized completely by the permittivity $\epsilon_{\mathrm{r}}(\mathbf{r}) = \epsilon_{\mathrm{r}}(\mathbf{r} + \mathbf{R})$. Bloch's theorem [64] ensures that the solutions to the wave equation in PCs may be written in the form

$$\mathbf{E}_\mathbf{k}(\mathbf{r}) = e^{i\mathbf{k}\cdot\mathbf{r}} \mathbf{u}_\mathbf{k}(\mathbf{r}), \tag{2.24}$$

in which $\mathbf{u}_\mathbf{k}(\mathbf{r} + \mathbf{R}) = \mathbf{u}_\mathbf{k}(\mathbf{r})$ for all lattice vectors $\mathbf{R}$. Due to the Bloch form of the solution, we focus the analysis to wave vectors $\mathbf{k}$ in the first Brillouin zone of the reciprocal lattice, defined as the set of points closer to $\mathbf{k} = 0$ than to any other

reciprocal lattice site (the central Voronoi cell). For any wave vector $\mathbf{k}'$ there exists a reciprocal lattice vector $\mathbf{G}$ so that $\mathbf{k}' = \mathbf{k} + \mathbf{G}$ with $\mathbf{k}$ in the first Brillouin zone. Inserting in Eq. (2.24) we have

$$\mathbf{E}_{\mathbf{k}'}(\mathbf{r}) = e^{i\mathbf{k}\cdot\mathbf{r}}\mathbf{u}_{\mathbf{k}'}(\mathbf{r})e^{i\mathbf{G}\cdot\mathbf{r}} \tag{2.25}$$

which is itself a valid Bloch mode of the form in Eq. (2.24) since from Eq. (2.23) it follows that $\mathbf{G}\cdot\mathbf{R} = 2\pi M$ with integer M and hence

$$\mathbf{u}_{\mathbf{k}'}(\mathbf{r}+\mathbf{R})e^{i\,\mathbf{G}\cdot(\mathbf{r}+\mathbf{R})} = \mathbf{u}_{\mathbf{k}'}(\mathbf{r})e^{i\,\mathbf{G}\cdot\mathbf{r}}.$$

Although the solutions in Eqs. (2.24) and (2.25) have the same form they are not the same solutions. Hence, they do not necessarily have the same frequencies but rather belong to different bands of the PC band structure, and we shall therefore index the modes by the wave vector $\mathbf{k}$ as well as the band number n so that Eq. (2.6) takes the form

$$\nabla\times\nabla\times\mathbf{E}_{n,\mathbf{k}}(\mathbf{r}) = \frac{\omega_n^2(\mathbf{k})}{c^2}\epsilon_{\mathrm{r}}(\mathbf{r})\mathbf{E}_{n,\mathbf{k}}(\mathbf{r}). \tag{2.26}$$

Due to the symmetries of the lattice, solutions at different $\mathbf{k}$ points may have identical frequencies. An obvious example is time-reversal symmetry which holds for all photonic crystals of interest in this work. It leads to the physically quite reasonable condition that waves traveling in exact opposite directions will have identical frequencies; $\omega_n(\mathbf{k}) = \omega_n(-\mathbf{k})$ [64]. In order to remove redundancy due to symmetry, investigations are typically restricted to the boundaries of the irreducible Brillouin zone. This is defined as the set of points in the Brillouin zone for which the solutions $\mathbf{E}_{n,\mathbf{k}}(\mathbf{r})$, with corresponding eigenfrequencies $\omega_n(\mathbf{k})$, are not related to the solutions at other $\mathbf{k}$ points via any of the symmetries of the lattice.

The PC band structures are typically calculated as the eigenvalues of the electromagnetic wave equation with periodic permittivity, $\epsilon_{\mathrm{r}}(\mathbf{r}) = \epsilon_{\mathrm{r}}(\mathbf{r}+\mathbf{R})$, under the assumption that the solutions have Bloch form, Eq. (2.24). For calculations on non-magnetic materials it is easier to work with the wave equation for the $\mathbf{H}_{\mathbf{k}}(\mathbf{r})$ field which, under the assumption $\mathbf{H}_{\mathbf{k}}(\mathbf{r}) = \exp(i\mathbf{k}\cdot\mathbf{r})\mathbf{u}_{\mathbf{k}}(\mathbf{r})$, reduces to the form

$$(i\mathbf{k}+\nabla)\times\frac{1}{\epsilon_{\mathrm{r}}(\mathbf{r})}(i\mathbf{k}+\nabla)\times\mathbf{u}_{\mathbf{k}}(\mathbf{r}) = \frac{\omega^2(\mathbf{k})}{c^2}\mathbf{u}_{\mathbf{k}}(\mathbf{r}). \tag{2.27}$$

For a given material distribution $\epsilon_{\mathrm{r}}(\mathbf{r})$, Eq. (2.27) may be discretized and solved using any suitable numerical method.

2.2.5 An overview of existing calculation methods

A large number of different methods are being explored in the investigation of light propagation in microstructured materials such as photonic crystals. In order to re-

late the methods that we have used in this project to other methods in the literature, we give in this section an overview of relevant existing calculation methods.

Finite Difference Time-Domain calculations

The Finite Difference Time-Domain (FDTD) method [65] is the workhorse of many light propagation calculations and is regularly employed in the design of PC structures. Although originally developed for electromagnetic problems it has applications in other areas including quantum mechanics [66]. We shall focus only on applications with relation to our work, namely band structure calculations and calculations of the Green's tensor and LDOS.

As an alternative to the formulation in terms of an eigenvalue equation, as in Eq. (2.27), one can employ FDTD calculations in order to trace out the band diagram. In this approach, so-called Bloch boundary conditions are enforced on the FDTD calculation domain in order to make the field conform to the Bloch form, Eq. (2.24). Using a collection of randomly distributed broad band sources, all relevant modes of the system are excited and allowed to propagate for a sufficiently long time that a subsequent Fourier transform will reveal only the strongest resonances of the system. These correspond to the eigenmodes, and the FDTD approach thus offers an alternative to the formulations based on Eq. (2.27). In section 5.2 we use both plane wave calculations and the FDTD method to calculate the band structure of a photonic crystal slab.

FDTD has been used for calculations of the LDOS in photonic crystals; notably in Ref. [67] where the Purcell effect due to the mode in a PC wave guide was calculated using FDTD. The need for defining proper boundary conditions such as perfectly matched layers make FDTD calculations in periodic structures complicated, and the method may be restricted to problems with well defined modes such as wave guides. For finite sized structures this problem does not arise, and FDTD has been used for the calculation of the LDOS in photonic crystallites [68] and finite sized waveguides [35].

For Calculations of the Green's tensor using FDTD the system is excited by a broad band point source at a given location $\mathbf{r}'$ and the system is evolved in time through Maxwell's equations and monitored at any position $\mathbf{r}$ within the calculation domain. In this case Eq. (2.12) establishes the connection between the measured field and the source from which the Green's tensor is derived. This procedure is used for the calculation of the Green's tensor in a PC slab in section 5.2. Although it is a stable and well established method, FDTD is extremely demanding in terms of both memory and time, easily reaching runtimes of several days for practically relevant structures.

Plane wave expansion

Plane wave expansion of Eq. (2.27) has been widely used for the study of photonic crystals through band structure calculations [69, 70]. In plane wave calculations, the fields $\mathbf{u_k}(\mathbf{r})$ and the inverse permittivity $\epsilon_r(\mathbf{r})^{-1}$ are expanded on lattice plane waves as

$$\mathbf{u_k}(\mathbf{r}) = \sum_{\mathbf{G}} \mathbf{u_G}(\mathbf{k}) e^{i\,\mathbf{G}\cdot\mathbf{r}} \quad \text{and} \quad \frac{1}{\epsilon_r(\mathbf{r})} = \sum_{\mathbf{G}} \eta_{\mathbf{G}} e^{i\,\mathbf{G}\cdot\mathbf{r}}, \tag{2.28}$$

and the accuracy is thus set by the calculation of the matrix elements $\mathbf{u_G}$ and $\eta_{\mathbf{G}}$ as well as the number of plane waves as controlled by the cutoff in the wave vectors $\mathbf{G}$. Due to the particular choice of expansions, the plane wave method is fine for full three-dimensional photonic crystals but does lead to problems in calculations on PC slabs where the analysis is limited to modes below the light-line [71].

The LDOS for photonic crystals has previously been investigated using plane wave expansions [72, 73, 74] in which the modes were found as the solutions to Eq. (2.28) and summed according to Eq. (2.8).

Multipole methods

The Generalized Multipole Technique [75] employs an expansion of the electromagnetic field in terms of so-called multipoles that are solutions to the wave equation in spherical coordinates (cylindrical coordinates in two dimensions). The expansion is performed in each region of the material, and a set of linear equations for the expansion coefficients is obtained by imposing proper boundary conditions for the fields. Since the basis functions are solutions to the wave equation, Maxwell's equations are automatically fulfilled within each region, and an error estimate can be obtained by evaluating to what degree the boundary conditions are met.

For calculations involving large numbers of scatterers in an otherwise homogeneous background, Rayleigh-multipole methods have been used for calculations on microstructured fibres [76, 77, 78, 79] as well as photonic crystals composed of cylinders [80, 81] or spheres [82, 83]. The use of multipole expansions for the fields ensures a significant reduction in the number of basis functions, thus enabling calculations on complex structures of practical interest. For simple scatterers, analytical expressions for the expansion coefficients are available which significantly increases calculation speeds and accuracy.

Method of moments and the coupled dipole approximation

The Lippmann-Schwinger equation is an example of a volume integral equation for the electric field. Various volume and surface integral methods exist for the electric and magnetic fields. These methods typically rely on discretization to express the

integrals as linear systems of equations - a procedure known as the method of moments. In the discretization process the solution is expanded in terms of linearly independent basis functions which vary in complexity depending on the specific method employed [84]. A particularly simple and convenient choice of basis function is the pulse basis function, but higher order basis functions have been applied [85]. The application of pulse basis functions to the Lippmann-Schwinger equation results in what is usually termed the coupled (or discrete) dipole approximation (CDA) [86, 87].

The CDA allows for relatively easy implementation as well as the physically attractive property that the resulting field can be directly interpreted as the sum of the field from all the individual cells in the scattering structure oscillating as dipoles in response to the incoming field. However, depending on the desired accuracy and the nature of the scattering problem at hand, the required number of basis functions may become too large for practical calculations on e.g. photonic crystals. In addition, this type of discretization may lead to stability problems which, for example, limit the efficiency in the case of high refractive index contrasts [84].

The CDA has previously been applied to two dimensional scattering problems in inhomogeneous backgrounds [88], and the application of the CDA to the calculation of the Green's tensor in a photonic crystal slab was reported in Ref. [89]. In Refs [90, 91] an iterative scheme was suggested for the solution of the Lippmann-Schwinger equation which has been applied also for the calculation of light propagation in finite sized photonic crystals [92]. This elegant formulation is based on the combined use of the Lippmann-Schwinger equation and the Dyson equation to solve the linear equation system. However, the number of operations scales as $\mathcal{O}(N^3)$. This means that the method is similar in performance to most traditional solvers whereas advanced solvers may show better performance [84].

Other methods

Other numerical methods of great importance in modeling of optical devices include the Finite Element Method (FEM) [93]. Like FDTD, the FEM is a brute force numerical technique that can handle many different geometries. In addition, very efficient matrix inversion algorithms are available for the sparse matrix equation system resulting from typical FEM discretization. For three dimensional calculations, however, the memory requirements for solution of the full vector field problem may become too large for many applications.

Last, we note that the expansion in Eq. (2.13) has been used for derivations of analytical approximations to the Green's tensor in optical wave guides and microcavities [94, 95, 96].

2.3 Quantum dot models

QDs allow for confinement of carrier motion to limited regions of the host dielectric. This leads to a quantization of the allowed energy levels as known from atomic physics but realized in semiconductor materials. The energy level structure can therefore in principle be engineered by changing the QD size and shape. In semiconductors, excitations appear as the creation of an electron-hole pair subject to a number of many particle effects, e.g. coulomb interaction. However, for most modeling purposes we may simply regard the QD as a two level system with a ground state and an excited state, similar to the electronic states of an atom. Also, as in the case of atoms, the QDs have an intrinsic dipole moment. Although we will effectively model the QDs as two-level systems with parameters taken from measurements, in this section we will discuss some aspects of QD modeling in order to illustrate the theoretical foundations.

As a starting point we consider a perfect semiconductor crystal in the ground state for which all states in the valence band are filled and all states in the conduction band are empty. This is the so-called Fermi vacuum $|\mathcal{F}\rangle$ [97]. We describe the electronic properties of the semiconductors close to the band extrema in which the parabolic approximation is valid. The extrema are found at $\mathbf{k} = 0$ for materials of interest in this work. The electrons in the perfect crystal are described by the Hamiltonian H_C which includes all many body effects such as coulomb interaction between all electrons and nuclei.

We model excitations, such as created by the pump laser in the experiment in section 1.1, by the removal of an electron in the valence band and the simultaneous creation of an electron in the conduction band, as illustrated in Fig. 2.1. Semiconductor theory and effective mass theory suggests that the missing electron

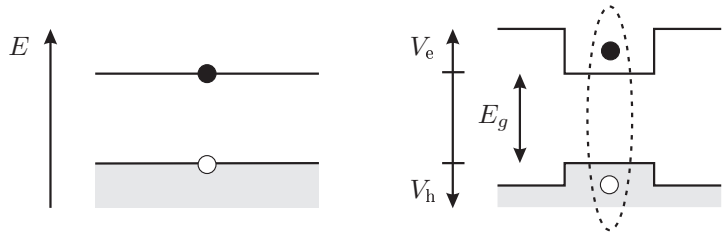

Figure 2.1: Left: An excitation in the bulk semiconductor consisting of an electron in the conduction band and a hole in the valence band. Right: By the inclusion of Coulomb interaction an exciton is formed. In addition, the QD geometry leads to confinement potentials V_e and V_h for the electron and hole, respectively.

in the valence band be treated as a hole with positive charge and negative mass. The excitation event thus creates the state

$$|X_{\mathbf{k}_\mathrm{e},\mathbf{k}_\mathrm{h}}\rangle = c^\dagger_{\mathrm{e},\mathbf{k}_\mathrm{e}} c^\dagger_{\mathrm{h},\mathbf{k}_\mathrm{h}} |\mathcal{F}\rangle \tag{2.29}$$

where $c^\dagger_{\mathrm{e},\mathbf{k}}$ and $c^\dagger_{\mathrm{h},\mathbf{k}}$ denote electron and hole creation operators, respectively [97]. Being fermion operators, these satisfy anticommutation relations,

$$\{c_{n,\mathbf{k}}, c^\dagger_{m,\mathbf{k}'}\} = \delta_{n,m}\delta(\mathbf{k}-\mathbf{k}'), \quad m,n \in \{\mathrm{e},\mathrm{h}\}. \tag{2.30}$$

Due to the infinite periodic lattice, the single-particle wave functions may be indexed by the wave vector $\mathbf{k}$, and owing to Bloch's theorem they may be written in the form

$$\begin{aligned}\varphi_{n,\mathbf{k}}(\mathbf{r}) &= \langle \mathbf{r}|c^\dagger_{n,\mathbf{k}}|\mathcal{F}\rangle \\ &= \frac{e^{i\mathbf{k}\cdot\mathbf{r}}}{\sqrt{V}} u_{n,\mathbf{k}}(\mathbf{r}),\end{aligned} \tag{2.31}$$

in which V is the volume of the crystal and $u_{n,\mathbf{k}}$ has the periodicity of the lattice.

The states $|X_{\mathbf{k}_\mathrm{e},\mathbf{k}_\mathrm{h}}\rangle$ are eigenstates of the Hamiltonian for the perfect crystal H_C. Due to the difference in charge, we model the electron-hole system by adding an attractive Coulomb interaction term. To model confinement within the QD we will add also a potential in both the conduction band and the valence band, as indicated in Fig. 2.1. The additional terms in the Hamiltonian ruins the symmetry of the perfect lattice, and as a consequence the eigenstates are no longer defined by a single wave vector. In this case we may expand the eigenstates of the full Hamiltonian as a superposition of the excitations in Eq. (2.29) as

$$|X\rangle = \sum_{\mathbf{k}_\mathrm{e},\mathbf{k}_\mathrm{h}} \chi(\mathbf{k}_\mathrm{e},\mathbf{k}_\mathrm{h}) c^\dagger_{\mathrm{e},\mathbf{k}_\mathrm{e}} c^\dagger_{\mathrm{h},\mathbf{k}_\mathrm{h}} |\mathcal{F}\rangle, \tag{2.32}$$

and by projecting onto the position eigenvectors and using the Bloch form of the solutions in the perfect lattice we obtain the exciton wave function

$$\begin{aligned}X(\mathbf{r}_\mathrm{e},\mathbf{r}_\mathrm{h}) &= \langle \mathbf{r}_\mathrm{e},\mathbf{r}_\mathrm{h}|X\rangle \\ &= \sum_{\mathbf{k}_\mathrm{e},\mathbf{k}_\mathrm{h}} \chi(\mathbf{k}_\mathrm{e},\mathbf{k}_\mathrm{h}) \langle \mathbf{r}_\mathrm{e},\mathbf{r}_\mathrm{h}|c^\dagger_{\mathrm{e},\mathbf{k}_\mathrm{e}} c^\dagger_{\mathrm{h},\mathbf{k}_\mathrm{h}}|\mathcal{F}\rangle \\ &= \frac{1}{V}\sum_{\mathbf{k}_\mathrm{e},\mathbf{k}_\mathrm{h}} \chi(\mathbf{k}_\mathrm{e},\mathbf{k}_\mathrm{h}) e^{i\mathbf{k}_\mathrm{e}\cdot\mathbf{r}_\mathrm{e}} u_{\mathrm{e},\mathbf{k}_\mathrm{e}}(\mathbf{r}_\mathrm{e}) e^{i\mathbf{k}_\mathrm{h}\cdot\mathbf{r}_\mathrm{h}} u_{\mathrm{h},\mathbf{k}_\mathrm{h}}(\mathbf{r}_\mathrm{h}) \\ &= \chi(\mathbf{r}_\mathrm{e},\mathbf{r}_\mathrm{h}) u_{\mathrm{e},0}(\mathbf{r}_\mathrm{e}) u_{\mathrm{h},0}(\mathbf{r}_\mathrm{h}),\end{aligned} \tag{2.33}$$

where we have evaluated the lattice-periodic functions $\mathbf{u}_{n,\mathbf{k}}$ at $\mathbf{k} = 0$, which is reasonable for excitations close to the band edge, and we have identified the sum as

the two-dimensional Fourier transform of the function $\chi(\mathbf{k}_\mathrm{e}, \mathbf{k}_\mathrm{h})$. The two-particle exciton wave function $\chi(\mathbf{r}_\mathrm{e}, \mathbf{r}_\mathrm{h})$ solves the effective mass equation [98, 99]:

$$H(\mathbf{r}_\mathrm{e}, \mathbf{r}_\mathrm{h})\chi(\mathbf{r}_\mathrm{e}, \mathbf{r}_\mathrm{h}) = E\chi(\mathbf{r}_\mathrm{e}, \mathbf{r}_\mathrm{h}), \tag{2.34}$$

in which E is the energy and

$$H(\mathbf{r}_\mathrm{e}, \mathbf{r}_\mathrm{h}) = E_\mathrm{g} + \frac{\mathbf{p}_\mathrm{e}^2}{2m_\mathrm{e}^*} + \frac{\mathbf{p}_\mathrm{h}^2}{2m_\mathrm{h}^*} + V_\mathrm{e}(\mathbf{r}_\mathrm{e}) + V_\mathrm{h}(\mathbf{r}_\mathrm{h}) - \frac{q^2}{4\pi\epsilon_0\epsilon_\mathrm{r}|\mathbf{r}_\mathrm{e} - \mathbf{r}_\mathrm{h}|},$$

where E_g is the band gap and $\mathbf{p}_n$ and m_n^* denote momentum operators and electron or hole effective masses, respectively. V_e and V_h are the confinement potentials for electrons and holes, as indicated in Fig. 2.1. The last term represents the attractive Coulomb potential in which $q = -1.602 \times 10^{-19}$ C is the electron charge.

Depending on the relative size of the Coulomb interaction and the particular form of the confinement potentials, the solution to Eq. (2.34) takes on a number of different forms. In the limit of zero confinement, the solutions are Wannier excitons for which the wave functions are given in terms of center of mass and relative coordinates with a characteristic Bohr radius,

$$a_0 = \frac{4\pi\hbar^2\epsilon_0\epsilon_\mathrm{r}}{q^2 m_\mathrm{R}^*},$$

where $m_\mathrm{R}^* = m_\mathrm{e}^* m_\mathrm{h}^*/(m_\mathrm{e}^* + m_\mathrm{h}^*)$ is the reduced mass [98].

For non-zero confinement potentials, an explicit model for $V_\mathrm{e}(\mathbf{r}_\mathrm{e})$ and $V_\mathrm{h}(\mathbf{r}_\mathrm{h})$ is needed. A strong and a weak coupling regime may be defined on the basis of the confinement energy relative to the exciton binding energy or, equivalently, the size of the QD relative to the Bohr radius [100]. In the strong coupling regime the Coulomb interaction may be ignored and Eq. (2.34) is separable in electron and hole parts that depend only on $\mathbf{r}_\mathrm{e}$ and $\mathbf{r}_\mathrm{h}$, respectively. In this case the solutions are products of solutions to the single-particle Schrödinger equation in the effective mass approximation,

$$\chi(\mathbf{r}_\mathrm{e}, \mathbf{r}_\mathrm{h}) = \psi_\mathrm{e}(\mathbf{r}_\mathrm{e})\psi_\mathrm{h}(\mathbf{r}_\mathrm{h}).$$

For most materials of interest these are relatively easy problems to solve using numerical methods, e.g. FEM [101, 102]. The correspondence between results from these simple numerical models and measurable quantities such as energy and oscillator strength has been tested with good agreement [1].

An interesting model has been presented by Sugawara [103] in which the in-plane potential of a QD is modeled with a parabolic potential and infinite potential barriers are used in the out of plane direction. In this case Eq. (2.34) is solvable with analytical solutions spanning both the weak and the strong coupling regimes.

For most calculations we will not be concerned with the explicit form of the exciton state but simply define an exciton creation operator through the sum in Eq. (2.32) and write the exciton state formally as

$$|X\rangle = b_x^\dagger |\mathcal{F}\rangle.$$

The exciton, by definition, is an eigenstate of the Schrödinger equation $H_{\mathrm{QD}}|X\rangle = \hbar\omega_x|X\rangle$ and we may conveniently write the Hamiltonian as

$$H_{\mathrm{QD}} = \sum_x \hbar\omega_x b_x^\dagger b_x, \tag{2.35}$$

where the sum runs over all excitons. Being composed of electron and hole creation operators, the exciton operators inherit the fermion anticommutation relations,

$$\{b_x, b_y^\dagger\} = \delta_{x,y}.$$

2.4 Coupling formalisms

Having discussed calculation of light propagation and scattering as well as QD models, we now turn to formalisms related to the coupling of light and matter. We shall be concerned with systems containing a single excitation only. In this case, for the coupled system, we are interested in properties connected to the composite state

$$|\Psi\rangle = \sum_x c_x|x,0\rangle + \sum_\mu c_\mu|0,\mu\rangle$$

where $|x,0\rangle = b_x^\dagger|\mathcal{F}\rangle$ denotes the state with one exciton in QD x and no photons and similarly $|0,\mu\rangle = a_\mu^\dagger|\mathcal{F}\rangle$ denotes the state with no excitons and one photon in mode μ.

With the above choice of state we are effectively working in the one-excitation subspace of the entire Hilbert space. This potentially limits the validity of the calculations, so a motivation and discussion of the sufficiency of calculations in this subspace is in order. The choice of a single excitation in the system is reasonable for calculations in connection with experiments such as the one described in Section 1.1, since the excitation power was kept well below one excitation per QD. For higher excitation powers, the probability of bi-exciton states would be non-negligible, and we would have to expand the basis set in order to get an adequate description. Even with only one excitation in the system, quantum mechanics allows for the excitation of virtual states on short time scales. However, the restriction of the analysis to the one-excitation subspace corresponds essentially to the rotating wave approximation in which one keeps in the equations only terms corresponding to energy conserving transitions [104].

Physical observables will depend on the state $|\Psi\rangle$ as well as the time-evolution governed by the interaction Hamiltonian. Below, we discuss first the interaction Hamiltonian. Afterwards, in section 2.4.2, we will discuss the derivation of the equations of motion in the Schrödinger and Heisenberg pictures. In addition to the distinction between Schrödinger and Heisenberg pictures, quantum optical calculations of light-matter interaction are typically carried out in one of two pictures with respect to the objective. One can work in an all matter picture in which the electromagnetic field is integrated out to reveal the dynamics of the atom or QD. Alternatively, one can work in an all light picture in which the atomic dynamics are integrated out to get the temporal behavior of the light at given positions [48]. The two pictures are complementary, and the choice of Hamiltonian as well as the formulation of the equations of motion will depend on the objective. In section 2.4.3 we set up equations of motion for the internal QD dynamics in the Schrödinger picture, and in section 2.4.4 we consider the field from a quantum emitter in the Heisenberg picture.

2.4.1 Interaction Hamiltonian

The interaction Hamiltonian in quantum optics is the subject of some controversy in that it is typically formulated in one of two ways. The minimal coupling Hamiltonian is formulated in terms of the vector and scalar potentials $\mathbf{A}$ and Φ and reads [61]

$$\begin{aligned} H_{\text{int}} &= \frac{1}{2m_0}\left(\mathbf{p} - q\mathbf{A}\right)^2 + V(\mathbf{r}) + q\Phi + \frac{1}{2}\int \epsilon_0\epsilon_{\text{r}}(\mathbf{r})E^2 + \frac{1}{\mu_0}B^2 \mathrm{d}\mathbf{r} \\ &= H_{\text{EM}} + H_{\text{QD}} - \frac{q}{2m_0}\left(\mathbf{p}\cdot\mathbf{A} + \mathbf{A}\cdot\mathbf{p}\right) + \frac{q^2}{2m_0}\mathbf{A}^2 + q\Phi, \end{aligned} \tag{2.36}$$

where we have identified the Hamiltonians for the uncoupled electromagnetic field and QDs, cf. Eqs. (2.22) and (2.35). Using the generalized Coulomb gauge

$$\nabla\cdot\left(\epsilon_{\text{r}}(\mathbf{r})\mathbf{A}(\mathbf{r})\right) = 0 \quad \text{and} \quad \Phi = 0$$

and dropping the small $q^2\mathbf{A}^2$ term, the interaction part is usually rewritten in the form

(Minimal Coupling)
$$H_{\text{int}}^{\text{min}} = -\frac{q}{m_0}\mathbf{p}\cdot\mathbf{A}. \tag{2.37}$$

Instead of the minimal coupling Hamiltonian, the so-called multipolar Hamiltonian is often used in quantum optics calculations. In this formulation the carriers couple to the displacement field $\mathbf{D} = \epsilon_0\epsilon_{\text{r}}(\mathbf{r})\mathbf{E} + \mathbf{P}_{\mathbf{ex}}$ [105], where $\mathbf{P}_{\mathbf{ex}}$ describes the extrinsic polarization due to the carriers in the QD, cf. Eq. (2.9). In the dipole approximation, the multipolar Hamiltonian reads

(Dipole)
$$H_{\text{int}}^{\text{dip}} = -q\mathbf{r}\cdot\mathbf{D}/\epsilon_0\epsilon_{\text{r}}(\mathbf{r}). \tag{2.38}$$

Often the dipole Hamiltonian is expressed in terms of the electric field only, thus neglecting the extrinsic polarization due to the excitons themselves. In order to account for the extrinsic polarization, a slightly different formulation in terms of an auxiliary field $\mathbf{F} = \mathbf{D}/\epsilon_0\epsilon_\mathrm{r}(\mathbf{r})$ was used in Ref. [48].

Starting on a fundamental level, one can show that the Lagrangians of the minimal coupling Hamiltonian and the multipolar Hamiltonian are equal up to a total time derivative. This means that although the Hamiltonians are different in form they must be connected by a canonical transformation and thus must lead to the same physics [61]. However, if one makes approximations to the Hamiltonians (such as the dipole approximation) they may lead to different results. This is similar to the fact that two different series that give the same sum are likely to give different sums if they are truncated.

2.4.2 Equations of motion

Central to quantum mechanical calculations is the historical and fundamental choice between the two different viewpoints of the Schrödinger picture, in which the quantum mechanical state carries the time evolution, and the Heisenberg picture, in which the time evolution is contained in the operators [97].

In the Schrödinger picture the time-evolution is governed by the Schrödinger equation

$$i\hbar\frac{\partial}{\partial t}|\Psi(t)\rangle_\mathrm{S} = H|\Psi(t)\rangle_\mathrm{S},$$

and we write the general state as

$$\begin{aligned}|\Psi(t)\rangle_\mathrm{S} &= \sum_x c_x(t)|x,0\rangle + \sum_\mu c_\mu(t)|0,\mu\rangle \\ &= \sum_x c_x^\mathrm{I}(t)e^{-i\omega_x t}|x,0\rangle + \sum_\mu c_\mu^\mathrm{I}(t)e^{-i\omega_\mu t}|0,\mu\rangle,\end{aligned}$$

where we have written explicitly the time dependence of the expansion coefficients due to the Hamiltonian $H_0 = H_\mathrm{QD} + H_\mathrm{EM}$ of the uncoupled system. In the uncoupled system this is the only time-dependence and c_x and c_μ are constants.

Typically in calculations of light-matter interaction, a so-called interaction picture is introduced in which the state carries the time evolution due to the interaction only and thus ignoring fast oscillations due to the bare energies of the uncoupled system [104]. In the interaction picture, the general state is written as

$$\begin{aligned}|\Psi\rangle_\mathrm{I} &= \exp\left(\frac{i}{\hbar}H_0 t\right)|\Psi\rangle_\mathrm{S} \\ &= \sum_x c_x^\mathrm{I}(t)|x,0\rangle + \sum_\mu c_\mu^\mathrm{I}(t)|0,\mu\rangle\end{aligned}$$

and evolves in time according to the equation

$$i\hbar\frac{\partial}{\partial t}|\Psi\rangle_{\mathrm{I}} = H_{\mathrm{I}}|\Psi\rangle_{\mathrm{I}},$$

where the interaction picture Hamiltonian is given as

$$H_{\mathrm{I}} = \exp\left(\frac{i}{\hbar}H_0 t\right) H_{\mathrm{int}} \exp\left(-\frac{i}{\hbar}H_0 t\right).$$

Inserting the state in the interaction picture Schrödinger equation and projecting onto the basis states $|x,0\rangle$ and $|0,\mu\rangle$ we obtain the equations of motion for the expansion coefficients

$$\dot{c}_x^{\mathrm{I}}(t) = -\frac{i}{\hbar}\sum_{\mu}\langle x,0|H_{\mathrm{I}}|0,\mu\rangle c_\mu^{\mathrm{I}} \tag{2.39a}$$

$$\dot{c}_\mu^{\mathrm{I}}(t) = -\frac{i}{\hbar}\sum_{x}\langle 0,\mu|H_{\mathrm{I}}|0,x\rangle c_x^{\mathrm{I}}. \tag{2.39b}$$

In the Heisenberg picture, we solve for the time evolution of the general operator $\mathcal{O}$ based on the Heisenberg equations of motion.

$$i\hbar\frac{\partial}{\partial t}\mathcal{O} = [\mathcal{O}, H].$$

In particular, we may solve for the time evolution of the annihilation operators b_x and a_μ in which case we find

$$\dot{b}_x = -i\omega_x b_x - \frac{i}{\hbar}[b_x, H_{\mathrm{int}}] \tag{2.40a}$$

$$\dot{a}_\mu = -i\omega_\mu a_\mu - \frac{i}{\hbar}[a_\mu, H_{\mathrm{int}}], \tag{2.40b}$$

with the adjoint equations providing the time dependence of the creation operators.

2.4.3 Quantum dot decay dynamics in the Schrödinger picture

This section describes the calculation of QD decay dynamics in the Schrödinger picture. The analysis follows the general method outlined in Ref. [62] which elegantly demonstrates how the QD dynamics are governed only by the local electromagnetic properties of the medium as described by the LDOS. In chapter 4 we will use this general formalism for the detailed analysis of non-Markovian decay in photonic crystals.

We consider the decay of a single QD that we model as a two-level system as discussed in section 2.3. For the analysis we use the minimal coupling Hamiltonian

in the dipole approximation where the size of the QD (or the size of the exciton wave function) is assumed to be small compared to variations in the vector potential so that we may set $\mathbf{f}_\mu(\mathbf{r}) = \mathbf{f}_\mu(\mathbf{r}_{\mathrm{QD}}) = \mathbf{f}_{\mu,0}$. The typical procedure is now to expand the momentum operator in the states $|X\rangle$ and $|\mathcal{F}\rangle$ as

$$\mathbf{p} = \mathbf{p}_{\mathcal{F}X}|\mathcal{F}\rangle\langle X| + \mathbf{p}_{X\mathcal{F}}|X\rangle\langle\mathcal{F}| = \mathbf{p}_x b_x + \mathbf{p}_x^* b_x^\dagger$$

where $\mathbf{p}_{ij} = \langle i|\mathbf{p}|j\rangle$ are momentum matrix elements and where we have set $\mathbf{p}_{XX} = \mathbf{p}_{\mathcal{F}\mathcal{F}} = 0$ (see below). In this way we write the interaction Hamiltonian as

$$H_{\mathrm{int}} = -\frac{q}{m_0}\sum_\mu \frac{\varepsilon_\mu}{\omega_\mu}\left(\mathbf{p}_x b_x + \mathbf{p}_x^* b_x^\dagger\right)\cdot\left(\mathbf{f}_{\mu,0} a_\mu + \mathbf{f}_{\mu,0}^* a_\mu^\dagger\right)$$

from which the interaction picture Hamiltonian follows:

$$H_{\mathrm{I}} = -\frac{q}{m_0}\sum_\mu \frac{\varepsilon_\mu}{\omega_\mu}\left(\mathbf{p}_x \mathbf{b}_x e^{-i\omega_x t} + \mathbf{p}_x^* b_x^\dagger e^{i\omega_x t}\right)\cdot\left(\mathbf{f}_{\mu,0} a_\mu e^{-i\omega_\mu t} + \mathbf{f}_{\mu,0}^* a_\mu^\dagger e^{i\omega_\mu t}\right).$$

In the rotating wave approximation we drop the two fast oscillating terms and keep only the two terms oscillating at the angular difference frequency $\Delta_\mu = \omega_\mu - \omega_x$ to arrive at the final form of the interaction picture Hamiltonian,

$$H_{\mathrm{I}} = -\hbar\sum_\mu \left(g_\mu b_x^\dagger a_\mu e^{-i\Delta_\mu} + g_\mu^* b_x a_\mu^\dagger e^{i\Delta_\mu}\right), \tag{2.41}$$

where

$$g_\mu = \frac{q}{m_0}\frac{p_x^*}{\sqrt{2\hbar\epsilon_0\omega_\mu}}\,\mathbf{e}_x\cdot\mathbf{f}_{\mu,0}.$$

As expected, the interaction picture Hamiltonian in the rotating wave approximation involves only energy conserving terms. Therefore, if we pump the system with only one quantum of energy the dynamics are restricted to the one-excitation subspace. In the above derivation we assumed that $\mathbf{p}_{XX} = \mathbf{p}_{\mathcal{F}\mathcal{F}} = 0$. Typically, for light-matter calculations in atomic physics, the symmetry of the electron wave functions are used to argue that this is the case. The self-assembled QDs are not spherically symmetric, and so this argument does not hold. However, if we had retained the two additional terms, these would have resulted in terms in the interaction picture Hamiltonian oscillating at the angular frequency ω_μ and thus would have been dropped in the rotating wave approximation. Also, these terms would not appear if we expanded the interaction Hamiltonian in the one-excitation subspace, since they correspond to the process of annihilation or creation of a photon without the creation or annihilation of an exciton.

With the interaction picture Hamiltonian, Eq. (2.41), the equations of motion take on the simple form

$$\dot{c}_x^{\mathrm{I}} = i \sum_\mu c_\mu^{\mathrm{I}} g_\mu e^{-i\Delta_\mu t} \tag{2.42a}$$

$$\dot{c}_\mu^{\mathrm{I}} = i\, c_x^{\mathrm{I}}\, g_\mu^*\, e^{i\Delta_\mu t}, \tag{2.42b}$$

from which we find, by integration of Eq. (2.42b) and insertion into Eq. (2.42a), the equation of motion for the expansion coefficient c_x^{I}:

$$\dot{c}_x^{\mathrm{I}} = -\sum_\mu |g_\mu|^2 \int_0^t c_x^{\mathrm{I}}(t') e^{-i\Delta_\mu (t-t')} \mathrm{d}t'.$$

From the discussion in section 1.1 the decay is expected to depend on properties of both the QD and the electromagnetic environment. The physical details of the coupling is hidden in the parameter $|g_\mu|^2$. In order to make the dependence on the LDOS explicit we follow Ref. [62] and add an integral over a Dirac δ-function to rewrite the expression as

$$\begin{aligned}\dot{c}_x^{\mathrm{I}}(t) &= -\alpha \sum_\mu \int_0^\infty \frac{|\mathbf{e}_x \cdot \mathbf{f}_{\mu,0})|^2}{\omega} \int_0^t c_x^{\mathrm{I}}(t')\, e^{-i(\omega-\omega_x)(t-t')} \mathrm{d}t'\, \delta(\omega-\omega_\mu)\, \mathrm{d}\omega \\ &= -\alpha \int_0^\infty \int_0^t c_x^{\mathrm{I}}(t')\, e^{-i(\omega-\omega_x)(t-t')}\, \frac{\rho_x(\omega, \mathbf{r}_{\mathrm{QD}})}{\omega}\, \mathrm{d}t'\, \mathrm{d}\omega, \end{aligned} \tag{2.43}$$

in which $\alpha = q^2 p^2 / 2\hbar m^2 \epsilon_0$ and $\rho_x(\omega, \mathbf{r})$ is the projected LDOS, Eq. (2.8). From Eq. (2.43) we can now directly appreciate how the LDOS governs the QD decay dynamics, as discussed in section 1.2.4.

The Wigner-Weisskopf approximation

If we assume that the LDOS varies slowly across the spectral linewidth of the emitter we may evaluate it at $\omega = \omega_x$ and pull it outside the integral in Eq. (2.43). This assumption is valid for a large set of materials because of the oscillatory term in the integral which will average to zero for frequencies much larger or smaller than $\omega = \omega_x$. With this assumption we lower the limit in the frequency integral to $-\infty$ and rewrite the integral as

$$\begin{aligned}\dot{c}_x^{\mathrm{I}}(t) &\approx -\alpha\, \frac{\rho_x(\omega_x)}{\omega_x} \int_0^t c_x^{\mathrm{I}}(t') \int_{-\infty}^\infty e^{-i(t-t')(\omega-\omega_x)} \mathrm{d}\omega \mathrm{d}t' \\ &= -\alpha\, \frac{\rho_x(\omega_x)}{\omega_x} \int_0^t c_x^{\mathrm{I}}(t')\, 2\pi\delta(t'-t) \mathrm{d}t' \\ &= -\frac{\Gamma}{2} c_x^{\mathrm{I}}(t), \end{aligned}$$

which corresponds to an exponential decay with decay constant given as

$$\Gamma = \frac{\pi\, q^2\, p^2}{\hbar\, m_0^2\, \epsilon_0}\, \frac{\rho_p(\omega_x)}{\omega_x}.$$

In the above integration, the δ-function leads to a factor of $1/2$ because it is centered at the end point of the integration interval.

Single-mode field - Vacuum Rabi oscillations

Optical microcavities offer the possibility of enhancing a single mode in a given frequency interval. For such structures the LDOS shows a very sharp peak and may be approximated by a Dirac δ-function of the form

$$\rho_x(\omega) = k\, \delta(\omega - \omega_x),$$

for the case of the emitter being perfectly resonant with the cavity mode. Substituting into Eq. (2.43), the frequency integral is evaluated to reveal the equation:

$$\dot{c}_x^{\mathrm{I}}(t) = -\kappa^2 \int_0^t c_x^{\mathrm{I}}(t')\, \mathrm{d}t',$$

where $\kappa^2 = \alpha\, k/\omega_x$. The solution is harmonic oscillations of the form $c_x^{\mathrm{I}}(t) = \cos(\kappa\, t)$ as can be verified by direct substitution. Introducing a δ-function in the LDOS means that the expansions of the electromagnetic field operators in Eqs. (2.18) reduce to a single term each. In this case it would be more natural to use a Jaynes-Cummings model [106] to solve the equations of motion instead of the more general method presented here.

2.4.4 Field from quantum emitter in the Heisenberg picture

In section 2.2.1 the electric field from a polarization point source was expressed in a simple and compact form in Eq. (2.12) based on the electromagnetic Green's tensor. It is tempting to ask if a similar equation holds for a quantum mechanical emitter in the form of a QD emitting a single photon if we exchange the classical electric field and the polarization by quantum mechanical operators. Using the dipole Hamiltonian and a harmonic oscillator model for the emitter it was shown in Ref. [48] that the answer is positive, provided that the Green's tensor is slightly modified. In this section, following Refs. [57, 95], we discuss the derivation in the framework of fermionic operators.

Expanding the dipole operator $\mathbf{d} = q\mathbf{r}$ on the exciton states we write the dipole Hamiltonian, Eq. (2.38) in the form

$$H_{\mathrm{int}} = -i \sum_{\mu,x} \varepsilon_\mu \left(\mathbf{d}_x b_x + \mathbf{d}_x b_x^\dagger\right) \cdot \left(\mathbf{f}_{\mu,x} a_\mu - \mathbf{f}_{\mu,x}^* a_\mu^\dagger\right),$$

where we have assumed that the dipole moments are real, and where the field modes $\mathbf{f}_{\mu,x} = \mathbf{f}_\mu(\mathbf{r}_x)$ are evaluated at the location of QD x. In the expansion of the dipole operator we have dropped the $\mathbf{d}_{XX}$ and $\mathbf{d}_{\mathcal{F}\mathcal{F}}$ terms as they will eventually lead to dynamics that are not restricted to the one-excitation subspace. Introducing the coupling strength

$$h_{\mu x} = i\epsilon_\mu \mathbf{d}_x \cdot \mathbf{f}_{\mu,x},$$

we may use Eqs. (2.40) to set up the equations of motion for the creation and annihilation operators as

$$\begin{aligned}
\dot{a}_\mu &= -i\omega_\mu a_\mu + \frac{i}{\hbar}\sum_x h^*_{\mu x}(b_x + b_x^\dagger) \\
\dot{a}_\mu^\dagger &= i\,\omega_\mu a_\mu^\dagger - \frac{i}{\hbar}\sum_x h_{\mu x}(b_x + b_x^\dagger) \\
\dot{b}_x &= -i\omega_x b_x - \frac{i}{\hbar}\sum_\mu (h_{\mu x} a_\mu + h^*_{\mu x} a_\mu^\dagger)\, b_x^z \\
\dot{b}_x^\dagger b_x^\dagger &= i\,\omega_x + \frac{i}{\hbar}\sum_\mu (h_{\mu x} a_\mu + h^*_{\mu x} a_\mu^\dagger)\, b_x^z,
\end{aligned}$$

where we have defined the operator

$$b_x^z = [b_x^\dagger, b_x] = b_x^\dagger b_x - b_x b_x^\dagger.$$

The equations of motion may be simplified considerably due to the restriction of the dynamics to the one-excitation subspace. By expanding the operators on the states $|\mathcal{F}\rangle$, $|X\rangle = b_x^\dagger|\mathcal{F}\rangle$ and $|\mu\rangle = a_\mu^\dagger|\mathcal{F}\rangle$ we realize that within this subspace we have the identities

$$\begin{aligned}
a_\mu^\dagger b_x^z &= -a_\mu^\dagger \\
a_\mu b_x^z &= -a_\mu,
\end{aligned}$$

which effectively renders the equations of motion identical to those of the harmonic oscillator model in Ref. [48]. This is consistent with the intuitive argument that in the limit of one excitation the distinction between fermions and bosons due to symmetry becomes irrelevant.

Instead of working in the time domain as in section 2.4.3, we may follow Refs. [48, 57, 95] where the equations of motion are solved in the frequency domain. The procedure is clearly explained in Ref. [48], and we will not repeat it here. With this approach, the electric field at position $\mathbf{r}_d$ from an exciton at a different position $\mathbf{r}_x$

is given as

$$\begin{aligned}\mathbf{E}(\mathbf{r}_d,\omega) &= \frac{\mathbf{G}(\mathbf{r}_d,\mathbf{r}_x,\omega)\mathbf{S}_x(\omega)}{1-\mathbf{e}_x\mathbf{G}(\mathbf{r}_x,\mathbf{r}_x,\omega)\mathbf{e}_x U_x(\omega)} \\ &= \mathbf{G}^{(1)}(\mathbf{r}_d,\mathbf{r}_x,\omega)\mathbf{S}_x(\omega), \end{aligned} \tag{2.44}$$

where

$$\mathbf{S}_x(\omega) = \mathbf{e}_x\left(\frac{id_x\omega^2}{\epsilon_0 c^2}\right)\left[\frac{b_x(0)}{\omega-\omega_x}+\frac{b_x^\dagger(0)}{\omega+\omega_x}\right]$$

represents the source, cf. Eq. (2.12), and

$$U_x(\omega) = \left(\frac{d_x^2\omega^2}{\hbar\epsilon_0 c^2}\right)\left(\frac{2\omega_x}{\omega_x^2-\omega^2}\right)$$

is a scattering potential due to the polarizability of the exciton itself. Comparing to Eq. (2.12) we have identified the object multiplying onto the source in Eq. (2.44) as the proper Green's tensor, $\mathbf{G}^{(1)}(\mathbf{r}_d,\mathbf{r}_1,\omega)$, which includes the self interaction from the exciton in the QD.

In Ref. [48] it was shown that the electromagnetic propagator that enters the equations of motion is slightly different from the Green's tensor of classical electromagnetism. The two are different only at $\mathbf{r}=\mathbf{r}'$, however, and furthermore only the real part is different. It is well known that the real part of the Green's tensor diverges in this limit. For this reason, when calculating spontaneous emission in the dipole approximation a renormalization is usually employed [48]. This renormalization effectively renders the explicit functional form irrelevant, and in this work we therefore keep the formulation in terms of the classical Green's tensor $\mathbf{G}(\mathbf{r},\mathbf{r}')$. As noted in section 2.2.1, the Green's tensor in this work, Eq. (2.11), is different by a factor of (-1) from the Green's tensor in Ref. [48]. For this reason we have changed the source and the scattering potentials accordingly to keep the same notation.

In chapter 5.3 we use this method to investigate scattering from multiple QDs in a photonic crystal slab.

Chapter 3

Multiple scattering calculations using the Lippmann-Schwinger equation

3.1 Introduction

For a proper treatment of light propagation in micro- and nanostructured media such as PCs, the full wave nature of the electromagnetic field needs to be taken into account. In this section we describe a solution method for the Lippmann-Schwinger equation that is well suited for calculations in finite sized PCs. We believe that the method will find applications in modeling of nanophotonic structures and devices such as waveguides, junctions and filters as well as switches and single photon sources based on PCs.

In order to motivate the formulation and to illustrate differences and similarities with respect to existing methods, we first consider a small example problem.

3.1.1 An example scattering problem

We consider the simple scattering problem in Ref. [91] of a plane wave incident along the x-axis on a dielectric plate at normal incidence, as depicted in Fig. 3.1. Due to symmetry, the scattering of the two polarizations is identical in this case, and both the reflected and the transmitted wave propagate parallel to the x-axis resulting

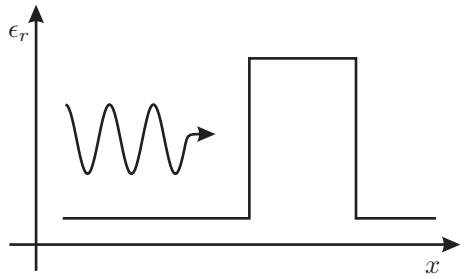

Figure 3.1: An example scattering problem. A plane wave $A\exp(ik_B x)$ is incident along the x axis onto a dielectric plate at normal incidence..

in a one-dimensional, scalar problem. This problem is among the simplest possible scattering problems and can be solved easily using most numerical methods. In particular, we may follow Ref. [91] and employ the CDA with an iterative solution scheme. Fig. 3.2 shows the CDA solution as a histogram to emphasize the pulse basis functions used in the solution. The chosen discretization corresponds to 20 basis functions per wavelength in vacuum and 10 basis functions per wavelength in the dielectric.

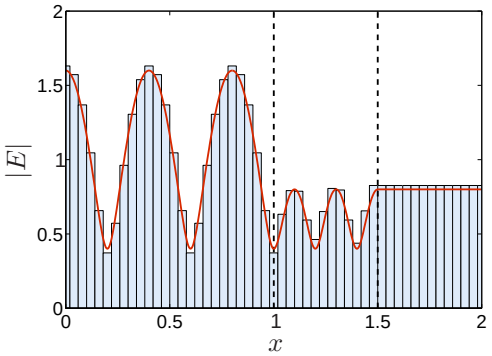

Figure 3.2: Amplitude of the solution to the scattering problem in Fig. 3.1 in the case of a dielectric barrier at $x_0 = 1$ with permittivity $\epsilon = 4$ and thickness $L = 1/2$ in vacuum. The amplitude and wavelength of the incident light is $A = 1$ and $\lambda_0 = 0.8\,\mu m$, respectively. Histogram shows the solution obtained from the CDA with a discretization of $\Delta x = 0.04\,\mu m$ and the solid curve shows the analytical solution.

The simplicity of the scattering problem, and the fact that the scatterer is homogeneous, means that the scattering problem can be solved analytically. This is

done by writing, in each section of the scattering structure, the field in terms of the solutions to the wave equation in that material. In one dimension the solutions are forward and backward traveling plane waves and so we expand the field as

$$E(x) = \begin{cases} A\exp(ik_{\mathrm{B}}x) + B\exp(-ik_{\mathrm{B}}x) & x < x_0 - L/2 \\ C\exp(ik_{\mathrm{R}}x) + D\exp(-ik_{\mathrm{R}}x) & |x - x_0| < L/2 \\ E\exp(ik_{\mathrm{B}}x) & x > x_0 + L/2 \end{cases} \tag{3.1}$$

and match the fields at the interfaces according to the boundary conditions. In this way a linear equation system is obtained that may be directly solved to yield the coefficients e_n. The solid red curve in Fig. 3.2 shows the analytical solution.

The histogram style in Fig. 3.2 illustrates how the numerical solution is never better than the sampling. In particular, for the simple pulse basis functions, the solution in cell n has the same value for all x within the cell and drops abruptly to another value in the next cell. The abrupt jumps in the numerical solution caused by the use of pulse basis functions may result in stability issues in vectorial calculations in two and three dimensions. The problem may be removed through the use of more sophisticated basis functions which would come at the expense of larger calculation times. For the scalar problems in one dimension the method is in fact convergent which is seen directly from the error analysis in Ref. [91].

The numerical solution is calculated first at positions within the dielectric plate. The solution at positions outside the plate is subsequently calculated directly from the Lippmann-Schwinger equation which is now an explicit equation. With the chosen discretization, the first part of the calculations is done using only 12 basis functions, which underscores the utility of the integral type formulation when the scattering geometries are small. It is a striking feature of the solution in Fig. 3.2 that even with the simplest possible type of basis function the solution was estimated to good accuracy using only 12 basis functions. When compared to the analytical solution that was calculated from a system of 4 equations this is quite impressive and underscores the value of having to solve for the field only within the scatterer. It is evident from Fig 3.2, however, that the discretization is somewhat coarse and the ratio of 10 basis functions per wavelength is probably as low as one would typically go in these kinds of calculations. In the present problem, the number of unit cells obviously scales linearly with the number of scatterers, the size of the scatterers and the refractive index. In higher dimensions however, the number of cells depend quadratically (in two dimensions) and cubically (in three dimensions) on the size of the scatterers, which may result in enormous memory requirements.

The increase in memory requirements in two and three dimensions, together with the stability problems for vectorial calculations when expanding on pulse basis

functions, lead us to look for an alternative basis of functions.

3.1.2 A hybrid method

In this PhD project we have developed a multiple scattering solution method to the Lippmann-Schwinger equation. The solution method is inspired by the analysis in section 3.1.1 which shows that an integral formulation is desirable because it limits the calculations to the extend of the scatterers. At the same time, the analytical result suggests that the best expansion will be in terms of solutions to the wave equation in the different regions of the calculation domain.

In our approach, the Lippmann-Schwinger equation is first expanded on a basis of solutions to the homogeneous Helmholtz equation and solved within the scattering elements. Solutions at points outside the scattering elements are subsequently calculated directly using the Lippmann-Schwinger equation. Because of the integral formulation, the method may benefit from known results for the Green's tensor in the background material while the normal mode expansion reduces the number of basis functions needed, thus enabling calculations on material systems of practical relevance. In view of the discussion in section 2.2.5 the method may be viewed as a hybrid between integral type method of moments calculations and multiple scattering multipole methods. In particular, although we use an integral equation formulation, we make use of a number of theorems which are regularly employed in multipole methods in order to simplify the evaluation of the scattering matrix elements.

Due to the hybrid formulation, a very low number of basis functions is needed. As an example; for a desired relative tolerance of 10^{-3} in PC calculations in two dimensions, one can typically work with around 10 basis functions per scatterer as shown in section 3.6. In the CDA, FDTD, FEM or other brute force numerical technique, one would typically work with at least 10 sampling points per effective wavelength in both directions. In addition, for FDTD and FEM the full calculation domain including the background will need to be discretized. For square scatterers with each side having the length $L = 0.3\lambda_0$, the demand for 10 sampling points per wavelength leads to approximately 100 points per scatterer for a refractive index of $n = 3$. This number scales quadratically (and cubically in three dimensions) with the refractive index.

3.1.3 Overview of chapter 3

In section 3.2 we formulate the method in a general form which is suited for both one, two and three dimensional problems. In section 3.1.1 the basic ideas are illustrated by a one dimensional example before proceeding to the two dimensional case in

section 3.4. We present details of the implementation in two dimensions and note that a similar approach is possible for three dimensional problems as well. Section 3.5 presents example scattering calculations in two dimensions and in section 3.6 these solutions serve as examples to discuss a practical method of evaluating the accuracy of a given calculation. Last, in section 3.7, the calculation method is extended to inhomogeneous backgrounds.

3.2 General formulation of the method

We consider scattering of monochromatic light, $\mathbf{E}(\mathbf{r},t) = \mathbf{E}(\mathbf{r})\exp(-i\omega t)$, in general systems consisting of a finite number of piecewise constant dielectric and non-magnetic perturbations to a piecewise homogeneous background, as illustrated in Fig. 3.3.

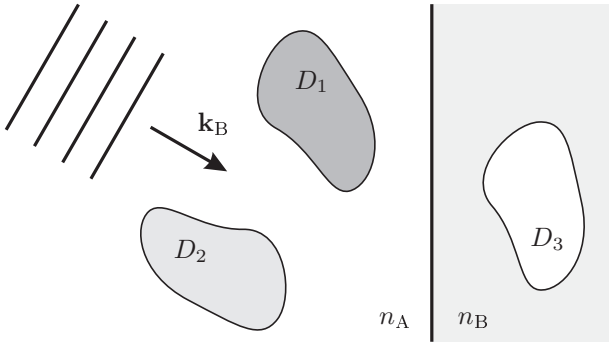

Figure 3.3: Sketch of general scattering geometry.

We will solve for the total field, $\mathbf{E}(\mathbf{r})$, inside the scattering material only, as the solution everywhere else can be subsequently obtained by use of the Lippmann-Schwinger equation. The incoming field, $\mathbf{E}^\mathrm{B}(\mathbf{r})$, is a solution to the wave equation with no scatterers and thus in general can be expanded on the solutions to the wave equation in the bulk background material, $\phi_n^\mathrm{B}(\mathbf{r})$. In a similar way, the total field inside a given scatterer may be expanded on the solutions in the bulk dielectric, $\phi_n(\mathbf{r})$. Based on these considerations we construct a basis consisting of solutions to the scalar wave equation, each with support on only one of the scattering sites,

$$\psi_n(\mathbf{r}) = K_n\phi_q(\mathbf{r})\,S_d(\mathbf{r}) \tag{3.2a}$$

$$\psi_n^\mathrm{B}(\mathbf{r}) = K_n^\mathrm{B}\phi_q^\mathrm{B}(\mathbf{r})\,S_d(\mathbf{r}), \tag{3.2b}$$

where we have defined a combined index $n = (q, d, \alpha)$, in which q is a parameter (or set of parameters) describing the solution and d denotes the particular subdomain

D_d of the scattering material we consider, e.g. which cylinder. For convenience, the field component $\alpha \in \{x, y, z\}$ is included in the index n as well. K_n and K_n^{B} are normalization constants and

$$S_d = \begin{cases} 1, & \mathbf{r} \in D_d \\ 0, & \text{otherwise} \end{cases}$$

defines the support. The solutions $\psi_n(\mathbf{r})$ have wave numbers corresponding to the index of the scattering material, $k_d = n_d k_0$, where n_d denotes the refractive index in the subdomain D_d, and $\psi^{\mathrm{B}}(\mathbf{r})$ have wave numbers corresponding to the background, $k_{\mathrm{B}} = n_{\mathrm{B}} k_0$. To ease the notation, we will write n in place of any of the indices q, d, α as this will not lead to ambiguities.

We define an inner product as

$$\langle \psi_m | \psi_n \rangle = \int \psi_m^*(\mathbf{r})\, \psi_n(\mathbf{r})\, \mathrm{d}\mathbf{r}, \tag{3.3}$$

which is in general non-zero for $m \neq n$, and the basis functions are normalized so that $\langle \psi_n | \psi_n \rangle = \langle \psi_n^B | \psi_n^{\mathrm{B}} \rangle = 1$. By expanding the electric fields as

$$\mathbf{E}(\mathbf{r}) = \sum_n e_n \psi_n(\mathbf{r}) \mathbf{e}_n$$
$$\mathbf{E}^{\mathrm{B}}(\mathbf{r}) = \sum_n e_n^{\mathrm{B}} \psi_n^{\mathrm{B}}(\mathbf{r}) \mathbf{e}_n,$$

where $\mathbf{e}_n$ is a unit vector, and projecting onto the basis formed by $\psi_m \mathbf{e}_m$ and $\psi_m^{\mathrm{B}} \mathbf{e}_m$, the Lippmann-Schwinger equation may be rewritten in matrix form as

$$\left(1 + L_{mn} \frac{\Delta\epsilon}{\epsilon_{\mathrm{B}}}\right) \sum_n \langle \psi_m | \psi_n \rangle e_n = \sum_n \langle \psi_m | \psi_n^{\mathrm{B}} \rangle e_n^{\mathrm{B}} + k_0^2 \Delta\varepsilon \sum_n G_{mn}^{\alpha\beta} e_n, \tag{3.4}$$

in which

$$G_{mn}^{\alpha\beta} = \int_V \psi_m^*(\mathbf{r}) \lim_{\delta V \to 0} \int_{V - \delta V} G_{\alpha\beta}^{\mathrm{B}}(\mathbf{r}, \mathbf{r}') \psi_n(\mathbf{r}') \mathrm{d}\mathbf{r}' \mathrm{d}\mathbf{r}, \tag{3.5}$$

with the directions α, β corresponding to the indices m, n written explicitly for clarity.

Eqs. (3.2) - (3.5) hold the complete formulation of the method. The form of the central matrix equation (3.4) is only slightly different from that of the CDA in that the left hand side is generally a matrix (although this matrix is very sparse, since basis functions belonging to different scattering domains are orthogonal by construction). The underlying strategy and the practical implementation of the

two methods, however, are very different. In the CDA, the projection onto the basis functions is straight forward resulting typically in a very large matrix equation system that is subsequently solved by iterative methods. In the present method, it is the projections onto the basis functions that are potentially time consuming but eventually leads to a relatively small system of equations.

3.2.1 Basis functions in different dimensions

The basis functions are solutions to the scalar wave equation. In one dimension the basis functions are forward and backward traveling plane waves,

$$\psi_n^{1\mathrm{D}}(x) = K_n \exp(qk_d x) S_d(x), \tag{3.6a}$$

$$\psi_n^{B,1\mathrm{D}}(x) = K_n^{\mathrm{B}} \exp(qk_{\mathrm{B}} x) S_d(x), \tag{3.6b}$$

in which $n = (q, d, \alpha)$ with $q \in \{-1, 1\}$.

In two dimensions we use the solutions to the wave equation in cylindrical coordinates (r,φ) defined with respect to the local coordinate system in the subdomain D_d,

$$\psi_n^{2\mathrm{D}}(\mathbf{r}) = K_n J_q(k_d r) e^{iq\varphi}\, S_d(\mathbf{r}) \tag{3.7a}$$

$$\psi_n^{B,2\mathrm{D}}(\mathbf{r}) = K_n^{\mathrm{B}} J_q(k_{\mathrm{B}} r) e^{iq\varphi}\, S_d(\mathbf{r}), \tag{3.7b}$$

in which J_q with $q \in \mathbb{Z}$ denotes the Bessel function of the first kind of order q.

In three dimensions we use the solutions to the wave equation in the local spherical polar coordinates (r,θ,φ) defined in the subdomain D_d,

$$\psi_n^{3\mathrm{D}}(\mathbf{r}) = K_n j_q(k_d r) Y_{lq}(\theta, \varphi)\, S_d(\mathbf{r}) \tag{3.8a}$$

$$\psi_n^{B,3\mathrm{D}}(\mathbf{r}) = K_n^{\mathrm{B}} j_q(k_{\mathrm{B}} r) Y_{lq}(\theta, \varphi)\, S_d(\mathbf{r}), \tag{3.8b}$$

in which j_q with $q \in \mathbb{Z}$ denotes the spherical bessel function of the first kind of order q and Y_{lq} are spherical harmonics [51].

3.3 One dimensional example: The example scattering problem revisited

In this section we apply the framework of section 3.2 to the example scattering problem in section 3.1.1. We solve for the electric field inside the dielectric plate where the field is expanded on only two plane waves of the form in Eq. (3.6a) with $K = 1/\sqrt{L}$ and $k_1 = k_2 = k_{\mathrm{R}}$. Eq. (3.4) is a 2x2 matrix equation,

$$\begin{bmatrix} 1 & \Delta_{12} \\ \Delta_{21} & 1 \end{bmatrix} \begin{bmatrix} e_1 \\ e_2 \end{bmatrix} = \begin{bmatrix} \Delta_{11}^{\mathrm{B}} & \Delta_{12}^{\mathrm{B}} \\ \Delta_{21}^{\mathrm{B}} & \Delta_{22}^{\mathrm{B}} \end{bmatrix} \begin{bmatrix} e_1^{\mathrm{B}} \\ e_2^{\mathrm{B}} \end{bmatrix} + k_0^2 \Delta\epsilon \begin{bmatrix} G_{11} & G_{12} \\ G_{21} & G_{22} \end{bmatrix} \begin{bmatrix} e_1 \\ e_2 \end{bmatrix},$$

where the indices 1 and 2 denote forward and backwards traveling waves, respectively, and

$$\Delta_{12} = \Delta_{21}^{*} = \frac{1}{L}\int_{x_0}^{x_0+L} e^{-2ik_{\mathrm{R}}x}\mathrm{d}x$$

is non-zero for the values of k_{R} and L in the example. Similarly, Δ_{mn}^{B} is non-zero and we have for example

$$\Delta_{12}^{\mathrm{B}} = \frac{1}{L}\int_{x_0}^{x_0+L} e^{-i(k_{\mathrm{R}}+k_{\mathrm{B}})x}\mathrm{d}x.$$

The projections G_{12}^{B} of the Green's tensor onto the basis function set is given in Eq. (3.5) and we get for example

$$G_{12} = \frac{1}{2k_{\mathrm{B}}L}\int_{x_0}^{x_0+L}\int_{x_0}^{x_0+L} e^{-ik_{\mathrm{R}}(x+y)}e^{ik_{\mathrm{B}}|x-y|}\mathrm{d}x\mathrm{d}y.$$

The integrals Δ_{12}, Δ_{mn}^{B} and G_{mn} are sufficiently simple to allow for analytical solutions. The incoming wave is a forward traveling wave and so we set $e_1^{\mathrm{B}} = 1$ and $e_2^{\mathrm{B}} = 0$ and solve the matrix equation to obtain the two unknowns e_1 and e_2. Comparing to Eq. (3.1) we must get $e_1 = \sqrt{L}\,C$ and $e_2 = \sqrt{L}\,D$. Note that in one dimension the basis function set completely spans the solution space, so there is no error due to truncation.

3.4 Implementation in two dimensions

In two dimensions the light travels in the xy-plane, $\mathbf{r} = (x, y)$, and the vector equation decouples into two independent equations for the Transverse Electric (TE) and the Transverse Magnetic (TM) polarizations. In the case of TE polarization, the electric field is oriented in the xy-plane, whereas for TM polarization the electric field is oriented along the z-axis and the scattering calculation is essentially a scalar problem.

The matrix elements need to be evaluated for basis functions within the same domain (self-terms) as well as different domains (scattering terms). The case of a homogeneous background is of special interest as one will often be able to separate the background Green's tensor into terms corresponding to a homogeneous background and a number of additional scattering terms. Therefore, we focus in this section on evaluation of the matrix elements for a homogeneous background Green's tensor and return to the additional terms due to scattering in an inhomogeneous background in section 3.7. Explicit expressions for the elements in the background Green's tensor is given in Eqs. (A.3),

A number of mathematical results exist that can dramatically speed up the calculations of the matrix elements and the implementation in general. This is discussed in sections 3.4.1-3.4.4.

3.4.1 Self-terms

The evaluation of the self-terms is complicated by the divergence in the Green's tensor for $\mathbf{r}' = \mathbf{r}$ and the fact that the integrand couples $\mathbf{r}'$ and $\mathbf{r}$, effectively resulting in a four-dimensional integral. In the following, a method for the evaluation is described in which the four-dimensional integral, Eq. (3.5), is rewritten in terms of a number of one and two dimensional integrals. This method is suitable for evaluation of general matrix elements. For special scattering geometries, however, other methods may be more efficient, and we discuss one such case by comparing to results from Mie scattering.

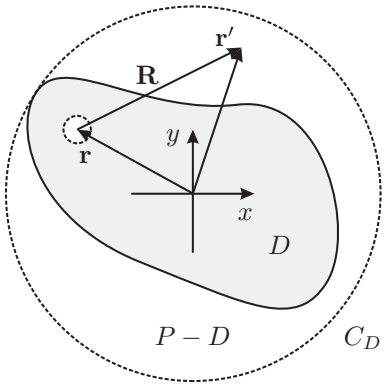

Figure 3.4: Sketch of the local coordinates used for calculation of the self-term in scattering domain D.

Figure 3.4 shows a sketch of the local coordinates used for evaluation of the integral. In order to efficiently treat the divergence, for each $\mathbf{r}$ we first integrate $\mathbf{r}'$ over the entire plane P less the principal volume centered on $\mathbf{r}$. Subsequently, the integral for $\mathbf{r}' \notin D$ is subtracted. For this integral the limit $\delta A \to 0$ is trivial since $\mathbf{r}' \neq \mathbf{r}$. The matrix element is thus rewritten as $G^{\alpha\beta}_{mn} = \mathcal{A}^{\alpha\beta}_{mn} - \mathcal{B}^{\alpha\beta}_{mn}$, in which

$$\mathcal{A}^{\alpha\beta}_{mn} = \int_D \psi^*_m(\mathbf{r}) \lim_{\delta A \to 0} \int_{P-\delta A} G^{\mathrm{B}}_{\alpha\beta}(\mathbf{r}, \mathbf{r}') \psi_n(\mathbf{r}') \mathrm{d}\mathbf{r}' \mathrm{d}\mathbf{r}$$

and

$$\mathcal{B}^{\alpha\beta}_{mn} = \int_D \psi^*_m(\mathbf{r}) \int_{P-D} G^{\mathrm{B}}_{\alpha\beta}(\mathbf{r}, \mathbf{r}') \psi_n(\mathbf{r}') \mathrm{d}\mathbf{r}' \mathrm{d}\mathbf{r}.$$

Using the Graf addition theorem (cf. appendix B.1), we can simplify the evaluation of $\mathcal{A}^{\alpha\beta}$ by expanding the function $\psi_n(\mathbf{r}')$ around the point $\mathbf{r}$, so that

$$\begin{aligned}\mathcal{A}^{\alpha\beta}_{mn} &= K_m K_n \sum_\mu \int_D J_m(k_\mathrm{R} r) J_{n+\mu}(k_\mathrm{R} r) e^{i(n+\mu-m)\varphi} \\ &\quad \times \int_{P-\delta A} G^\mathrm{B}_{\alpha\beta}(0,\mathbf{R}) J_\mu(k_\mathrm{R} R)(-1)^\mu e^{-i\mu\theta_R} \mathrm{d}\mathbf{R}\mathrm{d}\mathbf{r} \\ &= K_m K_n \sum_\mu \int_D J_m(k_\mathrm{R} r) J_{n+\mu}(k_\mathrm{R} r) e^{i(n+\mu-m)\varphi} \mathrm{d}\mathbf{r} \times I^{\alpha\beta}_\mu, \end{aligned} \tag{3.9}$$

where $k_\mathrm{R} = n_d k_0$ and we have exploited the fact that the integration over $\mathbf{R} = (R, \theta_R)$ is over the entire plane (less the principal volume) and thus does not depend on $\mathbf{r}$. The integral over $\mathbf{R}$, denoted by $I^{\alpha\beta}_\mu$ above, is nonzero only for $\mu \in \{-2, 0, 2\}$ and the evaluation can be reduced to a number of one dimensional integrals as shown in appendix C.1. In addition, we note that the simple angular dependence of the integrand in many cases allows for a reduction of the remaining integral over $\mathbf{r}$ to a sum of one dimensional integrals. In appendix C.2 we illustrate this for the case of regular polygons.

Evaluation of $\mathcal{B}^{\alpha\beta}_{mn}$ may also be substantially simplified using the Graf addition theorem to expand the Hankel function in terms of Bessel and Hankel functions defined in the local coordinate system. The expansion differs depending on the sign of $r - r'$. For $r' > r$ we write the integrand as

$$\begin{aligned} b^{\alpha\beta}_{mn}(\mathbf{r},\mathbf{r}') &= \psi^*_m(\mathbf{r}) G^\mathrm{B}_{\alpha\beta}(\mathbf{r},\mathbf{r}') \psi_n(\mathbf{r}') \\ &= K_m K_n \sum_\mu J_m(k_\mathrm{R} r) e^{-im\varphi} \mathcal{L}^{\alpha\beta} \left\{ \frac{i}{4} J_\mu(k_\mathrm{B} r) e^{-i\mu\varphi} \right\} \\ &\quad \times H_\mu(k_\mathrm{B} r') J_n(k_\mathrm{R} r') e^{i(n+\mu)\varphi'}, \end{aligned} \tag{3.10}$$

whereas, for $r' < r$ we write

$$\begin{aligned} b^{\alpha\beta}_{mn}(\mathbf{r},\mathbf{r}') &= K_m K_n \sum_\mu J_m(k_\mathrm{R} r) e^{-im\varphi} \mathcal{L}^{\alpha\beta} \left\{ \frac{i}{4} H_\mu(k_\mathrm{B} r) e^{i\mu\varphi} \right\} \\ &\quad \times J_\mu(k_\mathrm{B} r') J_n(k_\mathrm{R} r') e^{i(n-\mu)\varphi'}, \end{aligned} \tag{3.11}$$

in which

$$\mathcal{L}^{\alpha\beta} = \delta_{\alpha,\beta} + \frac{\partial_\alpha \partial_\beta}{k^2_\mathrm{B}}$$

where $\delta_{\alpha,\beta}$ is the Kronecker delta. For circular scatterers we always have $r' > r$ and the expression for $\mathcal{B}^{\alpha\beta}_{mn}$ factors into a number of one dimensional integrals. Similarly, the evaluation of $\mathcal{B}^{\alpha\beta}_{mn}$ for non-circular scatterers may be conveniently

split depending on whether $\mathbf{r}'$ is outside or inside the circumscribing circle (denoted by C_D in Fig. 3.4). In the former case, the expression factors into separate integrals for $\mathbf{r}$ and $\mathbf{r}'$, whereas in the latter case the two integrations are coupled. Again, the simple angular dependence of the integrands in many cases allows for a reduction of these integrals to a number of one and two-dimensional integrals, cf. appendix C.2.

Relation to Mie scattering

The scattering of an incoming plane wave off a single circular cylinder (or sphere) is referred to as Mie scattering. Analytical solutions to such problems can be obtained by expanding the fields inside and outside the cylinder on cylindrical wave functions and matching these in accordance with the boundary conditions [107]. Due to differences in the boundary conditions, the solutions are usually calculated for the magnetic field in the case of TE polarization and for the electric field in the case of TM polarization. It is rewarding to compare the latter with the solutions to Eq. (3.4). In the case of a single circular scatterer and TM polarization, all basis functions with $m \neq n$ are orthogonal under the inner product in Eq. (3.3). Therefore, Eq. (3.4) is diagonal and may be solved directly for the coefficients e_n:

$$e_n = \frac{\langle \psi_n | \psi_n^{\mathrm{B}} \rangle e_n^{\mathrm{B}}}{1 - k_0^2 \Delta\epsilon G_{nn}^{zz}}.$$

Given that we already know the solution e_n we may solve for the matrix elements instead:

$$G_{nn}^{zz} = \frac{e_n - \langle \psi_n | \psi_n^{\mathrm{B}} \rangle e_n^{\mathrm{B}}}{k_0^2 \Delta\epsilon e_n}, \tag{3.12}$$

which provides an analytical expression for the matrix elements, thus avoiding any numerical quadrature. Incidentally, Eqs. (3.9), (3.10) and (3.12) may be used along with the Mie scattering solution to show the identity:

$$\int_0^\infty H_0(k_{\mathrm{B}} r) J_0(k_{\mathrm{R}} r) r \mathrm{d}r = \frac{-2i}{\pi(k_{\mathrm{R}}^2 - k_{\mathrm{B}}^2)},$$

for $k_{\mathrm{R}} \neq k_{\mathrm{B}}$.

3.4.2 Scattering terms

For the calculation of scattering terms, the integration domains for $\mathbf{r}$ and $\mathbf{r}'$ are completely separated in space, and so the Green's tensor is well behaved at all points of interest. In this case we employ the Graf addition theorem twice to

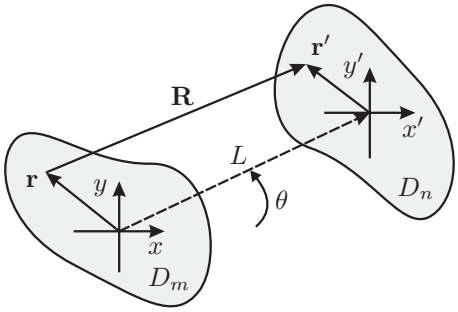

Figure 3.5: Sketch of local coordinates for $\mathbf{r}$ *and* $\mathbf{r}'$ *in two independent scatterers.*

express the Hankel function in terms of the distance between the centers of the two local coordinate systems, as illustrated in Fig. 3.5,

$$\begin{aligned} G_{mn}^{\alpha\beta} =& \frac{i}{4} \sum_{\mu,\lambda} H_{\mu+\lambda}(k_\mathrm{B} L)(-1)^\mu e^{i(\mu+\lambda)\theta} \\ & \times \int_{D_m} K_m J_m(k_m r) e^{-i\,m\,\varphi} \mathcal{L}^{\alpha\beta} \left\{ J_\lambda(k_\mathrm{B} r) e^{-i\lambda\varphi} \right\} \mathrm{d}\mathbf{r} \\ & \times \int_{D_n} K_n J_\mu(k_\mathrm{B} r') J_n(k_n r') e^{i\,(n-\mu)\,\varphi'} \mathrm{d}\mathbf{r}', \end{aligned} \tag{3.13}$$

where (L, θ) are cylindrical coordinates of $\mathcal{O}'$ with respect to $\mathcal{O}$, cf. appendix B.1. Eq. (3.13) shows that the scattering matrix calculation factors into terms that depend only on the geometries of the individual scatterers and the distance between them. Since the Hankel functions as well as the Bessel functions are well behaved at all points of interest, the integrals may be directly evaluated. Note that the procedure outlined above is compromised when $L < R_m + R_n$, where R_m and R_n are the radii of the circumscribing circles of domains D_m and D_n, respectively. This could happen in the case of close non-circular scatterers. In this case the Graf addition theorem is not valid and one can employ a strategy based on Eqs. (3.10) and (3.11) instead.

3.4.3 Background electric field

The incident background electric field, $\mathbf{E}^\mathrm{B}(\mathbf{r})$, is a solution to the wave equation without the scatterers. In the case of a bulk background, the solutions are plane waves, and the expansion in terms of cylindrical wave functions is readily obtained using the Jacobi-Anger identity, as discussed in appendix B.1. In the case of a plane wave, $A \exp(i\,\mathbf{k}\cdot\mathbf{r})$, traveling at an angle θ with respect to the x axis we

immediately get

$$e_n^{\mathrm{B}} = A\frac{i^n}{K_n^{\mathrm{B}}}e^{-i\,n\,\theta}e^{i\mathbf{k}_{\mathrm{B}}\cdot\mathbf{R}_n}\mathbf{e}_\theta\cdot\mathbf{e}_n,$$

in which $\mathbf{R}_n$ denotes the position of the scattering domain D_n and $\mathbf{e}_\theta$ is a unit vector in the direction of the electric field.

Instead of using plane waves as the background electric field we may use the columns of the 2D Green's tensor. These are related to the electric field at $\mathbf{r}$ due to a line source at $\mathbf{r}'$ [55]. Comparing to Eq. (2.17) it is evident that the solution to the Lippmann-Schwinger equation in this case exactly produces the corresponding columns of the full 2D Green's tensor for the scattering problem. By expanding the Green's tensor in terms of cylindrical wave functions,

$$\mathbf{G}(\mathbf{r},\mathbf{r}') = \sum_n \mathcal{L}\left\{H_n(k_{\mathrm{B}}L)e^{-in\theta}\right\}(-1)^n J_n(k_{\mathrm{B}}r')e^{in\varphi'},$$

we may identify the expansion coefficients corresponding to the β'th column as

$$e_n^{\mathrm{B}} = \frac{(-1)^n}{K_n^{\mathrm{B}}}\mathcal{L}^{n\beta}\left\{H_n(k_{\mathrm{B}}L)e^{-in\theta}\right\}, \tag{3.14}$$

which is valid for $L > R_n$, where R_n is the radius of the circumscribing circle of domain D_n, cf. Fig. 3.4. The (bounded) basis function set, Eqs. (3.7), is not suited to sample the Green's tensor with $\mathbf{r}$ inside any of the scatterers. In this case one may possibly extend the basis function set with the inclusion of functions of the form $\tilde{\psi}_n = K_n H_n(k_{\mathrm{R}}r)\exp(in\varphi)$.

Due to the truncation of the basis set, the divergence in the Hankel functions may result in poor sampling of the Green's tensor even for $\mathbf{r}$ outside but close to one of the scatterers. To get an estimate for the distances at which the sampling becomes a problem we may look at the series expansions for the radial parts of the terms in the Green's tensor, cf. Eqs. (A.3):

$$\begin{aligned}
\frac{i}{4}H_0(x) &= \frac{i}{4} - \frac{1}{2\pi}\left\{\ln(x/2)+\gamma\right\} + \mathcal{O}(x^2)\\
\frac{i}{4}H_1(x) &= \frac{1}{2\pi x^2} - \frac{1}{4\pi}\left\{\ln(x/2)+\gamma\right\} + \frac{1+i\pi}{8\pi} + \mathcal{O}(x^2)\\
\frac{i}{8}H_2(x) &= \frac{1}{2\pi x^2} + \frac{1}{8\pi} + \mathcal{O}(x^2).
\end{aligned} \tag{3.15}$$

For the TM polarization, the absolute value of the Hankel function has dropped to 1 at $k_{\mathrm{B}}R \approx 2\exp(-2\pi\sqrt{1-1/16}-\gamma) \approx 0.0031$. For the TE polarization, the xy term has dropped to 1 at $k_{\mathrm{B}}R \approx \sqrt{1/(2\pi-1/4)} \approx 0.41$. The same value holds for the xx and yy terms.

3.4.4 Exterior solution

The matrix equation (3.4) is solved using standard linear algebra routines to yield the solution at any point inside the scattering domains. The solution at points outside the scatterers can be subsequently obtained directly from the Lippmann-Schwinger equation which is now an explicit equation:

$$\mathbf{E}(\mathbf{r}) = \mathbf{E}^{\mathrm{B}}(\mathbf{r}) + \int_D \mathbf{G}^{\mathrm{B}}(\mathbf{r},\mathbf{r}')\, k_0^2 \Delta\varepsilon(\mathbf{r}') \sum_n e_n \psi_n(\mathbf{r}') \mathbf{e}_n \mathrm{d}\mathbf{r}'. \tag{3.16}$$

The sum in Eq. (3.16) runs over all basis functions in all scattering domains. Again, the calculation may be simplified considerably by use of the Graf addition theorem to rewrite the equation in terms of the distances from the centers of the local coordinate systems. Considering for simplicity the case of just a single scattering domain D, the equation is rewritten as

$$\begin{aligned}\mathbf{E}(\mathbf{r}) =& \mathbf{E}^{\mathrm{B}}(\mathbf{r}) + \frac{i}{4} k_0^2 \Delta\varepsilon \sum_{\mu,n} \mathcal{L}\left\{H_\mu(k_{\mathrm{B}} L) e^{i\mu\theta}\right\} (-1)^\mu \mathbf{e}_n \\ & \times e_n \int_D K_n J_n(k_{\mathrm{R}} r') J_\mu(k_{\mathrm{B}} r') e^{i\,(n-\mu)\,\varphi'} \mathrm{d}\mathbf{r}',\end{aligned} \tag{3.17}$$

where (L,θ) are now cylindrical coordinates of $\mathcal{O}'$ with respect to $\mathbf{r}$.

3.4.5 Solution of the linear equation system

In the case of practically relevant structures, Eq. (3.4) may consist of several thousand coupled linear equations. In this case a simple solution based on e.g. Gaussian elimination is impossible due to accumulation of error, and iterative methods such as the conjugate gradients method are usually employed. Iterative methods typically rely on solving the equation system

$$\mathbf{A}\mathbf{e} = \mathbf{e}^{\mathrm{B}}$$

by varying the vector $\mathbf{e}$ in order to minimize the residual

$$\xi = |\mathbf{A}\mathbf{e} - \mathbf{e}^{\mathrm{B}}|.$$

For solution of the system of equations we have used a biconjugate gradients stabilized method, which seems to be able to converge to the desired accuracy in most cases. For relatively small systems, however, we typically solve the equation system using a Moore-Penrose pseudoinverse based on singular value decomposition [108]. After solving the system with the pseudoinverse, we calculate the residual and find that the pseudoinverse returns solutions with very low relative residuals, typically $\xi \approx 10^{-10}$. For large systems, the solution step may be the far most expensive part of the calculation.

3.5 Two dimensional examples

To illustrate the method, we present in this section two example scattering problems; TE plane wave scattering from circular cylinders and calculation of the TM Green's tensor for a collection of square cylinders.

3.5.1 Plane wave scattering from circular cylinders

We consider a TE plane wave incident on a small crystallite of air cylinders in a high-index dielectric. Because of the cylindrical symmetry, the self-term matrix elements are non-zero only for $m - n \in \{-2, 0, 2\}$. Calculation of the scattering matrix elements, Eq. (3.13), is also substantially simplified because the angular integration leads to non-zero values only for terms with $\mu = n$ and $\lambda + m \in \{-2, 0, 2\}$.

Fig. 3.6 shows the absolute square of the total field as a function of position in the xy-plane. Also we show the magnitude of the E_x and the E_y components of the field along the line $y = 0$ through the centers of three of the cylinders. Clearly, the x component shows a number of discontinuous jumps, whereas the y component is continuous in accordance with the boundary conditions.

We note that the air cylinders act to partly block the light, resulting in the formation of a standing wave in the upper left part of the figure. Although an infinite triangular lattice of air holes will exhibit a photonic band gap at certain frequencies, this band gap is located at higher frequencies for the material parameters in the example [64]. Instead, we ascribe the blocking of the light as arising from the lower average refractive index of the crystallite relative to the background.

Typically we use the same number of basis functions in each scattering domain and for each polarization, so that $|q| \leq Q_{\max}$. This calculation was performed using $Q_{\max} = 10$, resulting in a matrix equation system of 294 unknowns. Using the method outlined in sections 3.4.1 and 3.4.2 and using an absolute tolerance on the numerical integrals of 10^{-6}, the average calculation time per scattering matrix element was less than 0.1 s for the self-terms and less than 0.01 s for the scattering terms on a 2.4 GHz processor. Making use of the symmetry of the crystallite we reduced the problem to the calculation of matrix elements for scattering between 19 different pairs of scatterers only. In addition, the form of Eq. (3.13) suggests that for identical scatterers the integrals across the domains D_m and D_n can be handled once only and stored for use in subsequent calculations of matrix elements for scattering between other pairs of scatterers. Using this approach, the total time for the calculation of all matrix elements was approximately 13 s. Due to the small size of the scattering problem, the solution of the linear equation system was handled in approximately a second.

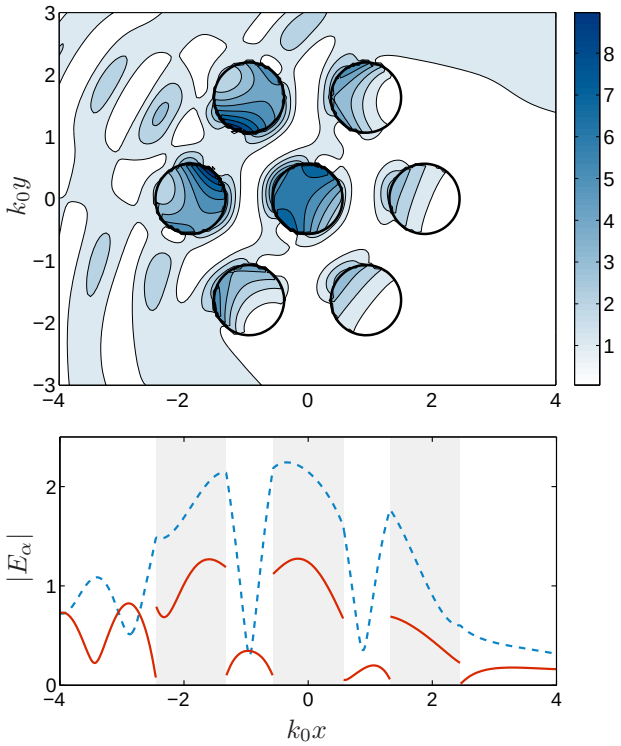

Figure 3.6: Example calculation. A TE plane wave of unit amplitude, $\mathbf{E}^B(\mathbf{r}) = \mathbf{e}\exp(i\,n_B\mathbf{k}_0\cdot\mathbf{r})$, is incident from the top left on a crystallite consisting of seven air holes ($n_d = 1$) in a high-index dielectric background ($n_B = 3.5$). Parameters are $\mathbf{k}_0 = (\sqrt{3}/2, -1/2)$ and $R_{PC} = 0.3a$ where R_{PC} is the radius of the cylindrical holes and $a = 0.3\lambda_0$ is the distance in between. Top: Absolute square, $|\mathbf{E}(\mathbf{r})|^2$, of the resulting field as a function of position in the xy-plane. Bottom: Absolute value of the components $E_x(x)$ (red solid line) and $E_y(x)$ (blue dashed line) along the line $y = 0$.

3.5.2 Green's tensor for a collection of square cylinders

In this section we apply the framework of section 3.4 to non-circular scatterers. In addition, we use the Green's tensor for the homogeneous material as the background field, so that we may interpret the solution as the Green's tensor for the entire structure including the scatterers, as discussed in section 3.4.3. We consider a geometry consisting of four square dielectric rods in air. The calculation of the matrix elements for the square scatterers is carried out in appendix C.2. Due to

the four-fold rotational symmetry, the self-term matrix elements are non-zero only for $m - n = 4p$ with $p \in \mathbb{Z}$.

In Fig. 3.7 we show the real and imaginary parts of the TM Green's tensor $G_{zz}(\mathbf{r}, \mathbf{r}')$ as a function of $\mathbf{r}$ for constant $\mathbf{r}'$ indicated in the figure. The calculation was performed using $Q_{\max} = 10$, resulting in only 84 unknowns. We used an absolute tolerance on the numerical integrals of 10^{-6}, and the average time per scattering matrix element was 0.7 s for the self-terms and 0.04 s for the scattering terms. Based on symmetry, the problem was reduced to the calculation of scattering matrix elements between 9 pairs of scatterers resulting in a total time for the matrix element calculations of approximately 200 s and a solution time of less than a second.

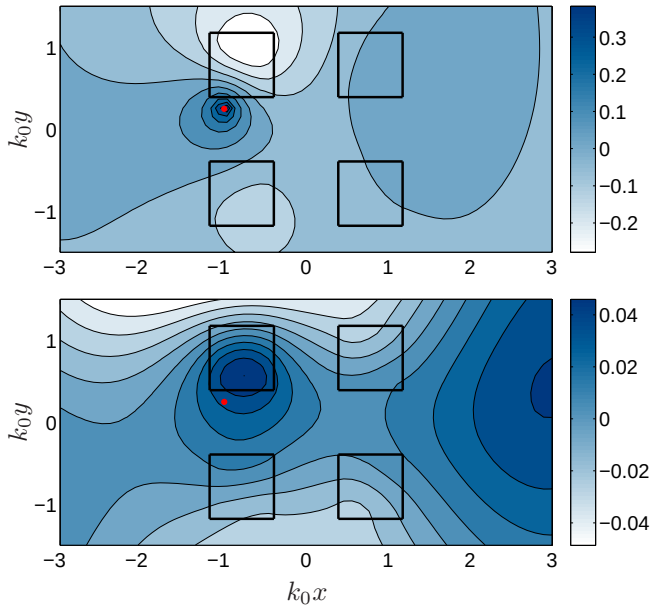

Figure 3.7: Real (top) and imaginary (bottom) part of the total TM Green's tensor $G_{zz}(\mathbf{r}, \mathbf{r}')$ as a function of $\mathbf{r}$ with $k_0\mathbf{r}' = (-1, 1/4)$ (as indicated by the red dot) in a structure consisting of four dielectric rods ($n_d = 3.5$) of square cross section in air. Parameters are $a = 2L$ where a is the distance between the rods and $L = \lambda_0/4$ is the side length.

The real part of the Green's tensor diverges in the limit $\mathbf{r} \to \mathbf{r}'$ which is the case also for the results in Fig. 3.7. Indeed it must be the case, since the results are obtained as the sum of the background field and the scattered field, as discussed in section 3.4.4. The scattered field is well behaved at all points, however, so

the divergence in the Green's tensor stems from the divergence in the background Green's tensor only. This divergence is logarithmic in the case of TM polarization as discussed in section 3.4.3 which is the reason why it does not show up at the chosen discretization. The imaginary part of the Green's tensor is continuous at all points. In the limit $\mathbf{r} = \mathbf{r}'$ it is proportional to the LDOS, cf. Eq. (2.14).

3.6 Error analysis

The numerical error in the calculations stems primarily from evaluation of the matrix elements and the truncation of the basis set. After solving the linear equation system, Eq. (3.4), the accuracy of a given solution may be estimated by substitution back into the Lippmann-Schwinger equation. To this end we define the local error as

$$\mathcal{E}_{\mathrm{L}}(\mathbf{r}) = |\mathbf{E}^{\mathrm{B}}(\mathbf{r}) - \mathbf{E}_{\mathrm{num}}(\mathbf{r}) + \int \mathbf{G}^{\mathrm{B}}(\mathbf{r},\mathbf{r}')\, k_0^2 \Delta\varepsilon(\mathbf{r}')\, \mathbf{E}_{\mathrm{num}}(\mathbf{r}')\mathrm{d}\mathbf{r}'|, \tag{3.18}$$

and we note that since $\mathbf{E}^{\mathrm{B}}(\mathbf{r})$ and $\mathbf{G}^{\mathrm{B}}(\mathbf{r},\mathbf{r}')$ are known analytically Eq. (3.18) can be used as a measure for the accuracy of a given calculation even if the analytical solution is not known. Based on the local error, we define the global relative error as

$$\mathcal{E}_{\mathrm{G}} = \frac{\int \mathcal{E}_{\mathrm{L}}(\mathbf{r})\mathrm{d}\mathbf{r}}{\int |\mathbf{E}^{\mathrm{B}}(\mathbf{r})|\mathrm{d}\mathbf{r}},$$

where the integrals are taken over the area of the scattering sites only. Fig. 3.8 shows the global error of the solutions to the problems in Figs. 3.6 and 3.7 as a function of the number of basis functions used in the expansions and dependent on the error in the matrix elements. The error analysis was performed by first calculating the matrix elements to high precision using an absolute error tolerance on the numerical integrals of 10^{-6}. Subsequently, for each value of $Q_{\max}$ the corresponding linear equation system, Eq. (3.4), was constructed, and a random complex number of fixed modulus, δG_{mn}, was added to each element in the matrix of modulus larger than δG_{mn} before solving the equation system.

The analysis shows an exponential like decrease in the global error as a function of the number of basis functions, underscoring the massive reduction in basis functions due to the expansion in normal modes when compared to conventional discretization methods. This is the case for the cylindrical holes in Fig. 3.6 as well as for the square rods in Fig. 3.7. The convergence is faster in the case of the cylindrical holes which is partly because the basis functions have the same symmetry as the scatterers and partly because the plane wave field is easier to approximate than the (divergent) Hankel function, as noted in section 3.4.3. From Fig. 3.8 we argue

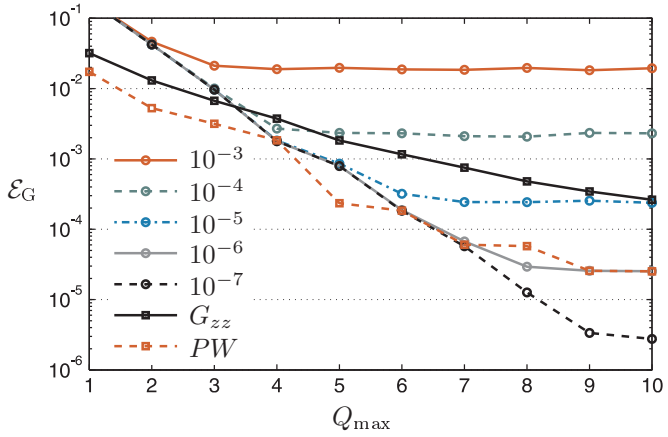

Figure 3.8: Global error as a function of the number of basis functions used in the expansion of the electric fields (controlled by Q_{max}). Circular markers correspond to the problem in Fig. 3.6 with different curves corresponding to different fixed errors on the relevant matrix elements as indicated. Square markers correspond to the problem in Fig. 3.7 calculated for the Green's tensor (G_{zz}) and plane waves (PW) as the background field.

that the artificial error on the matrix elements acts to limit the minimum achievable global error, and the analysis thus confirms that the global error is controlled by the number of basis functions as well as the accuracy of the numerical quadrature. We note that the measure in Eq. (3.18) may be viewed as a test of self-consistency of the method which is of principal importance for any solution to Eq. (2.16). From Fig. 3.8 it is evident that the measure is also of practical importance since, for a given tolerance on the numerical integrals, it can be used to estimate the number of basis functions needed to reach the minimum global error.

3.7 Inhomogeneous backgrounds

As an example of the utility of the method, we present in this section results for the investigation of light propagation near the edge of a finite sized two dimensional PC. We consider a PC made from 80 circular rods of refractive index $n_d = 3.4$ in a lower-index background ($n_{\mathrm{B}} = 1.5$). The cylinders are placed in a square lattice, and a short waveguide is created by the omission of 4 rods along the (11) direction of the crystal. The waveguide along with the crystal is terminated by an interface to air. We focus on TM polarized light and calculate the Green's tensor of the system $G_{zz}(\mathbf{r}, \mathbf{r}')$. Although the integral expressions become larger, a similar procedure as

the one outlined below may be used for the calculation of TE polarized light as well as for multiple interfaces. We start by extending the formalism of the previous sections to the case of a non-homogeneous background Green's tensor in section 3.7.1 and go on to show example calculations of light emission from a finite sized PC in section 3.7.2.

3.7.1 Additional scattering near interface

For the scattering calculations near a dielectric interface we use the Green's tensor for the dielectric half-space as the background Green's tensor in Eq. (2.16). The 2D Green's tensor for general stratified media is given in Ref. [54] in terms of an integral in **k**-space. Below, we discuss the calculation of the elements G^{zz}_{mn} in the special case of a single dielectric interface. We consider TM polarized light incident on an interface at $y = 0$ between two media with refractive indices n_A and n_B, respectively. We will deal only with scatterers in the lower layer (layer B) and so, following Ref. [54], the 2D Green's tensor is given as

$$\begin{aligned} G^\mathrm{B}_{zz}(\mathbf{r},\mathbf{r}') = &-\frac{\hat{\mathbf{y}}\hat{\mathbf{y}}}{k_2^2}\delta(\mathbf{R}) \\ &+ \frac{i}{4\pi}\int_{-\infty}^{\infty}\frac{1}{k_{\mathrm{B},y}} e^{i\,k_x(x-x')} e^{i\,k_{\mathrm{B},y}|y-y'|}\mathrm{d}k_x \\ &+ \frac{i}{4\pi}\int_{-\infty}^{\infty}\frac{\mathcal{F}^\mathrm{S}_\mathrm{BA}}{k_{\mathrm{B},y}} e^{i\,k_x(x-x')} e^{-i\,k_{\mathrm{B},y}(y+y')}\mathrm{d}k_x, \end{aligned} \tag{3.19}$$

where $k_{l,y} = \sqrt{k_l^2 - k_x^2}$ with $k_l = n_l k_0, l \in \{\mathrm{A},\mathrm{B}\}$ and

$$\mathcal{F}^\mathrm{S}_\mathrm{BA} = \frac{k_{\mathrm{B},y} - k_{\mathrm{A},y}}{k_{\mathrm{B},y} + k_{\mathrm{A},y}} = \frac{\sqrt{k_\mathrm{B}^2 - k_x^2} - \sqrt{k_\mathrm{A}^2 - k_x^2}}{\sqrt{k_\mathrm{B}^2 - k_x^2} + \sqrt{k_\mathrm{A}^2 - k_x^2}}$$

is the Fresnel reflection coefficient.

In Eq. (3.19), the first two terms correspond to the Green's tensor of the homogeneous material, whereas the last term gives the reflection off the interface. This means that the evaluation of the matrix element G^{zz}_{mn} naturally splits into a direct homogeneous material part and an indirect interface scattering part. The former is exactly what was handled in sections 3.4.1 and 3.4.2, so we concentrate in this section only on the scattering contribution G^S_{mn}:

$$\begin{aligned} G^\mathrm{S}_{mn} = \frac{i}{4\pi}\int_{-\infty}^{\infty}\frac{\mathcal{F}^\mathrm{S}_\mathrm{BA}(k_x)}{k_{\mathrm{B},y}(k_x)}\int_{D_m}\int_{D_n}\psi^*_m(\mathbf{r}) e^{i\,k_x(x-x')} \\ \times e^{-i\,k_{\mathrm{B},y}(k_x)(y+y')}\psi_n(\mathbf{r}')\mathrm{d}\mathbf{r}'\mathrm{d}\mathbf{r}\mathrm{d}k_x. \end{aligned} \tag{3.20}$$

In order to carry out the integration, we first write $(x, y) = (X, Y)+(r\cos\varphi, r\sin\varphi)$ and $(x', y') = (X', Y') + (r'\cos\varphi', r'\sin\varphi')$, where (X, Y) and (X', Y') denote the absolute coordinates of the centers of the local coordinate systems. We then recast the expression in terms of local coordinates as

$$\begin{aligned} G^{\mathrm{S}}_{mn} = \frac{i}{4\pi}\int_{-\infty}^{\infty} \frac{\mathcal{F}^{\mathrm{S}}_{\mathrm{BA}}(k_x)}{k_{\mathrm{B},y}(k_x)} e^{i(k_x(X-X')-k_{\mathrm{B},y}(k_x)(Y+Y'))} \\ \times \int_{D_m} K_m J_m(k_m r) e^{-i\,m\,\varphi} e^{i\,k_{\mathrm{B}}\,r\,\cos(\varphi-\theta(k_x))}\mathrm{d}\mathbf{r} \\ \times \int_{D_n} K_n J_n(k_n r') e^{i\,n\,\varphi'} e^{i\,k_{\mathrm{B}}\,r'\,\cos(\varphi'-\theta'(k_x))}\mathrm{d}\mathbf{r}'\mathrm{d}k_x, \end{aligned} \tag{3.21}$$

where we have rewritten the inner products of the wave vectors and the position vectors in the two domains in terms of the angles between them. This angle becomes imaginary whenever $k_x^2 > k_{\mathrm{B}}^2$. As in the case of the homogeneous background, we are able to simplify the expression further by factoring out the integrals over the domains D_m and D_n. To this end we use the Jacobi Anger identity, cf. appendix B.1, to rewrite the matrix elements as

$$\begin{aligned} G^{\mathrm{S}}_{mn} = \frac{i}{4\pi}\sum_{\lambda,\gamma} i^{\lambda+\gamma} \\ \times \int_{-\infty}^{\infty} \frac{\mathcal{F}^{\mathrm{S}}_{\mathrm{BA}}(k_x)}{k_{\mathrm{B},y}(k_x)} e^{i(k_x(X-X')-k_{\mathrm{B},y}(k_x)(Y+Y'))} e^{-i(\lambda\theta(k_x)+\gamma\theta'(k_x))}\mathrm{d}k_x \\ \times \int_{D_m} K_m J_m(k_m r) J_\lambda(k_{\mathrm{B}} r) e^{i\,(\lambda-m)\,\varphi}\mathrm{d}\mathbf{r} \\ \times \int_{D_n} K_n J_n(k_n r') J_\lambda(k_{\mathrm{B}} r') e^{i\,(\gamma+n)\,\varphi'}\mathrm{d}\mathbf{r}'. \end{aligned} \tag{3.22}$$

Due to the circular symmetry, the angular integrations over the domains D_m and D_n lead to non-zero values only for $\lambda = m$ and $\gamma = n$. In these cases the radial integrals have well known analytical values (see appendix B.3), leaving only a final integration over k_x.

3.7.2 Light emission in finite sized photonic crystal waveguide

We may now combine the scattering calculations for a homogeneous background with the procedure in section 3.7.1 in order to include the additional scattering from an interface. In Fig. 3.9 we show a contour plot of the absolute value of the Green's tensor $|G_{zz}(\mathbf{r}, \mathbf{r}')|$ along with real and imaginary parts at positions along the x-axis. Results are shown for $k_0\mathbf{r}' = (0, -7.58)$ in the center of the waveguide at the location of one of the missing rods. In an infinite waveguide this would be the location of the field antinode of the waveguide mode.

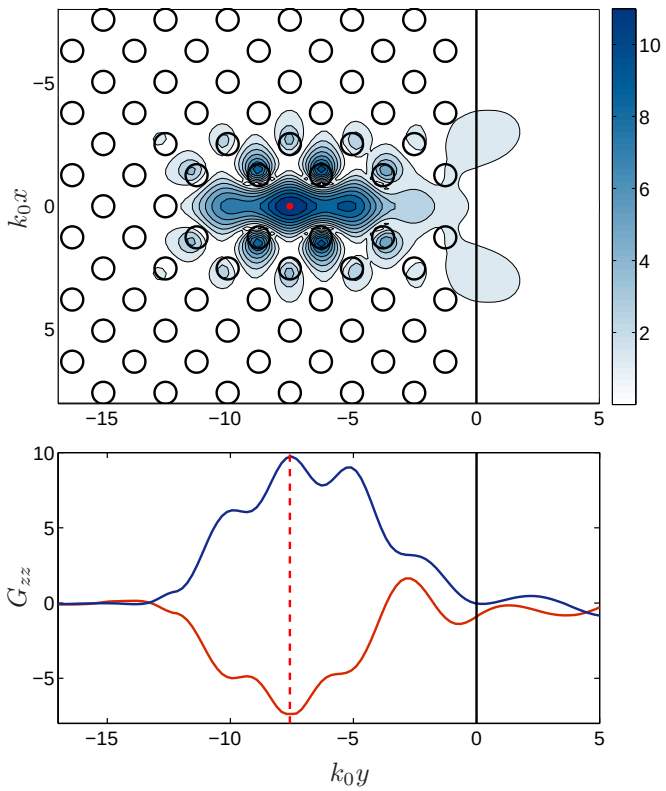

Figure 3.9: Top: Absolute value, $|G_{zz}(\mathbf{r},\mathbf{r}')|$, of the TM Green's tensor for a finite sized PC waveguide consisting of 80 rods of refractive index $n_d = 3.4$ in a background with an interface between a low-index dielectric ($n_B = 1.5$) and air ($n_A = 1$). The results are calculated as a function of $\mathbf{r}$ with $k_0\mathbf{r}' = (0, -7.58)$ (indicated by the red dot and vertical dashed line). Bottom: Real (red) and imaginary (blue) parts of $G_{zz}(y,\mathbf{r}')$ along the line $x = 0$. Parameters are $R_{PC} = 0.25a$ where R_{PC} is the radius of the cylindrical holes and $a = 0.28\lambda_0$ is the distance in between.

The periodic Bloch-mode character of the waveguide mode is evident also in the case of this finite waveguide, and the structure acts as a resonator greatly increasing the absolute value of the Green's tensor for positions $\mathbf{r}$ inside the waveguide as compared to the bulk medium. For $\mathbf{r} \to \mathbf{r}'$ the real part of $G_{zz}(\mathbf{r},\mathbf{r}')$ diverges. This is the case also in Fig. 3.9, but the divergence is too weak to show up at the chosen discretization. Although the finite waveguide acts as a resonator, light can propagate out of the end facet. Fig. 3.10 shows $|G_{zz}(\mathbf{r},\mathbf{r}')|$ at positions outside the structure. As noted in section 3.4.3, the Green's tensor is related to the electric

field at point $\mathbf{r}$ due to a line source at point $\mathbf{r}'$. Therefore, we may interpret the figure as the emission pattern from the source inside the waveguide. Due to the resonator effect of the waveguide structure, the emission pattern does not show up on the scale of the contour plot in Fig. 3.9.

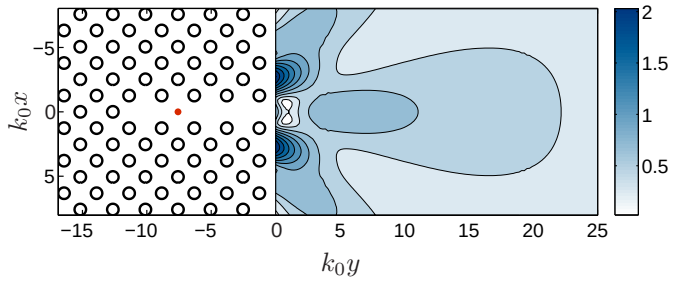

Figure 3.10: Contour plot of emission pattern, $|G_{zz}(\mathbf{r}, \mathbf{r}')|$, of the system in Fig. 3.9 but for positions outside the PC.

3.8 Conclusion

We have described a procedure for solving the Lippmann-Schwinger equation for electromagnetic scattering in which the field along with the electric field Green's tensor is expanded inside each scatterer on a basis of solutions to the scalar Helmholtz equation. We have presented the method in a general form that is suited for both one, two and three dimensional problems, and we have shown a simple example of implementation in one dimension and provided a thorough discussion of the implementation in two dimensions. In this case, the projection of the electric field and the Green's tensor onto the basis set is facilitated by the use of a number of addition theorems to simplify the integral expressions.

The chosen basis set ensures that all basis functions have the correct wave number. This, combined with the need for solving the system inside the scattering elements only, results in a relatively small linear equation system as compared with other methods. Consequently, the method is fast and capable of handling large material systems such as PCs. In two dimensions, the use of a local cylindrical wavefunction basis avoids the introduction of fictitious charges which may lead to instabilities for large refractive index contrasts in the case of TE polarization [84], and the integration scheme is free of staircasing errors along the boundaries. Due to the formulation in terms of the Green's tensor for the background medium there is no need for a calculation domain, and the radiation condition is automatically satisfied as are the boundary conditions (limited only by the numerical precision

chosen). The accuracy of the method is thus limited only by the number of basis functions and the tolerances on the numerical integrals employed for the evaluation of the scattering matrix elements. We have introduced a measure of accuracy based on self-consistency that is of principal as well as practical importance. Once the matrix equation has been set up, it holds all information necessary to carry out scattering calculations on the geometry at the chosen frequency. It can thus be stored and used for different choices of incoming fields as well as for the calculation of the Green's tensor between different points $\mathbf{r}$ and $\mathbf{r}'$.

We have illustrated the method by two example problems, and we have shown an application of the method where we have calculated the G_{zz} component of the Green's tensor for a finite sized PC waveguide. Similar calculations will find application in the development of nanophotonic devices such as in design of junctions or cavities in PCs or investigation of emission patterns from single photon sources. Using a similar procedure, the method may be extended to three dimensional scattering geometries, and although we have focused on applications in micro- and nanophotonic structures we believe the method may be of use in other areas of electromagnetic scattering calculations as well.

Chapter 4

Fractional decay of quantum dots in photonic crystals

4.1 Introduction

Section 1.2.4 described how variations in the LDOS may lead to qualitatively different decay dynamics. Especially how a heavily modified LDOS, such as observed in some PCs, may result in the marvelous quantum optical phenomenon that we called fractional decay. Fractional decay has been investigated theoretically by a number of authors [19, 20, 109] and continues to be of interest [110]. In this chapter we consider the phenomenon in the context of quantum dots in photonic crystals.

By a pure fractional decay we understand a decay in which the probability amplitude for the excited state tends to a finite non-zero value at long times, $|c_x(t)|^2 \to k$, $(0 < k < 1)$, for $t \to \infty$. For these solutions it is natural to define a degree of fractional decay as $d_f = 1 - k$. If we include the effects of absorptive losses the decay curves inevitably tend to zero at long times, but nevertheless we may still meaningfully assign a degree of fractional decay to these solutions also.

For the calculations we employ the general approach of Vats *et. al* [62] and use the minimal coupling Hamiltonian in the dipole approximation, as discussed in section 2.4.3. Contrary to the general treatment in Ref. [62], we focus on the possible realization of fractional decay using specific and realistic structures. In particular, the investigations are based on the actual LDOS of a three dimensional PC obtained from plane wave calculations. Due to the resonant nature of the light-matter coupling, the qualitative nature of the dynamics are governed by the LDOS in a narrow frequency interval around $\omega = \omega_x$. At first sight this is encouraging for the theoretical analysis since we can focus on a narrow frequency range of the

LDOS. However, the relevant frequency range turns out to be several orders of magnitude smaller than typical resolutions in LDOS calculations. To overcome this problem we use plane wave calculations to set up an analytical approximation to the band edge LDOS.

The LDOS model is extended to include effects of absorptive losses. Absorption is shown to be a limiting factor and we present quantitative results showing the degree of fractional decay achievable for available QDs and practically relevant material loss.

4.1.1 Overview of chapter 4

Section 4.2 starts out with a general discussion of the method and reviews some of the results from section 1.2.4 as illustrative examples. Motivated by the examples, it is discussed how a measure for the degree of fractional decay may be obtained from analysis of the decay dynamics in the frequency domain. In section 4.3 we employ the measure for analysis of fractional decay in the so-called anisotropic band gap model.

In section 4.4 we carry out detailed investigations of the LDOS close to the band edge of a Si inverse opal based on an analytical approximation to numerical plane wave calculations. In this way we are able to assess the validity of the anisotropic band gap model. Using perturbation theory we extend the model to include effects of absorptive loss in the LDOS. Finally, in section 4.5 we investigate the degree of fractional decay that can be obtained in Si inverse opals with absorptive losses.

4.2 Calculation of decay curves

Following Ref. [62] the equations of motion may be solved in the frequency domain using the initial condition $c_x(t=0)=1$. In this case the analysis of the decay is based on the spectrum for the expansion coefficient $c_x(\omega)$,

$$c_x(\omega) = \frac{1}{\alpha\, G(\omega) - i\,(\omega - \omega_x)}, \tag{4.1}$$

where α is a measure of the light-matter coupling strength, cf. section 2.4.3, and ω_x is the exciton frequency. The function $G(\omega)$ is given for frequencies above the integration path in the complex plane as

$$G(\omega) \;=\; i\,\omega \int_0^{\omega_C} \frac{\rho_x(z)}{z^2(\omega - z)}\mathrm{d}z, \tag{4.2}$$

where $\rho_x(\omega)$ denotes the LDOS, and we have introduced an upper cutoff to make the integral finite. Eq. (4.2) may be used along with the spectrum, Eq. (4.1),

to investigate the degree of fractional decay. To motivate the analysis we consider first the case of an integration path along the real axis in which case we obtain the important limiting form

$$G(\omega) = G_{\mathrm{R}}(\omega) + iG_{\mathrm{I}}(\omega), \tag{4.3}$$

where the two functions $G_{\mathrm{R}}(\omega)$ and $G_{\mathrm{I}}(\omega)$ are defined as

$$G_{\mathrm{R}}(\omega) = \pi\frac{\rho(\omega)}{\omega} \tag{4.4}$$

$$G_{\mathrm{I}}(\omega) = \omega \mathrm{P}\int_0^{\omega_C} \frac{\rho_x(z)}{z^2(\omega - z)}\mathrm{d}z, \tag{4.5}$$

with P denoting the Cauchy principal value of the integral.

4.2.1 Illustrative examples

With $\rho_x(\omega) = 0$ we have $G(\omega) = 0$ and the spectrum has a simple pole at $\omega_0 = \omega_x$ which, upon transforming back to the time domain, results in the constant function $|c_x(t)|^2 = 1$. This has the direct physical interpretation that if the only decay mechanism is through spontaneous emission, and if no optical modes are available, then no decay can occur.

Exponential decay

For $\rho(\omega) > 0$ the effect of $G(\omega)$ is to shift the pole away from the real axis and into the fourth quadrant of the complex ω plane. For weak light-matter interaction, the spectrum will have a single pole, ω_0, leading to an exponential decay. If the LDOS varies sufficiently slowly we can estimate the position of the pole from Eq. (4.3) by evaluating $G(\omega)$ at $\omega = \omega_x$. This is the pole approximation, and in this case we find

$$\omega_0 \approx \omega_x + \alpha G_{\mathrm{I}}(\omega_x) - i\alpha G_{\mathrm{R}}(\omega_x), \tag{4.6}$$

so we may write the spectrum as

$$c_x(\omega) = \frac{i}{\omega - \omega_0}.$$

The time-domain dynamics may now be readily found through the inverse Fourier transform,

$$c_x(t) = \frac{1}{2\pi}\int_{-\infty}^{\infty} \frac{i}{\omega - \omega_0} e^{-i\omega t}\mathrm{d}\omega = e^{-i\omega_0 t},\ t > 0, \tag{4.7}$$

where we have closed the integration path in the lower half of the complex plane. The physically observable decay curves are given as $|c_x(t)|^2$ denoting the probability

that an excitation exists in the QD at time t. From the above analysis we find that for a slowly varying LDOS the decay rate is given as

$$\Gamma = 2\pi\alpha\frac{\rho_x(\omega_x)}{\omega_x}.$$

Pure fractional decay

For the probability amplitude to go to a finite constant value there will need to be at least one pole on the real axis. From Eq. (4.7) we realize that any pole with a non-zero imaginary part will lead to a decaying exponential function and so will not meet the criterion we have set up for a pure fractional decay. From Eq. (4.4) it is evident that if the pole is real then $\rho(\omega_0) = 0$. This means, that a necessary condition for pure fractional decay to occur is for the LDOS to be zero at least for one frequency. The real part of the pole is determined by ω_x and the function $G_{\mathrm{R}}(\omega)$, which will move the pole in the direction of the negative real axis (the Lamb shift). In the general case, and in particular for fractional decay calculations, the pole approximation is not valid, so Eq. (4.6) cannot be used. From the spectrum, Eq. (4.1), we see that $\rho_x(\omega_0) = 0$ at whatever frequency solves the equation

$$\omega_0 - \omega_x - \alpha G_{\mathrm{R}}(\omega_0) = 0.$$

4.2.2 A measure for the degree of fractional decay

The analysis in section 4.2.1 illustrates how a pole in the spectrum results in a decreasing exponential term. The decay rate is proportional to the imaginary part of the pole, and in the limiting case of pure fractional decay this may be zero. We write a general pole term as

$$\frac{a_{-1}}{\omega - \omega_0},$$

and we note that the absolute square of the residue, $|a_{-1}|^2$, represents the relative magnitude of the pole term and is equal to the value of the exponential part at $t = 0$. In the case of slow variations in the LDOS we have $|a_{-1}|^2 = 1$ and the spectrum consists only of a single pole term. This is characteristic of the weak coupling Purcell regime. For structures in which the LDOS show large variations around the emitter frequency the single pole approximation is no longer valid. In this case we can usually still find a pole, but there may also be other contributions to the spectrum. Therefore, in general the spectrum may be written as a pole term and a rest term as

$$c_x(\omega) = \frac{a_{-1}}{\omega - \omega_0} + c'(\omega).$$

If $|a_{-1}|^2 < 1$ the rest term must be non-zero in order to meet the initial condition $|c_x(t=0)|^2 = 1$. Consequently, this signifies a deviation from the Purcell regime and we define

$$d_{\mathrm{f}} = 1 - |a_{-1}|^2$$

as a measure of the degree of fractional decay. This measure is reasonable when describing fractional decay curves since it measures the deviation from the exponential decay of the Purcell regime. For the pure fractional decay $|a_{-1}|^2$ gives exactly the limiting value of the decay curves for long times. The measure is convenient from a mathematical point of view also, since it can be calculated simply from the derivative of the denominator in Eq. (4.1) at the location of the pole. The denominator, $\Phi(\omega)$, is expanded in a Taylor series around the pole as

$$\Phi(\omega) = \alpha G(\omega) - i(\omega - \omega_x) = \Phi'(\omega_0)(\omega - \omega_0) + \mathcal{O}\left((\omega - \omega_0)^2\right),$$

where we have used the notation

$$f'(\omega_0) = \frac{\mathrm{d}}{\mathrm{d}\omega} f(\omega)\Big|_{\omega=\omega_0}.$$

From the Taylor series it follows that we can rewrite the spectrum in the form of a pole term and a non-zero rest term as

$$\begin{aligned} c_x(\omega) &= \frac{1/\Phi'(\omega_0)}{\omega - \omega_0} + \frac{1}{\Phi'(\omega_0)(\omega - \omega_0) + \mathcal{O}\left((\omega - \omega_0)^2\right)} - \frac{1}{\Phi'(\omega_0)(\omega - \omega_0)} \\ &= \frac{1/\Phi'(\omega_0)}{\omega - \omega_0} + \frac{\mathcal{O}\left((\omega - \omega_0)^2\right)}{\left(\Phi'(\omega_0)(\omega - \omega_0)\right)^2 + \mathcal{O}\left((\omega - \omega_0)^3\right)}. \end{aligned}$$

In practice, we first calculate the pole term and then simply subtract this from the spectrum to get the rest term.

4.2.3 Estimates of the residue

In the Purcell regime, the term $\alpha G(\omega)$ is small compared to the exciton frequency ω_x. Indeed, from the analysis of exponential decay in section 4.2.1 it follows that the decay rate is simply $\Gamma = 2\,\alpha\,G_{\mathrm{R}}$. With $\omega_x \approx 10^{15}\,\mathrm{s}^{-1}$ and typical values for Γ in the range of ns^{-1} (as seen in Fig 1.4) we have $\alpha G_{\mathrm{R}}(\omega_x)/\omega_x \approx 10^{-6}$. Therefore, in order to estimate the residue of the pole term we may use, as a first approximation, the derivative of $\Phi(\omega_x)$. With this, the derivative of the denominator is given as

$$\Phi'(\omega_x) = \alpha G'_{\mathrm{R}}(\omega_x) + i(\alpha G'_{\mathrm{I}}(\omega_x - 1)),$$

and the absolute square of the residue readily follows as

$$|a_{-1}|^2 = \left((\alpha G'_{\mathrm{R}}(\omega_x))^2 + (\alpha G'_{\mathrm{I}}(\omega_x) - 1)^2\right)^{-1}. \tag{4.8}$$

We are mainly interested in material systems for which the decay dynamics deviate from the Purcell regime. Due to the formulation in terms of an integral, the function G_{I} is somewhat complicated to work with. The function G_{R}, on the other hand, is a lot simpler and is basically the scaled LDOS. In addition, both terms in Eq. (4.8) are positive, so provided that $G'_{\mathrm{R}}(\omega_x) = G'_{\mathrm{R}}(\omega_0)$ we may state

$$\alpha G'_{\mathrm{R}}(\omega_x) > 1 \tag{4.9}$$

as a sufficient (but not necessary) condition that the dynamics deviate from the Purcell regime. This represents a mathematical formulation of the argument used in section 2.4.3 to justify the Wigner-Weisskopf approximation; namely that the LDOS should vary little over the spectral linewidth of the emitter.

At this point it is illustrative to introduce a scaled (and dimensionless) LDOS through the substitution

$$\rho_x(\omega) = \frac{\omega_x^2}{3\pi^2 c^3}\tilde{\rho}_x(\tilde{\omega}) = \rho_0(\omega_x)\tilde{\rho}_x(\tilde{\omega}),$$

where $\rho_0(\omega)$ denotes the DOS of free space, and where we have introduced a scaled (and dimensionless) frequency through the substitution

$$\omega = \omega_x\tilde{\omega}.$$

In terms of the scaled quantities we may write the condition in Eq. (4.9) as

$$\beta\pi\frac{\mathrm{d}}{\mathrm{d}\tilde{\omega}}\left(\frac{\tilde{\rho}_x(\tilde{\omega})}{\tilde{\omega}}\right) = \beta\pi\left(\frac{\tilde{\rho}'_x(\tilde{\omega})}{\tilde{\omega}} - \frac{\tilde{\rho}_x(\tilde{\omega})}{\tilde{\omega}^2}\right) > 1, \tag{4.10}$$

where the dimensionless coupling strength beta is defined as

$$\beta = \frac{p^2 q^2}{6\hbar m^2 \pi^2 \epsilon_0 c^3},$$

and is related directly to the decay rate in free space as

$$\Gamma_0 = 2\pi\omega_x\beta.$$

Experimental values for β range from $\beta \approx 10^{-8}$ for InAs QDs [111] to $\beta \approx 6\times10^{-8}$ for PbSe QDs [112] with so-called interface defect QDs possibly reaching values of $\beta \approx 10^{-6}$ [113]. The coupling strength β arises naturally when recasting the expression for the spectrum, Eqs. (4.1) and (4.2) in dimensionless form. However, a large variety of different coupling parameters are used by different authors. Appendix E provides a discussion of the relation of β to the oscillator strength. The second term in Eq. (4.10) is typically vanishing and we will ignore it, leaving the approximate condition

$$\beta\frac{\tilde{\rho}_x(\tilde{\omega})}{\tilde{\omega}} \gtrsim 1. \tag{4.11}$$

We are thus left with the convenient guideline as to the kind of material systems that are likely to show fractional decay dynamics:

- The LDOS should be zero at least at one frequency, so that the we can hope to find $g(\omega_0) = 0$ and hence a real pole.
- The relative slope of the LDOS should be on the order of β^{-1} so that deviations from the Purcell regime will occur.

This is in accordance with the choices of LDOS used in Refs. [19, 20, 109]. Obvious candidates for material systems are three dimensional PCs which may show a full photonic band gap and for which the slope of the LDOS may be very large. Different models for the LDOS has been used in the literature, including both isotropic and anisotropic gap models [114] in which the LDOS at the band edge takes the forms

$$\text{(Isotropic gap)} \qquad \rho_x^{\text{iso}}(\omega) = \frac{K_{\text{iso}}}{\sqrt{\omega - \omega_{\text{BE}}}}$$

$$\text{(Anisotropic gap)} \qquad \rho_x^{\text{BE}}(\omega) = K_{\text{BE}}\sqrt{\omega - \omega_{\text{BE}}},$$

with K_{iso} and K_{BE} being material constants of dimensions $[K_{\text{iso}}] = \text{s}^{1/2}/\text{m}^3$ and $[K_{\text{BE}}] = \text{s}^{3/2}/\text{m}^3$.

The validity of both LDOS models have been questioned in the literature. Notably in Ref. [115], where the authors use dense sampling of the LDOS to conclude that the anisotropic model can be valid only in a region below $\Delta\omega^{\text{PC}} = 0.005\,(2\pi c/a)$ from the band edge. From the above analysis, however, we realize that this frequency range should be compared to the light-matter coupling strength. For the Si inverse opal ($\epsilon_{\text{Si}} = 11.76$), the upper band edge is located at $\omega_{\text{BE}} = 0.8163\,(2\pi c/a)$. If we choose to scale the photonic crystal so that the band edge is at the emitter frequency we therefore have

$$\frac{a\omega_x}{2\pi c} = 0.8163.$$

This means, that in the scaled frequencies, $\tilde{\omega} = \omega/\omega_x$, the restriction on the validity of the anisotropic model, as stated in Ref. [115], reads

$$\Delta\tilde{\omega} = 0.005\frac{2\pi c}{a\omega_x} \approx 6 \times 10^{-3},$$

which is more than 4 orders of magnitude larger than the intrinsic bandwidth set by β. In section 4.4 we show that for most spatial positions in the lattice, the limiting form of the LDOS in high-index inverse opals is indeed given by the anisotropic gap model. At this point, however, it is illustrative first to apply the analysis to this model.

4.3 Fractional decay in the anisotropic gap model

In this section the analysis in section 4.2.2 is used to investigate fractional decay in the anisotropic gap model. For convenience in the numerical modeling we will often use the scaled frequencies $\tilde{\omega} = \omega/\omega_x$. The spectrum, Eq. (4.1), is given as

$$\tilde{c}_e(\tilde{\omega}) \;=\; \frac{1}{\beta\,\tilde{G}(\tilde{\omega}) - i\,(\tilde{\omega}-1)},$$

in which the function $\tilde{G}(\tilde{\omega})$, upon insertion of the anisotropic band gap model for the LDOS, is given for frequencies above the integration path as

$$\begin{aligned}
\tilde{G}(\tilde{\omega}) \;&=\; i\,\tilde{\omega}\int_{\tilde{\omega}_{\mathrm{BE}}}^{\infty}\frac{\tilde{K}_{\mathrm{BE}}\sqrt{\tilde{z}-\tilde{\omega}_{\mathrm{BE}}}}{\tilde{z}^2(\tilde{\omega}-\tilde{z})}\mathrm{d}\tilde{z}\\
&=\; i\,\tilde{K}_{\mathrm{BE}}\,\tilde{\omega}\,\frac{\pi}{2\tilde{\omega}^2\sqrt{\tilde{\omega}_{\mathrm{BE}}}}\left(-2\tilde{\omega}_{\mathrm{BE}}+\tilde{\omega}+2\sqrt{\tilde{\omega}_{\mathrm{BE}}-\tilde{\omega}}\sqrt{\tilde{\omega}_{\mathrm{BE}}}\right)\\
&=\; -i\,\tilde{K}_{\mathrm{BE}}\,\tilde{\omega}\,\frac{\pi}{2\tilde{\omega}^2\sqrt{\tilde{\omega}_{\mathrm{BE}}}}\left(\sqrt{\tilde{\omega}_{\mathrm{BE}}-\tilde{\omega}}-\sqrt{\tilde{\omega}_{\mathrm{BE}}}\right)^2
\end{aligned}\qquad (4.12)$$

with the scaled material constant defined through the relation

$$K_{\mathrm{BE}} = \frac{\rho_0(\omega_x)}{\sqrt{\omega_x}}\tilde{K}_{\mathrm{BE}}.$$

For the calculations we will normally have $\tilde{\omega}_{\mathrm{BE}} \approx 1$. The integral representation of $\tilde{G}(\tilde{\omega})$ is valid only for frequencies above the integration path, but using Eq. (4.12) we may directly make an analytical continuation to the entire complex plane. In this way we are able to calculate the pole term and the residue to arbitrary accuracy.

By definition, the atomic frequency is at $\tilde{\omega} = 1$, so detuning of the emitter with respect to the band edge is handled by changing the value of $\tilde{\omega}_{\mathrm{BE}}$. To this end we write $\tilde{\omega}_{\mathrm{BE}} = 1 + \Delta$, in which Δ is the detuning. For large positive detunings the band edge is at much higher frequencies than the emitter frequency (the emitter is deep within the band gap), and very little or no decay at all is expected. For large negative detunings the emitter frequency is deep within the continuum of modes above the band edge and one will expect the Wigner-Weisskopf approximation to hold, leading to exponential decay.

4.3.1 Definition of the square root

There is a subtlety in Eq. (4.12) because the square root is multiple valued with values in either of two Riemann sheets as illustrated in Fig. 4.1. The branch cut is defined by the integration path which will typically be along the real axis from $\tilde{\omega}_{\mathrm{BE}}$ to infinity. It is possible, however, to define a new square root in which the

phase ϕ of the complex number $Z = |Z| \exp(i\phi)$ is chosen to lie in a given interval. Irrespective of the definition of the square root, the second Riemann sheet is found by using $-\sqrt{\tilde{\omega}_{\mathrm{BE}} - \tilde{\omega}}$ in Eq. (4.12).

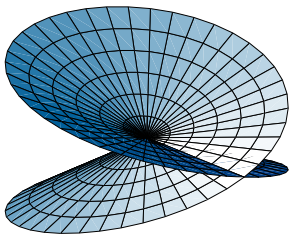

Figure 4.1: Sketch of the Riemann surface for the square root function. The function is multiple valued with values in either of two Riemann sheets. For a given point on the surface, only by circling the center twice do we arrive the same point.

Fig. 4.2 shows the absolute value of the denominator in Eq. (4.1) calculated on the two different Riemann sheets for the case of $\beta = 5.5{\times}10^{-8}, \tilde{K}_{\mathrm{BE}} = 10$ and $\Delta = 8.645{\times}10^{-7}$. We have rotated the branch cut from the real axis into the lower half of the complex plane. This means, that one pole is found on the first Riemann sheet and one is found on the second Riemann sheet. Note that the function is continuous across the branch cut in the sense that as one traverses the branch cut one should continue onto the other Riemann sheet as illustrated in Fig. 4.1.

4.3.2 Movement of poles

The pole defining the decay process is located below (or potentially on) the real axis. Fig. 4.3 shows the movement of the poles in the complex $\tilde{\omega}$ plane as the detuning is varied. For large negative detunings the pole of interest is situated to the right of and below the band edge in the complex plane. As the detuning is increased the pole wanders towards the band edge, in the process inevitably crossing over to the second Riemann sheet. At a critical detuning, Δ_0, the two (complex conjugate) poles collide on the real axis and start to move in opposite directions. For $\beta = 5.5{\times}10^{-8}$ and $K_{\mathrm{BE}} = 10$ the critical detuning is at $\Delta_0 = -8.6394 \times 10^{-7}$. At another critical detuning one of the poles reaches the band edge frequency and crosses over once again to the first Riemann sheet. The gray shaded area in the right figure indicates the interval in which the real part of the pole is less than

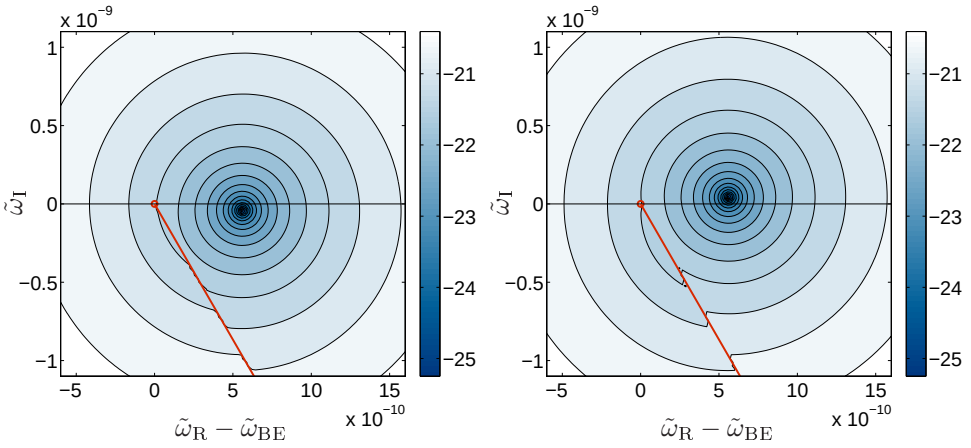

Figure 4.2: Logarithm of the absolute value of the denominator in the spectrum calculated on the first and on the second Riemann sheet, respectively, in the neighborhood of the location of the poles. The branch cut is chosen to lie in the lower half of the complex plane as indicated by the red line, thus exposing the pole just below the real axis.

the band edge. If the branch cut was chosen to be vertically downwards from the band edge, this would indicate the interval in which both poles are on the second Riemann sheet.

For convenience, we shall refer to the pole in the upper half of the complex plane as pole 1 and the other pole as pole 2. At the critical detuning we can no longer distinguish the two, but nevertheless we shall refer to the pole traveling in the direction of positive frequencies as pole 2, since this is the pole that we are ultimately interested in.

4.3.3 Residues

When the pole is on the first Riemann sheet the absolute value of the residue and the imaginary part of the pole defines the long time behavior of the temporal solution. In particular, if the pole has a non-zero imaginary part the temporal solution will eventually decay to zero. This is the case for $\Delta - \Delta_0 < 0$ as seen in figure 4.3, right. On the other hand, if the pole is located on the real axis, the temporal solution will tend to a non-zero stable value given as the absolute square of the residue. This is fractional decay and will happen at detunings above the gray shaded area in the figure. For detunings in the region of the gray shaded area there are no poles on the first Riemann sheet, and hence the pole does not define the long time behavior

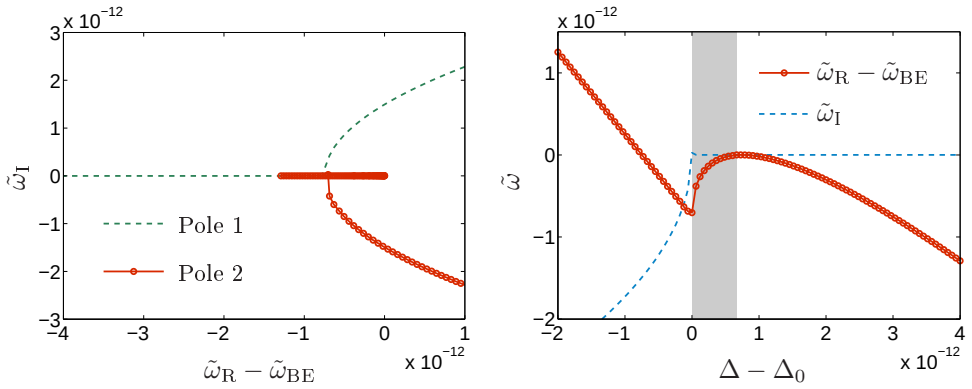

Figure 4.3: As the detuning is varied, the poles of the spectrum move around in the complex plane. Left: Movement of poles in either of the two Riemann sheets, corresponding to the two different signs of the square root. Right: Position of the pole of interest that was originally in the first Riemann sheet below the real axis. The figure shows the real and the imaginary part, respectively, as a function of the detuning Δ. $\Delta_0 = -8.6394 \times 10^{-7}$ denotes the critical detuning.

of the temporal solution.

Fig. 4.4, left shows the absolute value of the residues of the two poles as a function of the detuning Δ. Again, the gray shaded area defines the qualitatively different regimes. At large negative detunings the poles are complex conjugates and the absolute values of the residues are equal. As the poles collide on the real axis the residues seem to diverge. As noted above, this has no implications for the temporal solutions as both poles are on the second Riemann sheet. At a certain critical detuning one pole crosses over to the first Riemann sheet and the decay becomes fractional. At this detuning the absolute value of the residue is zero (corresponding to a full decay at long times) but increases with increasing detuning. Fig 4.4, right shows three examples of temporal solutions at detunings above the critical detuning where the pole reenters the first Riemann sheet and fractional decay occurs.

From Fig. 4.4 it is seen that the detuning can always be varied to achieve an arbitrarily large a degree of fractional decay. This is consistent with the analysis in sections 4.2.3 from which we know that non-Markovian dynamics are expected whenever the relative slope of the LDOS is larger than the intrinsic bandwidth set by β. In the calculations we have modelled the LDOS using a square root for which the relative slope diverges. Therefore, in principle we can always tune the frequency to obtain as large a degree of fractional decay as wanted. We note that the region of fractional decay, as defined by $|a_{-1}|^2 < 1$, extends for several decades of $\Delta - \Delta_0$,

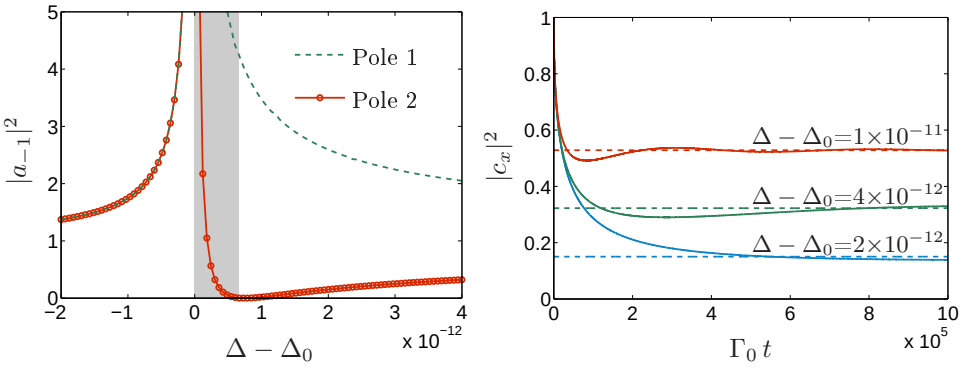

Figure 4.4: Left: Absolute value of the residues of the two poles as a function of detuning, Δ. Right: Examples of temporal solutions at three different detunings as function of normalized time $\Gamma_0 t$, where Γ_0 is the decay rate in vacuum. Dashed lines show the part of the solution corresponding to the pole term.

slowly approaching the limit $|a_{-1}|^2 = 1$.

In practice, a relative detuning of $\Delta = 10^{-12}$ means that the system will have to be stabilized to within $\Delta\omega \approx 10^3\,\mathrm{s}^{-1}$ which is several orders of magnitude finer than any available spectrometer. This apparent problem is linked to the formulation in which there seems to be only one material parameter of importance, namely the product βK_{BE}. In real samples there will likely be other important parameters defining the decay dynamics, and the obtainable degree of fractional decay will depend on the size of βK_{BE} relative to these parameters. One such parameter is the material absorption, as we will discuss in sections 4.4 and 4.5. When material losses are included in the model there will be an optimum detuning for which the degree of fractional decay is largest. In this case the optimum detuning is found within a frequency interval defined by the size of the light-matter coupling strength relative to the absorption.

4.4 High resolution local density-of-states

We now aim at applying the criterion in Eq. (4.11) to evaluate the possibility of non-Markovian decay of QDs in three dimensional PCs. To this end we must be able to assess whether or not the relative slope of the LDOS can reach values on the order of β^{-1}. This in turn puts rather severe constraints on the calculation methods employed, because the LDOS will need to be sampled at a much higher resolution than what is typical for such calculations. Fig. 4.5 shows the band diagram for a close packed inverse opal photonic crystal made from Silicon ($\epsilon_{\mathrm{r}} = 11.76$). All

plane wave calculations in this section were performed using code based on Ref. [74], kindly shared by Dr. Femius Koenderink. The band diagram shows a band gap with the upper and lower band edges defined by the W and X points in the irreducible Brillouin zone, respectively. Based on the band diagram, and the discussion of a suitable LDOS for the observation of fractional decay in Section 4.2.3, we realize that inverse opals are promising candidates for a model system showing fractional decay.

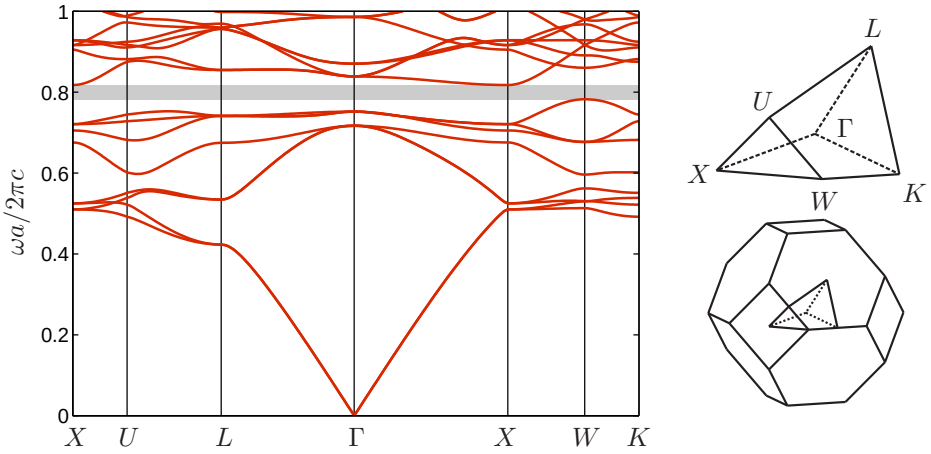

Figure 4.5: Band structure of a close packed Si ($\epsilon_r = 11.76$) inverse opal along with a sketch of the Brillouin zone. The irreducible Brillouin zone is indicated in the sketch along with the high-symmetry points.

In this section we first discuss typical calculations of the LDOS in photonic crystals using plane wave expansion. In order to evaluate the possibility of non-Markovian decay we focus on the upper band edge and set up an analytical expression for the LDOS close to the band edge based on an expansion of the relevant dispersion surfaces in powers of the $\mathbf{k}$ vector. Based on the model LDOS we next use perturbation theory to include the effects of material absorption which acts to broaden the features of the LDOS.

4.4.1 Calculations using plane wave expansion

The LDOS is typically calculated using a plane wave expansion technique [72, 73, 74]. In this way the eigenmodes are found along with the corresponding eigenfrequencies and are summed according to Eq. (2.8). The calculations result in histograms which converge to the true LDOS only in the limit of vanishing bin-width, $\Delta\tilde{\omega}$. In the case of perfect sampling in $\mathbf{k}$-space the calculations result in the

discretely sampled function $h(\tilde{\omega}_i)$,

$$h(\tilde{\omega}_i) \;=\; \frac{1}{\Delta\tilde{\omega}} \int_{\tilde{\omega}_i}^{\tilde{\omega}_i+\Delta\tilde{\omega}} \tilde{\rho}(\tilde{\omega}')\,\mathrm{d}\tilde{\omega}'. \tag{4.13}$$

In practice, however, we calculate only the solutions at a finite number of **k** points. The binwidth, $\Delta\tilde{\omega}$, and the sampling in **k**-space are intimately connected, so that

$$\Delta\tilde{\omega} \;\approx\; \Delta\mathbf{k}|\nabla\tilde{\omega}(\mathbf{k})|,$$

in which $|\nabla\tilde{\omega}(\mathbf{k})|$ represents the group velocity [74]. This means that smaller binwidth necessarily comes at the price of finer sampling in **k**-space and hence longer calculation times.

Fig. 4.6 shows an example of the function $h(\tilde{\omega}_i)$ at the Γ and P points of a close packed Si inverse opal (hole radius per lattice constant $R/a = 1/\sqrt{8} \approx 0.3536$). The binwidth in the calculations was $\Delta\tilde{\omega} = 0.005$ and the histograms were calculated using 725 plane waves and 26670 **k** points in half of the first Brillouin zone. The small binwidth was chosen in order to illustrate the limiting form of $h(\tilde{\omega}_i)$ close to the band edge as seen in the insets. Despite the large number of **k** points, the overall appearance of the LDOS histograms is somewhat rugged and irregular spikes indicate that the number of data points (one for each band at each **k** point) is almost too low for the chosen binwidth. For the same reason we were forced to lower the number of plane waves for these calculations - the analysis in section 4.4.2 is carried out using 1243 plane waves. The appearance of the LDOS histograms can be smoothened by using a larger binwidth or a larger number of **k** points at the prize of longer computation times as discussed above. Although the number of **k** points is large, it is by no means unique in the literature. For comparison, the results in Ref. [74] were obtained using 145708 **k** points and a binwidth of $\Delta\omega = 0.01(2\pi c/a)$ (roughly equivalent also to $\Delta\tilde{\omega} = 0.01$). We note that chosen binwidth is comparable to the binwidth in Ref. [115] in which the anisotropic band gap model was questioned based on the appearance of the LDOS histograms close to the band edge. From the insets in Fig. 4.6 we see that the LDOS at the Γ point does in fact follow a square root behavior close to the gap, whereas the LDOS at the P point does not.

4.4.2 Detailed analysis of the band edge

As discussed in section 4.2.3, the binwidth $\Delta\tilde{\omega} = 0.005$ is four orders of magnitude too large to sample the slope of the LDOS that is required for non-Markovian decay to be observable. Therefore, in this section we take a semi-analytical approach in which the numerical dispersion curves close to the band edges are approximated by

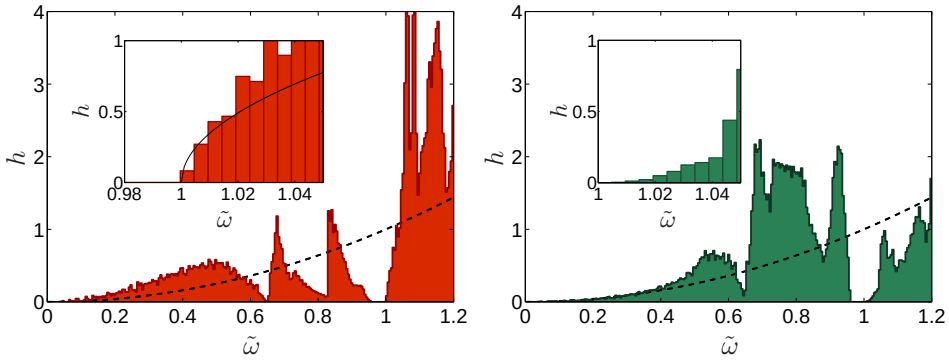

Figure 4.6: Examples of discrete samplings $h(\tilde{\omega}_i)$ of the LDOS of the Si inverse opal at the Γ (left) and P (right) points in the Wigner-Seitz cell. In both histograms the band gap is clearly visible just below $\tilde{\omega} = 1$. Dashed curve indicates the scaled LDOS in free space $\tilde{\rho}_0 = \tilde{\omega}^2$. In both figures, the inset shows a zoom in at values close to the upper band gap edge. The black curve in the left inset shows the limiting square root behavior of the LDOS close to the band edge.

analytical functions and integrated to get an analytical expression for the LDOS. The LDOS is given originally as the sum in Eq. (2.8) which may be written, in the limit of large quantization volume, as an integral,

$$\rho_x(\mathbf{r},\omega) \;=\; \sum_p \frac{V}{(2\pi)^3} \int |\mathbf{e}_x \cdot \mathbf{f}_\mu(\mathbf{r})|^2 \delta(\omega - \omega_\mathbf{k})\, \mathrm{d}\mathbf{k},$$

where the sum is now over the two polarizations p only. Owing to the periodic structure of the material, the frequencies are defined by $\mathbf{k}$ vectors in the first Brillouin zone only and may be ordered in bands of index n. Considering the contribution from just a single band, one may use standard methods from solid state physics [116, 117] to rewrite the integral as

$$\rho_x(\mathbf{r},\omega) \;=\; \sum_p \frac{V}{(2\pi)^3} \int_{S_n(\omega)} \frac{|\mathbf{e}_x \cdot \mathbf{f}_\mu(\mathbf{r})|^2}{|\nabla\omega_n(\mathbf{k})|}\, \mathrm{d}S, \tag{4.14}$$

in which the integral is now over the surface of constant frequency in the n'th band. Appendix D.1 illustrates the procedure for the homogeneous medium.

Close to the band edge, the LDOS of the Si inverse opal is defined only by the ninth band. Further, the band edge is defined only by the high-symmetry point X in $\mathbf{k}$-space, which means that the dispersion surface is an ellipsoid. By making a suitable expansion of the integrand in Eq. (4.14) in terms of $\mathbf{k}$ we may evaluate the resulting integral analytically to obtain the correct behavior of the LDOS. The

integral is carried out over the dispersion surface in the first Brillouin zone. However, one cannot restrict the analysis to the irreducible Brillouin zone because the projected mode functions, $|\mathbf{e}_x \cdot \mathbf{f}_\mu(\mathbf{r})|$, are not invariant under the symmetry operations that applies to the underlying lattice [73]. Details of the calculations may be found in Appendix F. By expanding the dispersion surface in a coordinate system centered on the X point as

$$\omega \;=\; \omega_0 + \frac{1}{2}\left(\omega_{xx}k_x^2 + \omega_{yy}k_y^2 + \omega_{zz}k_z^2\right)$$

it is shown that to lowest order in ω the limiting form of the LDOS at the band edge is given by the anisotropic gap model as

$$\rho_x^{\mathrm{BE}}(\mathbf{r},\omega) = \frac{I_x}{(2\pi)^2}\sqrt{\frac{2}{\omega_{xx}^2\omega_{zz}}}\sqrt{\omega-\omega_{\mathrm{BE}}} = K_{\mathrm{BE}}\sqrt{\omega-\omega_{\mathrm{BE}}}, \tag{4.15}$$

where ω_{xx} and ω_{zz} denote, respectively, the curvatures of the dispersion surface in the directions parallel and perpendicular to the Brillouin zone surface and where

$$I_x = V\sum_{n=1}^{6}|\mathbf{e}_x \cdot \mathbf{f}_\mu(\mathbf{r}, X_n)|^2$$

denotes the sum of the projected field strength at the 6 X points in the Brillouin zone. For non-vanishing I_x the band edge is seen to follow the square-root behavior of the anisotropic gap model. The solid curve in the inset of Fig. 4.6 (left) illustrates how the analytical approximation conforms to the purely numerical histogram close the band edge.

Fig. 4.7 shows the values of K_{BE} along lines between symmetry points of the Wigner-Seitz cell of a Si inverse opal with hole radius per lattice constant of $R/a = 0.3436$. The analytical approach allows for the use of only 5 $\mathbf{k}$ points in each direction for the determination of the curvature and we have used 1243 plane waves to ensure convergence. The maximum value of K_{BE} is found at the H point (blue sphere in the sketch of the inverse opal unit cell in Fig. 1.7). This value may be further increased by reducing the radius of the air spheres as shown by the dashed curve in Fig. 4.7. The large value of K_{BE} at the H point makes this the position in the crystal where non-Markovian effects are most pronounced.

The radius of the air spheres $R = 0.3436\,a$ used in the calculation of Fig. 4.7. is slightly less than that of the close packed crystal. For the close packed crystal the air spheres touch at the N points. This means that the thickness of the dielectric vanishes at these points, resulting in a divergence of the electric field component parallel to the surfaces of the spheres. The effect is visible already at the chosen value of R/a as a pronounced increase of the value of K_{BE} for the x polarization.

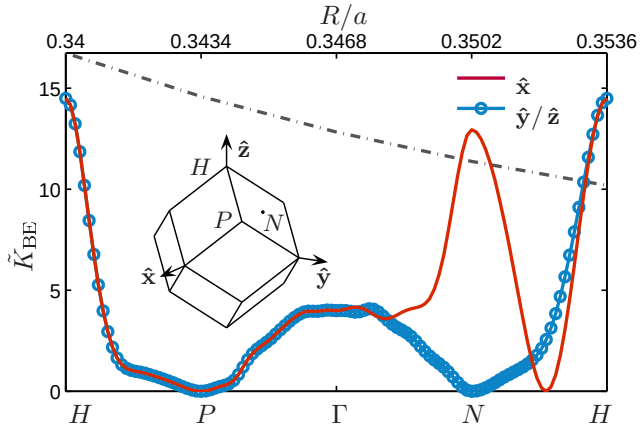

Figure 4.7: The parameter K_{BE} (in units of $\rho_0(\omega_x)/\omega_x^{1/2}$) as a function of position in the Wigner-Seitz cell (shown in the inset) for the three principal emitter orientations. Grey dash-dotted line shows values of K_{BE} at the H point for different R/a (top scale).

In addition to the numerical problems at the N point, we experienced some trouble converging the results for the z polarized emitter at positions along the $\Gamma - H$ route. Since these positions are less relevant for the discussion in this work we have left them out.

4.4.3 Influence of material loss

In order to introduce loss in the material, a small imaginary part is added to the permittivity,

$$\epsilon_{\mathrm{R}} \to \epsilon_{\mathrm{R}} + i\,\epsilon_{\mathrm{I}},$$

which in turn leads to a small (imaginary) shift in frequency. For small losses we use first order perturbation theory [64, 118, 119] to write $\omega = \omega^{(0)} - i\delta$, where $\omega^{(0)}$ is the frequency in the absence of losses and

$$\delta = \frac{\omega^{(0)}}{2}\,\frac{\langle \mathbf{E}_\mu | i\,\epsilon_{\mathrm{I}} | \mathbf{E}_\mu \rangle_{\mathrm{C}}}{\langle \mathbf{E}_\mu | i\,\epsilon_{\mathrm{R}}(\mathbf{r}) | \mathbf{E}_\mu \rangle_{\mathrm{V}}} = \frac{\omega^{(0)}\epsilon_{\mathrm{I}}}{2\,\epsilon_{\mathrm{R}}}\,f,$$

where subscript C denotes the volume of the lossy material only, and subscript V denotes the entire volume. The parameter f is given as

$$f = \frac{\langle \mathbf{E}_\mu | \epsilon_{\mathrm{R}}(\mathbf{r}) | \mathbf{E}_\mu \rangle_{\mathrm{C}}}{\langle \mathbf{E}_\mu | \epsilon_{\mathrm{R}}(\mathbf{r}) | \mathbf{E}_\mu \rangle_{\mathrm{V}}} < 1$$

and is a measure of the concentration of the electric field energy in the high-index material [64]. In this part of the calculation we do not worry about the actual mode

profiles, but simply set $f = 1$ to get an upper bound for δ. If the material loss is assumed to be independent of $\mathbf{k}$ we may rewrite the band edge LDOS in Eq. (4.15) as [120]

$$\rho_x^{\mathrm{BE}}(\mathbf{r},\omega) = K_{\mathrm{BE}}(\mathbf{r}) \int_{\omega_{\mathrm{BE}}}^{\infty} \sqrt{z-\omega_{\mathrm{BE}}}\, \frac{\delta/\pi}{(\omega-z)^2+\delta^2}\, \mathrm{d}z, \tag{4.16}$$

in which we can identify a Lorentzian approximation to the Dirac δ-function illustrating that the effect of absorption is to broaden the modes. For $\delta \to 0$ we recover the square root LDOS of the anisotropic gap model. The integral may be readily calculated to yield the LDOS in closed form:

$$\rho_x^{\mathrm{BE}}(\mathbf{r},\omega) = K_{\mathrm{BE}}(\mathbf{r})\, \frac{\delta}{\sqrt{2\sqrt{(\omega-\omega_{\mathrm{BE}})^2+\delta^2}-2(\omega-\omega_{\mathrm{BE}})}}. \tag{4.17}$$

Fig. 4.8 shows the LDOS close to the band edge at zero detuning for three different values of the loss parameter δ. For $\omega \gg \omega_{\mathrm{BE}}$ the function tends to the square root behavior of the lossless crystal, whereas for $\omega < \omega_{\mathrm{BE}}$ it remains non-zero and extends below the band edge of the lossless crystal.

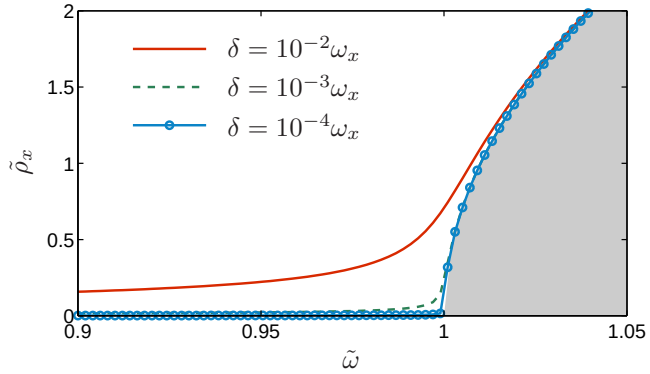

Figure 4.8: LDOS close to the band edge at zero detuning for $\tilde{K}_{BE} = 10$ and three different values of the loss parameter δ. Clearly, as $\delta \to 0$ we recover the square root function of the anisotropic gap model indicated in Gray.

The inclusion of loss in the material compromises the expansion, Eq. (2.8), of the LDOS in the eigenmodes of the vector Helmholtz equation. In this case the problem can be reformulated in terms of the electromagnetic Green's tensor [121]. The Green's tensor approach ensures that the quantization is consistent with the Kramers-Kronig relations as well as the canonical commutation relations for the electromagnetic field operators. This method avoids the use of a mode-decomposition of the LDOS, which in principle is not possible in lossy materials

with refractive index $n = n_{\mathrm{R}} + in_{\mathrm{I}}$ because the modes are not normalizable. In the case of a full Green's tensor approach the equations of motion will be the same as in our treatment, the only difference being that the LDOS is replaced by the imaginary part of the Green's tensor. It is shown in Ref. [121] that in the limit of small loss, $\epsilon_{\mathrm{I}} \ll \epsilon_{\mathrm{R}}$, the two formulations coincide, and therefore the perturbative approach is valid. An illustrative example is provided in Ref. [122] where an increase of n_{I} is shown to broaden the features in the imaginary part of the Green's tensor similar to the introduction of modes in the gap below the band edge observed in Fig. 4.8.

4.5 Fractional decay of quantum dots in inverse opals with material losses

We now consider a specific example of colloidal PbSe QDs, emitting at $\omega_x = 1.3 \times 10^{15}\mathrm{s}^{-1}$ ($\beta = 5.5 \times 10^{-8}$ [112]) and placed at the H point in a close packed Si inverse opal for which we set $K_{\mathrm{BE}} = 10\rho_0(\omega_x)/\omega_x^{1/2}$ in accordance with the calculation results in Fig. 4.7.

4.5.1 Calculation of the spectrum

For the case of the LDOS in Eq. (4.17), the integral expression for $G(\omega)$, Eq. (4.2), can no longer be evaluated analytically. This means that we cannot make a direct analytical continuation into the lower part of the complex plane as we did for the analysis of fractional decay in the anisotropic gap model in section 4.3. Instead the integral is evaluated numerically. In that case a branch cut is introduced along the integration path which may result in the pole not being visible on the resulting Riemann sheet. However, the poles may in that case be found by extending the integration path from the real axis into the complex plane. Fig. 4.9 illustrates the procedure for the case of $\delta = 0$ corresponding to the anisotropic band gap model. By integrating along an ellipse into the lower part of the complex plane we recover the position of the pole from the analytical result in Fig. 4.2.

In a similar way we are able to perform an integration into the upper part of the complex plane to reveal the second pole. Note however, that the two poles are located on different Riemann sheets. The spectrum is given through Eq. (4.2) for frequencies above the branch cut only which means that only the pole in the lower part of the complex plane is of relevance in the calculation of the spectrum. When losses are included the situation is complicated by the fact that the extra square roots in Eq. (4.17) introduce branch cuts of their own. Defining $u = \tilde{\omega} - \tilde{\omega}_{\mathrm{BE}}$, the

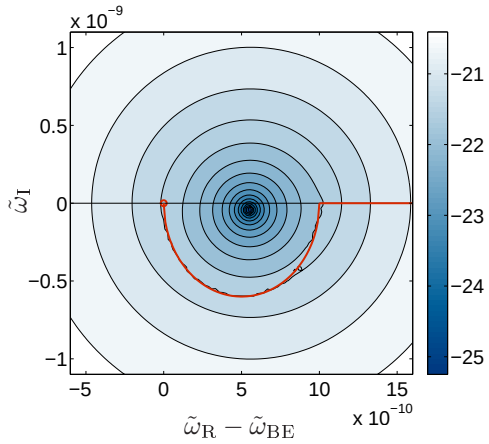

Figure 4.9: Logarithm of the absolute value of the denominator in Eq. (4.12) calculated by numerical quadrature along the elliptical path extending into the lower half of the complex plane, in this way exposing the pole.

LDOS is written for convenience as

$$\tilde{\rho}(u) \;=\; \tilde{K}_{\mathrm{BE}}\,\frac{\delta}{\sqrt{2}}\sqrt{\frac{1}{\sqrt{u^2+\delta^2}-u}}.$$

If the inner square root is chosen to have branch cuts along the negative real axis, the function $1/(\sqrt{u^2+\delta^2}-u)$ will have branch cuts extending vertically upwards from $u = i\delta$ and downwards from $u = -i\delta$, as illustrated in Fig. 4.10. For finite

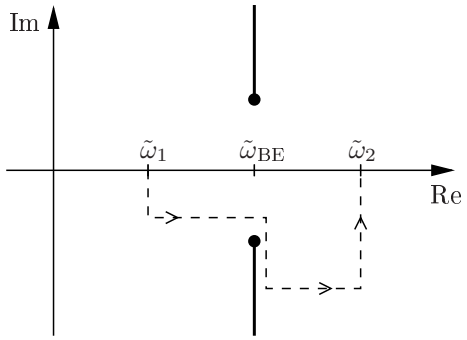

Figure 4.10: Branch cuts of the function $1/(\sqrt{u^2+\delta^2}-u)$. Also shown in the figure is the integration path into the lower part of the complex plane, revealing the position of the pole.

loss we integrate from a lower cutoff, $\tilde{\omega}_1$, to an upper cutoff, $\tilde{\omega}_2$, along a path in the lower part of the complex plane and expose the relevant pole, cf. Fig. 4.10.

When carrying out calculations using the analytical result for the lossless LDOS it was necessary to define a new branch cut of the square root, cf. section 4.3.1. For the direct numerical calculations, however, we may simply choose the branch cuts of both square roots in Eq. (4.17) to be along the negative real axis. This reproduces the analytical result in the case of no loss (simple square root LDOS) in the limit of vanishing loss $\delta \to 0$ in Eq. (4.17). For investigations of fractional and near-fractional decay we choose to integrate along the contour indicated by the dashed line in Fig. 4.10. This ensures that the pole is exposed for the detunings that are relevant in these calculations.

4.5.2 Decay dynamics in crystals with material losses

We now turn to the calculations of decay dynamics in the case of material losses. As we have emphasized in section 4.2.3, the decay is a resonant process and is governed by the LDOS in a narrow frequency interval around $\tilde{\omega} = 1$. The remaining LDOS contributes an overall Lamb shift to the spectrum. To model this effect we include an integration using $\rho_x = \rho_0$ for $\tilde{\omega} < \tilde{\omega}_1 = 0.95$ (corresponding to the lower band edge) and for $\tilde{\omega} > \tilde{\omega}_2 = 1.01$. A cutoff is chosen at $\tilde{\omega}_C = 10^5$ corresponding to the Compton frequency [62]. For $0.95 < \tilde{\omega} < 1.01$ the integral is carried out using the accurate band edge LDOS $\rho_x(\mathbf{r}, \omega) = \rho_x^{\mathrm{BE}}(\mathbf{r}, \omega)$ in Eq. (4.17).

Fig. 4.11 shows decay curves calculated using the LDOS of a Si inverse opal with added material losses. The decay curves are calculated using different material loss and a constant detuning of $\Delta = -8.309 \times 10^{-7}$. For vanishing losses the

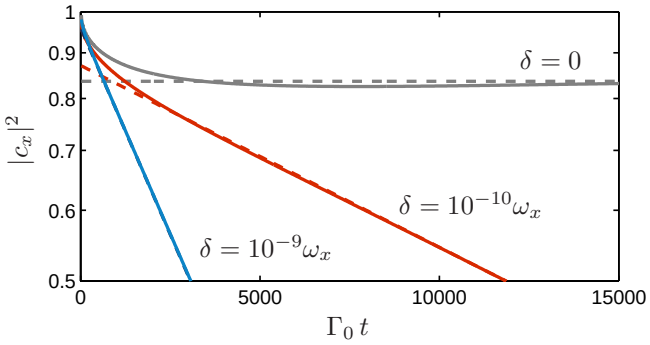

Figure 4.11: Decay from PbSe QDs at the H point in an Si inverse opal ($\beta K_{BE} = 5.5 \times 10^{-7}$) at detuning $\omega_{BE}/\omega_x = 1 - 8.309 \times 10^{-7}$ and different losses as indicated. Dashed curves show exponential parts only.

population tends to a non-zero value at long times with $d_f = 0.16$. At small finite losses a fractional effect is still visible with $d_f = 0.13$ at an absorption of $\alpha = 3 \times 10^{-5}\text{cm}^{-1}$ ($\delta/\omega_x = 10^{-10}$) and $d_f = 0.04$ at $\alpha = 3 \times 10^{-4}\text{cm}^{-1}$ ($\delta/\omega_x = 10^{-9}$). We note that absorption in Si at this frequency may be as low as $\alpha \approx 10^{-7}\text{cm}^{-1}$ ($\delta/\omega_x \approx 10^{-13}$) [123]. Fig. 4.11 therefore shows that fractional decay may be observable for real QDs in dielectric photonic crystals exhibiting absorptive losses.

At this point we return again to the validity of the perturbative inclusion of losses in the calculation of the LDOS. We now realize that the losses considered in this work are indeed extremely small and correspond to length scales that far exceed the size of typical photonic crystals. The absorption length is $L = 33\,\text{m}$ for $\alpha = 3{\times}10^{-4}\,\text{cm}^{-1}$ which is the largest value of the absorption coefficient used. Therefore the criterion $n_I << n_R$ is certainly met in our calculations and the perturbative approach is fully valid.

For a given material system the detuning of the emitter relative to the band edge defines the exact modes, and hence the group velocity, of the emitted light. This was illustrated in the left panel of Fig. 4.4 for the anisotropic gap model of the LDOS. In Fig. 4.12 we show similar calculations for the LDOS in Eq. (4.17) in the case of constant material absorption $\delta = 5{\times}10^{-10}\omega_x$ and three different values of βK_{BE}. For small values of the light-matter coupling strength there is hardly any minimum to be seen, whereas for the larger values of βK_{BE} the curve corresponds

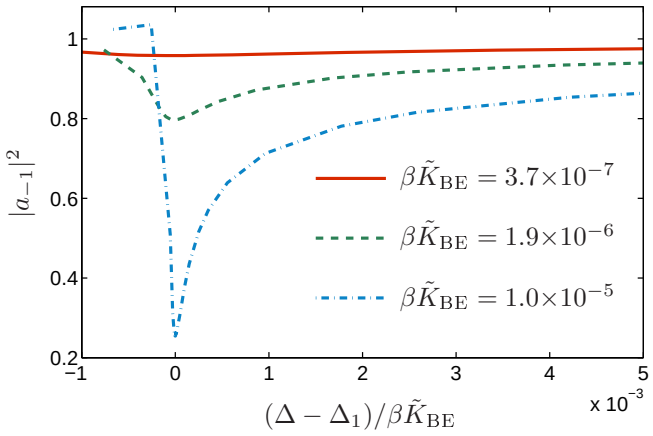

Figure 4.12: Absolute square of the residue $|a_{-1}|^2$ as a function of scaled detuning $(\Delta - \Delta_1)/\beta\tilde{K}_{BE}$, where Δ_1 is the detuning corresponding to the minimum. The material loss is $\delta = 5{\times}10^{-10}\omega_x$ and the three curves correspond to different light-matter coupling strength $\beta\tilde{K}_{BE}$ as indicated. Note that both Δ_1 and $\beta\tilde{K}_{BE}$ is different for the three curves.

more closely to the zero loss case in Fig. 4.4. We note that for $\beta\tilde{K}_{\mathrm{BE}} = 1{\times}10^{-5}$ the relative detunings are on the order of $\Delta \approx 10^{-8}$ which means, that the system should be stabilized within $\Delta\omega \approx 10^{7}\,\mathrm{s}^{-1}$.

Fig. 4.12 shows that when material absorption is included in the model it is no longer possible to achieve an arbitrarily large degree of fractional decay. Rather there is an optimum detuning that will give the largest possible effect and we therefore define the parameter D_{f} as the maximum value of $d_{\mathrm{f}} = 1 - |a_{-1}|^2$ for optimized detuning. In Fig. 4.13 we show D_{f} as a function of $\beta\tilde{K}_{\mathrm{BE}}$. The curves were obtained for each $\beta\tilde{K}_{\mathrm{BE}}$ by varying the detuning as in Fig. 4.12 in order to find the maximum value of d_{f}. The figure shows that a profound degree of fractional decay is possible for a range of experimentally relevant material parameters. However, as discussed above the resonant nature of the phenomenon may be a problem since the system will have to be stabilized within a very narrow frequency interval.

Larger values of $\beta\tilde{K}_{\mathrm{BE}}$ will lead to larger frequency intervals for which $|a_{-1}|^2 < 1$ and thus relax the stabilization requirements. The chosen parameter values are consistent with the analysis in section 4.4 but leads to a very narrow frequency interval. We note that Ref. [62] used a less conservative estimate of this parameter and found fractional decay within a larger bandwidth on the order of the decay rate. This does not seem to conform to the results obtained for Si inverse opals but may hold for other material systems.

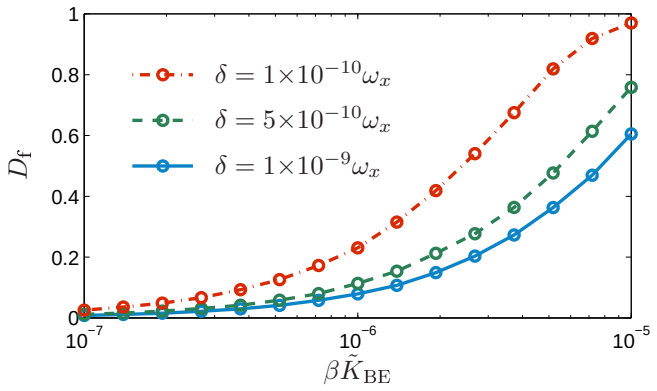

Figure 4.13: Degree of fractional decay obtainable versus light-matter coupling strength, βK_{BE}, at different absorption, δ, as indicated.

4.6 Conclusion

In conclusion we have investigated QD decay dynamics using a Laplace transform technique in which the equations of motion are solved in the frequency domain to reveal the spectrum. The spectrum may be conveniently split into a pole term and a rest term. We have discussed how properties of the pole term in a given spectrum may be used to define deviations of the decay dynamics from the Purcell regime of exponential decay. Motivated by this discussion we have defined a measure for the degree of fractional decay, and as an example we have applied the measure to decay curves calculated in the anisotropic band gap model. In this model one can in principle obtain an arbitrarily large degree of fractional decay by tuning the emitter precisely into resonance with the modes of vanishing group velocity at the band edge. We have discussed how this is a mathematical artifact due to the simplicity of the model for the LDOS.

In order to model real PCs we used an analytical expression to the band edge LDOS in inverse opals. This allowed us to investigate which positions in the crystal that are most suitable for observation of fractional decay. Furthermore, we have extended the analysis to include absorptive losses and calculated the degree of fractional decay obtainable for given losses and light-matter coupling strengths. Contrary to the lossless material case, it turns out that there is an optimum detuning for which the degree of fractional decay is the largest. This optimum detuning depends on the material loss and the light-matter coupling strength. The analysis shows that absorption has a limiting but not prohibitive effect and that fractional decay may be possible to achieve, e.g. using PbSe QDs in Si inverse opals. The experimental verification, however, may be difficult since the system will have to be stabilized within a very narrow frequency interval. This is clearly on the very edge (and possible beyond) what can be measured with today's spectrum analyzers. However, the analysis shows that fractional decay may be within reach of experimental verification if one can find a suitable material system.

Chapter 5

Multiple quantum dots in photonic crystal slabs

5.1 Introduction

QDs not only act as sources for the light but also inevitably lead to additional scattering. The mere inclusion of a QD in an otherwise perfect PC will change the electromagnetic response of the system as described by the Green's tensor. The linewidth of typical QDs, however, is extremely narrow compared to the spectral properties of most PCs. In many cases this allows us to apply the Wigner-Weisskopf approximation in calculations of spontaneous emission as discussed in sections 2.4.3 and 4.2.3. In the context of light scattering, it means that the QDs will act as scatterers within a very narrow frequency interval only.

In this chapter we work in an all light picture to investigate how resonant interaction of neighbor QDs within a PC slab affects spontaneously emitted light. The Green's tensor arises naturally in calculations of light emission and propagation in micro structured media such as PCs. Indeed, according to Eq. (2.44) the electric field at point $\mathbf{r}$ due to a point source at $\mathbf{r}_x$ is given as

$$\mathbf{E}(\mathbf{r}_\mathrm{d}, \omega) = \mathbf{G}^{(1)}(\mathbf{r}_\mathrm{d}, \mathbf{r}_x, \omega)\mathbf{S}_x(\omega),$$

where $\mathbf{G}^{(1)}(\mathbf{r}_\mathrm{d}, \mathbf{r}_x, \omega)$ contains the exciton self-interaction. Apart from the effect of the QD itself we have made no assumptions about the Green's tensor and so, in principle, it could contain scattering contributions from other QDs in the sample. This is the main idea behind the approach that we will take in this section where the effect of scattering due to QDs are added to the Green's tensor for the passive crystal using a self-consistent Dyson equation approach. Our procedure is somewhat

similar to the iterative method that has been developed by Martin *et al.* for the evaluation of the Green's tensor in the CDA [55]. It has recently been used for the investigation of QD light emission [56] and entanglement [57] in PC cavity systems for which analytical approximations to the Green's tensor were used. In this work we present the method in a general form and apply it to a numerically calculated Green's tensor.

Calculations of the Green's tensor for experimentally relevant structures can be very time-consuming, but it may be worth the effort as the Green's tensor includes in principle information of all scattering channels in the structure. For the calculations in this chapter we use FDTD calculations for the background Green's tensor and focus on finite sized photonic crystallites in a dielectric slab. Similar PCs have previously been investigated in Ref. [68] in which the LDOS was calculated at a number of positions within the Wigner-Seitz cell. Contrary to Ref. [68] we present both local properties $\mathbf{G}(\mathbf{r},\mathbf{r})$ and non-local properties $\mathbf{G}(\mathbf{r},\mathbf{r}')$ describing the interaction of spatially separated QDs within the PC.

The Green's tensor governs not only the coupling between QDs within the PC but also propagation to the detector above the PC membrane. In an all light picture we solve for the dynamics of the electric field operators at a given location corresponding to the detector. In many experiments, such as the one described in section 1.1, we are not interested in the electric field itself but rather the intensity. Indeed, in a number state, such as the one photon state, the number of photons and hence the energy is well defined. The electric field on the other hand is not, and the expectation value of the electric field operator vanishes [63]. We therefore focus on the intensity of the emitted light at the position of the detector and show how the resonant interaction with other QDs may qualitatively change the expectation value from that of the one QD case.

5.1.1 Overview of chapter 5

Section 5.2 presents calculations of the Green's tensor for a finite sized photonic crystallite in a dielectric slab. In addition, we discuss how many of the properties of the Green's tensor in this case can be understood from a simple schematic mode description. In section 5.3 we introduce the method for modeling nanophotonic structures with several QDs. The method is presented in a general form that allows for direct interpretation in terms of different possible scattering channels by which the light can travel from a QD to the detector. In addition, we discuss how the method may be extended to account for local field corrections in a simple and intuitive manner. Finally, in section 5.4 the results of sections 5.2 and 5.3 are combined to study spontaneous decay dynamics of a two QD system in which an excited QD within the sample is influenced by another spatially separated QD.

5.2 Finite sized photonic crystallite in dielectric slab

This section studies light scattering in finite sized photonic crystallites as described by the Green's tensor. Whereas the LDOS has been calculated for a number of infinite PCs as well as finite sized two and three-dimensional structures, there has only been a limited number of publications concerned with the general Green's tensor. To aid us in understanding various contributions to the Green's tensor we employ band structure calculations, since properties of the band structure show up in even fairly small periodic structures.

The material system under investigation consists of a slab of GaAs ($n = 3.523$) of thickness $h = 150\,\mathrm{nm}$ with a finite-sized hexagonal PC of air holes with radius $r = 93.3\,\mathrm{nm}$. The lattice constant is $a = 298\,\mathrm{nm}$, so that $r/a = 0.313$. The periodic arrangement is terminated to form a small hexagonal crystallite with side length L as illustrated in Fig. 5.1. The crystallites are similar to those investigated in Ref. [68], except that material parameters have been changed slightly to match those used in the experiment by Julsgaard *et al.* [23].

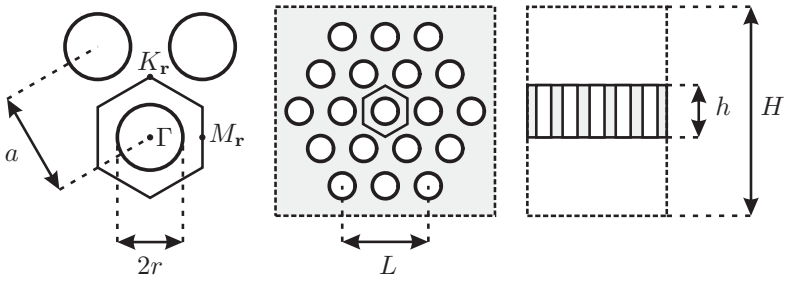

Figure 5.1: Sketch of the crystallites investigated in this work. Of special importance are the high-symmetry points in the center and along the edge of the Wigner-Seitz cell. In this work we focus on the points $\Gamma = (0,0,0)$, $K_\mathbf{r} = (0, a/\sqrt{3}, 0)$ *and* $M_\mathbf{r} = (a/2, 0, 0)$.

For the applications in section 5.4 the QDs are assumed to be placed inside the crystal as in Ref. [23] to act as sources of single photons. We therefore consider only positions in the middle of the slab. Maxwell's equations are scalable in the sense, that if we scale all lengths in the system, the solutions must be the same but for a scaling of the frequency. To scale all lengths, however, the thickness of the slab needs to be scaled as well. This means that the results in this work does not immediately apply to the analysis of results obtained in Ref. [23] for other choices of r/a.

5.2.1 Photonic crystal slab analysis

For the analysis we first calculate the band diagram of the infinite PC slab. Fig. 5.2 shows results for the even modes calculated with both the plane wave method and FDTD as discussed in section 2.2.5. The plane wave calculations were performed using the free plane wave software package `mpb` by Steven G. Johnson, which is based on Ref. [70]. FDTD calculations were done using the commercial FDTD software FDTD solutions from Lumerical Inc. We have left out the odd modes in Fig. 5.2 since the QDs in section 5.4 are assumed to be placed in the center of the slab and thus couple only to even modes. The plane wave method is restricted to frequencies inside the light cone (illustrated in grey), whereas the FDTD method allows us to track the modes also at frequencies outside the light cone. Horizontal dashed lines in the figure indicate frequencies of special interest in the present study; the frequency of the first band at the M point and the frequencies defining the in-plane bandgap between the first band at the K point and the second band at the M point.

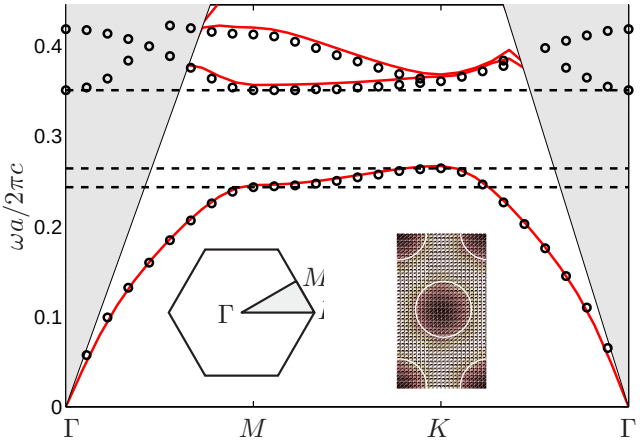

Figure 5.2: Band diagram for even modes in the infinite PC slab calculated with both the plane wave method (red solid line) and using FDTD (circles). The light cone is indicated by the gray shading. Inset shows the Brillouin zone along with high-symmetry points and the mode profile at the K point.

5.2.2 Green's tensor and the local density-of-states

We now turn to the results of the Green's tensor calculations using FDTD. Appendix H provides an overview of the calculation procedure. Visualization of the

full Green's tensor is difficult for several reasons. The vector nature of the electromagnetic field means that the Green's tensor consists of nine complex scalars, each of which has a two fold spatial dependence as well as a frequency dependence. We will restrict the analysis to the to positions $K_{\mathbf{r}}$ and $M_{\mathbf{r}}$ and plot different elements of the tensor as function of frequency.

Of particular interest in the context of light emission from QDs is the projected LDOS which is proportional to the imaginary part of the Green's tensor at $\mathbf{r} = \mathbf{r}'$. Fig. 5.3 shows the x-projected LDOS at the $K_{\mathbf{r}}$ point (as illustrated in Fig. 5.1) in the Wigner-Seitz cell centered on the central air hole in a crystallite of size $L = 6\,a$. Comparing to the band structure in Fig. 5.2 the in-plane band gap is clearly visible as a pronounced depletion of the LDOS over a wide frequency interval.

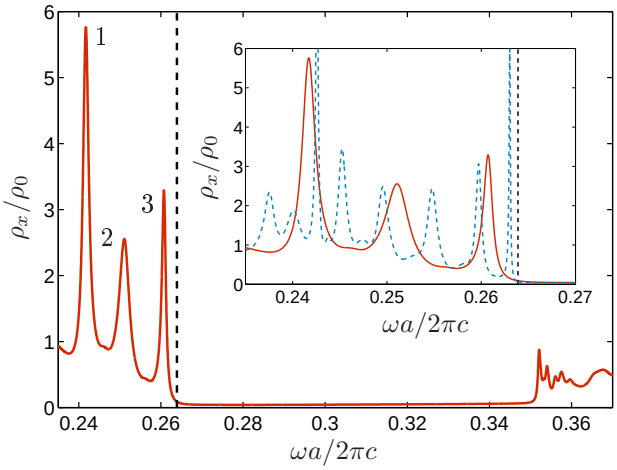

Figure 5.3: X-projected LDOS at the $K_{\mathbf{r}}$ point in a crystallite of size $L = 6\,a$. The LDOS is normalized to that of the homogeneous material, so that the curves correspond to the Purcell effect. Inset: Zoom in on the LDOS at frequencies close to the lower band edge. Also shown (blue dashed line) is the case $L = 12\,a$ showing additional Fabry-Perot like resonances. Vertical dashed lines indicate the (lower) band edge of the infinite crystal.

We note that peak 3 does not coincide with the band edge as calculated in Fig. 5.2 due to the finite size of the structure. In the inset we show a zoom in of the LDOS at frequencies below the band gap. Also, we show the x-projected LDOS at the same point, but for a crystallite of size $L = 12\,a$. The sharp resonances at peaks 1 and 3 shift in this case, so that the position of peak 3 seems to converge towards the in-plane band edge as the size of the crystal is increased. We have calculated the LDOS for a number of different sizes of structures including $L = 18\,a$ which

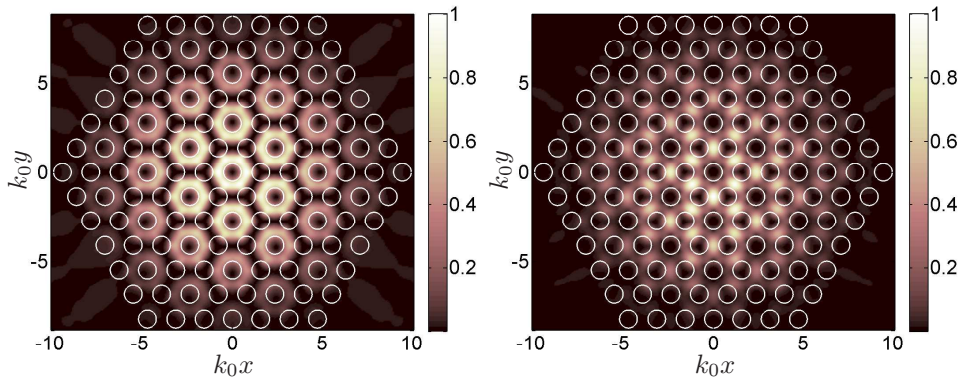

Figure 5.4: Normalized mode profiles at constant frequency $\omega a/2\pi c = 0.26$, corresponding to peak 3 in Fig. 5.3 as excited by an x-oriented (left) and a y-oriented (right) polarization point source at the $K_\mathbf{r}$ point indicated by the white dot.

seems to confirm this assumption.

The peaks in the LDOS are due to Fabry-Perot like resonances that shift depending on the size of the crystallite [68]. Using a run-time fast fourier transform [124] we may further investigate the nature of the resonances by calculating the field at specific frequencies. Fig. 5.4 shows the normalized intensity of the field at $\omega a/2\pi c = 0.26$ corresponding to peak 3 in Fig. 5.3 as excited by both an x-oriented and a y-oriented polarization point source at the $K_\mathbf{r}$ point. The calculations were done with an apodization to filter out the contribution from the source at early times, and the fields thus represent the (quasi) modes of the structure that are initially excited by the source and decays with a finite lifetime given by the width of the peaks in the LDOS. The field profiles in Fig. 5.4 display a periodic structure multiplied by an envelope function to account for scattering at the crystallite edges. In addition, the left figure is somewhat similar to the profile of the Bloch mode in the inset of Fig. 5.2, confirming that the crystallite acts as a confinement potential for the Bloch modes.

Left panel of Fig. 5.5 shows the projected LDOS at the positions $K_\mathbf{r}$ and $M_\mathbf{r}$. At $\omega a/2\pi c = 0.26$ we observe a quenching of the x-projected LDOS at the $M_\mathbf{r}$ point and a corresponding increase in the y projected LDOS. Light propagation between the two points is described by the Green's tensor $\mathbf{G}(K_\mathbf{r}, M_\mathbf{r}, \omega)$. In the right panel of Fig. 5.5 we show the four elements that are relevant for in-plane oriented electric fields. We notice a pronounced peak of the element G_{xy} and a quenching of the element G_{xx} at $\omega a/2\pi c = 0.26$.

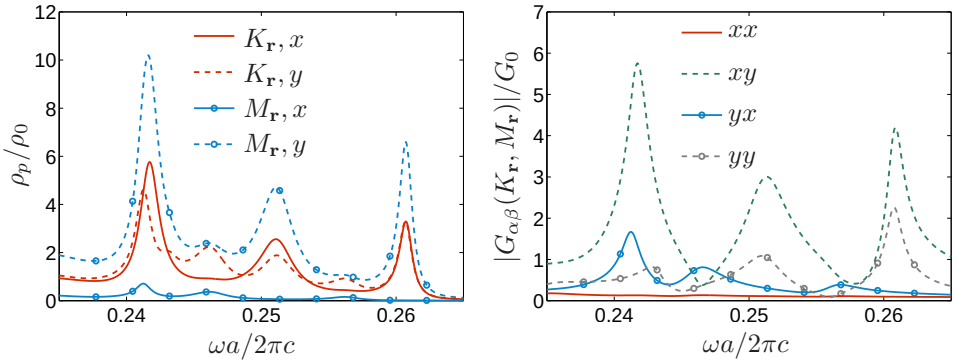

Figure 5.5: Left: Projected LDOS at the two positions $K_\mathbf{r}$ and $M_\mathbf{r}$ with projections along the x or y-directions as indicated. Values are in units of the projected LDOS in the homogeneous material, so that the figure effectively shows the Purcell effect. Right: Absolute values of elements in the propagator between the points $K_\mathbf{r}$ and $M_\mathbf{r}$ in units of $G_0(\omega) = n\omega/(6\pi c)$ corresponding to the imaginary part of the projected Green's tensor in the homogeneous material.

Analysis of mode profiles

There is an interesting overall patterning of the modes in Fig. 5.4 that relates to the field profiles of the Bloch modes and the orientation of the emitter. The Green's tensor may be written in general as a sum over all modes as in Eq. (2.13) and so includes contributions also from radiation modes. The sharp peaks in the LDOS, however, indicate that resonances in the structure that may be associated with modes account for the vast majority of the scattering dynamics in the system at these frequencies.

In Fig. 5.6 we show the real part of the components E_x and E_y of the field from Fig. 5.4 left. At this frequency the modes consist of electric fields that circle the air holes. The modes in Fig. 5.6 are periodic with $\mathbf{E}(\mathbf{r} + 3\mathbf{R}) \approx \mathbf{E}(\mathbf{r})$, where $\mathbf{R}$ is a lattice vector. This is consistent with the fact that the frequency $\omega a/2\pi c = 0.26$ corresponds to the K point in the Brillouin zone for which $|\mathbf{k}| = 2\pi/3a$. The statement is only an approximation since from Fig. 5.4 we realize that there is an overall envelope multiplying onto the fields to account for the finite size of the crystal.

Owing to symmetry, the modes of the system must be six fold degenerate but due to time-reversal symmetry we will limit the analysis to only three. In order to obtain an approximate description of the coupling we now consider the field in the left panel of Fig. 5.6 as one of the three modes at the given frequency. Similarly, the two other modes are each circling a different set of air holes in the crystallite as

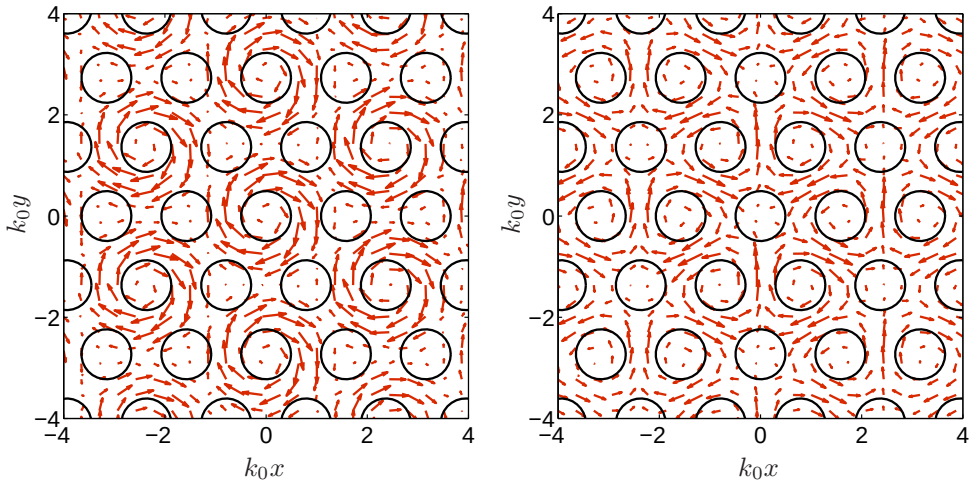

Figure 5.6: Plots of scaled in-plane field vectors for the modes in Fig. 5.4.

illustrated in Fig. 5.7

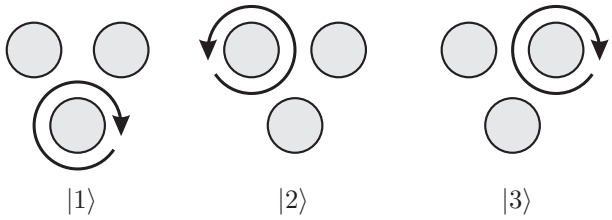

Figure 5.7: Schematic illustration of the three modes in the photonic crystallite each circulating one set of air holes.

We may use the schematic mode profiles in Fig. 5.7 directly to understand how light emitted from a QD at the $K_\mathbf{r}$ point is influenced by QDs at other positions in the crystal, notably the $M_\mathbf{r}$ point. Even though the modes are degenerate due to the symmetry of the crystallite the position and orientation of the emitter breaks this symmetry and allows for controllable coupling to one or more of the modes.

Since the $K_\mathbf{r}$ point is directly between the three air holes, an emitter at this point will in principle couple equally well to all three modes. However, for an x-oriented emitter the modes $|2\rangle$ and $|3\rangle$ interfere destructively, so that only mode $|1\rangle$ is excited. In the example in the left panels of Figs. 5.4 and 5.6, rotating the emitter by $\pi/3$ will result in the mode $|2\rangle$ being excited instead. Similarly, the field in the right panels of Figs. 5.4 and 5.6 may be understood as the sum of the modes $|2\rangle$ and $|3\rangle$. Indeed, a y-oriented emitter at the $K_\mathbf{r}$ point is orthogonal to mode $|1\rangle$

but must couple equally well to modes $|2\rangle$ and $|3\rangle$.

The simple mode description can be used to understand the Green's tensor calculations in Fig. 5.5. Since all three modes are circling the air holes in the crystal, the x-projected LDOS at the $M_{\mathbf{r}}$ point must vanish. Similarly, the y-projected LDOS is enhanced as the sum of the modes $|1\rangle$ and $|2\rangle$. For the non-local coupling, the large value of the xy term in the Green's tensor is understood as coupling through mode $|1\rangle$, and the yy term must stem from modes $|2\rangle$ and $|3\rangle$.

5.3 Additional scattering from quantum dots

Given the Green's tensor for the passive photonic crystal, we can use a Dyson equation approach to self-consistently include additional scattering that arise when QDs are embedded in the structure. The Dyson equation is written in general as

$$\mathbf{G}(\mathbf{r},\mathbf{r}',\omega) = \mathbf{G}^{\mathrm{B}}(\mathbf{r},\mathbf{r}',\omega) + \int \mathbf{G}^{\mathrm{B}}(\mathbf{r},\mathbf{r}'',\omega)\mathbf{U}(\mathbf{r}'',\omega)\mathbf{G}(\mathbf{r}'',\mathbf{r}',\omega)\mathrm{d}\mathbf{r}'',$$

where the integral is over all space and where $\mathbf{U}(\mathbf{r},\omega)$ is a generalized scattering potential, e.g. due to the inclusion of QDs. In particular, $\mathbf{U}(\mathbf{r},\omega)$ may contain both a passive change in permittivity and a dynamic polarizability term due to the excitons. However, in the following we assume that $\mathbf{G}^{\mathrm{B}}(\mathbf{r},\mathbf{r}')$ already contains corrections due to the passive change in permittivity, and we thus consider only the dynamic polarizability. We will return to the question of the passive change in permittivity in section 5.3.1. The excitons are modeled as polarization point sources, and so we will write the potential as

$$\mathbf{U}(\mathbf{r},\omega) = \sum_n \delta(\mathbf{r}-\mathbf{r}_n)\mathbf{e}_{QD}U_n(\omega) = \sum_n \delta(\mathbf{r}-\mathbf{r}_n)\mathbf{U}_n(\omega),$$

where $\delta(\mathbf{r})$ is the Dirac δ-function and $\mathbf{r}_n$ is the position of the n'th QD. This is consistent with Ref. [48] and the discussion in section 2.2.1. In the following we will drop the explicit ω dependence to ease the notation. We now use the Dyson equation along with Eq. (2.44) iteratively to add QDs to the system one at a time and we adopt the convention that $\mathbf{G}^{(N)}$ represents the Green's tensor for the system with N QDs. For the simple case of two QDs in the system we illustrate the method

by calculating the Greens's tensor between points $\mathbf{r}_\mathrm{d}$ and $\mathbf{r}_1$ through the sequence:

$$\begin{aligned}
\mathbf{G}^{(1)}(\mathbf{r}_\mathrm{d},\mathbf{r}_2) &= \mathbf{G}^\mathrm{B}(\mathbf{r}_\mathrm{d},\mathbf{r}_2) + \mathbf{G}^\mathrm{B}(\mathbf{r}_\mathrm{d},\mathbf{r}_1)\mathbf{U}_1\mathbf{G}^{(1)}(\mathbf{r}_1,\mathbf{r}_2) \\
\mathbf{G}^{(1)}(\mathbf{r}_2,\mathbf{r}_2) &= \mathbf{G}^\mathrm{B}(\mathbf{r}_2,\mathbf{r}_2) + \mathbf{G}^\mathrm{B}(\mathbf{r}_2,\mathbf{r}_1)\mathbf{U}_1\mathbf{G}^{(1)}(\mathbf{r}_1,\mathbf{r}_2) \\
\mathbf{G}^{(2)}(\mathbf{r}_2,\mathbf{r}_1) &= \mathbf{G}^{(1)}(\mathbf{r}_2,\mathbf{r}_1) + \mathbf{G}^{(1)}(\mathbf{r}_2,\mathbf{r}_2)\mathbf{U}_2\mathbf{G}^{(2)}(\mathbf{r}_2,\mathbf{r}_1) \\
\Rightarrow \quad \mathbf{e}_2\mathbf{G}^{(2)}(\mathbf{r}_2,\mathbf{r}_1) &= \frac{\mathbf{e}_2\mathbf{G}^{(1)}(\mathbf{r}_2,\mathbf{r}_1)}{1-\mathbf{e}_2\mathbf{G}^{(1)}(\mathbf{r}_2,\mathbf{r}_2)\mathbf{e}_2U_2} \qquad (5.1) \\
\mathbf{G}^{(2)}(\mathbf{r}_\mathrm{d},\mathbf{r}_1) &= \mathbf{G}^{(1)}(\mathbf{r}_\mathrm{d},\mathbf{r}_1) + \mathbf{G}^{(1)}(\mathbf{r}_\mathrm{d},\mathbf{r}_2)\mathbf{U}_2\mathbf{G}^{(2)}(\mathbf{r}_2,\mathbf{r}_1). \qquad (5.2)
\end{aligned}$$

Comparing Eqs. (2.44) and (5.2), we can immediately interpret the additional term as arising due to the light scattering off QD 2 before arriving at $\mathbf{r}_\mathrm{d}$ as illustrated in Fig. 5.8.

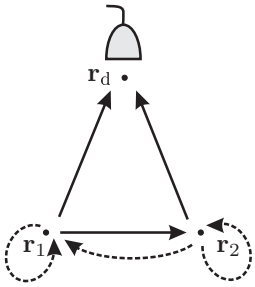

Figure 5.8: Sketch of different scattering channels in a system with two QDs. The solid lines correspond to the two different paths evident in Eq. (5.2), whereas the dashed lines correspond to additional dressing of the Green's tensor due to multiple scattering among the two QDs.

From the denominator in Eq. (5.1), we note that $\mathbf{G}^{(2)}(\mathbf{r}_2,\mathbf{r}_1)$ includes the self interaction due to multiple scattering off QD 2. Eq. (5.1) is equivalent to Eq. (2.44), only now with the one QD Green's tensor in place of the background Green's tensor. By substituting $\mathbf{r}_\mathrm{d}$ for $\mathbf{r}_1$ in Eq. (5.1) and interchanging the spatial positions (using the general relation $\mathbf{e}_n\mathbf{G}(\mathbf{r}_n,\mathbf{r}) = \mathbf{G}(\mathbf{r},\mathbf{r}_n)\mathbf{e}_n$) we have

$$\mathbf{G}^{(2)}(\mathbf{r}_\mathrm{d},\mathbf{r}_2)\mathbf{e}_2 = \frac{\mathbf{G}^{(1)}(\mathbf{r}_\mathrm{d},\mathbf{r}_2)\mathbf{e}_2}{1-\mathbf{e}_n\mathbf{G}^{(1)}(\mathbf{r}_2,\mathbf{r}_2)\mathbf{e}_2U_2}, \qquad (5.3)$$

which gives the coupling from QD 2 to the detector when there is another QD present. Although it is not immediately obvious, one can show that Eqs. (5.2) and (5.3) are identical under the interchange of QD 1 and QD 2 - as they should be, of course, as it should not matter in which order the QDs are added to the system. In addition, we note that Eq. (5.2) may be rewritten in the form of Eq. (47) in Ref.

[48]. Although we have illustrated the method in the case of two QDs, the method obviously works for any number of QDs.

The direct application of the Dyson equation is compromised whenever $\mathbf{r}$ is inside the source volume (that is, whenever $\mathbf{r} = \mathbf{r}_n$) due to the divergence in the real part of the background Green's tensor. Formally, this is also the case in the calculations leading to Eq. (5.1). The above discussion, however, suggests that the procedure is really self-consistent and one can arrive at Eq. (5.1) directly from Eq. (2.44) by simply using $\mathbf{G}^{(1)}(\mathbf{r}, \mathbf{r}')$ as the background Green's tensor. This further illustrates that the method is consistent with Ref. [48].

5.3.1 Local field corrections using a Coupled Dipole Approximation approach

In the calculations above, we assumed that $\mathbf{G}(\mathbf{r}, \mathbf{r}')$ includes already the additional scattering due to a passive change in permittivity from the QDs. Although the QDs are tiny compared with the typical length scales in electromagnetic scattering calculations this is not a priori justified. In the following we will analyze scattering from the passive QDs in the framework of the CDA as formulated in Ref. [55].

An introductory example

As an introduction, we consider the calculation of the electric field at point $\mathbf{r}$ in a material system with a scattering object in the form of a small (passive) homogeneous lump of semiconductor material at the position $\mathbf{r}_{\mathrm{QD}}$ as sketched in Fig. 5.9.

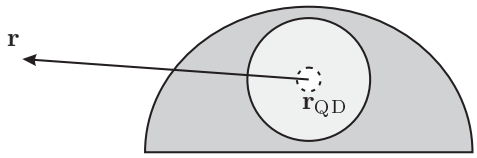

Figure 5.9: Sketch of the geometry for calculations of local field corrections for a self-assembled QD.

Following the iterative scheme of Ref. [55] we first solve for the electric field at the location of the QD. The Lippmann-Schwinger equation reads

$$\mathbf{E}(\mathbf{r}_{\mathrm{QD}}) = \mathbf{E}^0(\mathbf{r}_{\mathrm{QD}}) + k_0^2 \Delta\epsilon \lim_{\delta \to 0} \int_{V_{\mathrm{QD}} - \delta V} \mathbf{G}^{\mathrm{B}}(\mathbf{r}_{\mathrm{QD}}, \mathbf{r}') \mathbf{E}(\mathbf{r}') \mathrm{d}\mathbf{r}' - \mathbf{L} \frac{\Delta\epsilon}{\epsilon_{\mathrm{B}}} \mathbf{E}(\mathbf{r}_{\mathrm{QD}}), \tag{5.4}$$

where V_{QD} denotes the QD volume with an exclusion volume δV centered on $\mathbf{r}' = \mathbf{r}_{\mathrm{QD}}$ and $\Delta\epsilon = \epsilon_{\mathrm{QD}} - \epsilon_{\mathrm{B}}$. In the dipole approximation the electric field varies little over the extend of the QD. Hence we evaluate it at $\mathbf{r}' = \mathbf{r}_{\mathrm{QD}}$ and rearrange the terms to get the explicit expression

$$\mathbf{E}(\mathbf{r}_{\mathrm{QD}}) = \left(1 - k_0^2 \Delta\epsilon \mathbf{M} + \mathbf{L}\frac{\Delta\epsilon}{\epsilon_{\mathrm{B}}}\right)^{-1} \mathbf{E}^0(\mathbf{r}_{\mathrm{QD}}) \tag{5.5}$$

where

$$\mathbf{M} = \lim_{\delta \to 0} \int_{V_{\mathrm{QD}} - \delta V} \mathbf{G}^{\mathrm{B}}(\mathbf{r}_{\mathrm{QD}}, \mathbf{r}') \mathrm{d}\mathbf{r}'.$$

Using the expression for $\mathbf{E}(\mathbf{r}_{\mathrm{QD}})$ the electric field at the point $\mathbf{r}$ can be directly calculated from the Lippmann-Schwinger equation:

$$\mathbf{E}(\mathbf{r}) = \mathbf{E}^0(\mathbf{r}) + k_0^2 \Delta\epsilon \int_{V_{\mathrm{QD}}} \mathbf{G}^{\mathrm{B}}(\mathbf{r}, \mathbf{r}') \mathbf{E}(\mathbf{r}') \mathrm{d}\mathbf{r}'.$$

Since the observation point is outside the QD the Green's tensor is bounded and there is no need for an exclusion volume. Working in the dipole approximation we evaluate both the Green's tensor and the electric field at $\mathbf{r}' = \mathbf{r}_{\mathrm{QD}}$ to arrive at the expression for the electric field:

$$\begin{aligned}\mathbf{E}(\mathbf{r}) &= \mathbf{E}^0(\mathbf{r}) + k_0^2 \Delta\epsilon V_{\mathrm{QD}} \mathbf{G}^{\mathrm{B}}(\mathbf{r}, \mathbf{r}_{\mathrm{QD}}) \mathbf{E}(\mathbf{r}_{\mathrm{QD}}) \\ &= \mathbf{E}^0(\mathbf{r}) + k_0^2 \Delta\epsilon V_{\mathrm{QD}} \mathbf{G}^{\mathrm{B}}(\mathbf{r}, \mathbf{r}_{\mathrm{QD}}) \left(1 - k_0^2 \Delta\epsilon \mathbf{M} + \mathbf{L}\frac{\Delta\epsilon}{\epsilon_{\mathrm{B}}}\right)^{-1} \mathbf{E}^0(\mathbf{r}_{\mathrm{QD}}). \end{aligned} \tag{5.6}$$

The value of $\mathbf{M}$ is dependent on the shape of the QD as well as the shape of the infinitesimal exclusion volume. The latter dependence, however, is precisely balanced by the $\mathbf{L}$ term in such a way that the right hand side of the Lippmann-Schwinger equation is independent of the shape of the exclusion volume [59]. For a spherical QD of radius R it is convenient to choose also a spherical exclusion volume in which case

$$\mathbf{M} = \frac{2}{3k_{\mathrm{B}}^2} \left((1 - ik_{\mathrm{B}}R)e^{ik_{\mathrm{B}}R} - 1\right) \mathbf{I}, \tag{5.7}$$

where $k_{\mathrm{B}}^2 = k_0^2 \epsilon_{\mathrm{B}}$ as stated in Ref. [55]. For typical QDs we have $R \approx 10\,\mathrm{nm}$ and $k_{\mathrm{B}} = k_{\mathrm{B}}\Omega_x/c \approx 10^7\,\mathrm{m}^{-1}$ giving $k_{\mathrm{B}}R \approx 1/10$. In this case we have

$$|k_0^2 \Delta\epsilon M_{\alpha\alpha}| \approx 0.003 \frac{\Delta\epsilon}{\epsilon_{\mathrm{B}}}, \quad \alpha \in \{x, y, z\},$$

which is two orders of magnitude smaller than the terms $L_{\alpha\alpha}\Delta\epsilon/\epsilon_{\mathrm{B}}$ due to the spherical exclusion volume, cf. section 2.2.2. Due to the diagonal forms of both $\mathbf{M}$

and $\mathbf{L}$ Eq. (5.6) is written more compactly as

$$\mathbf{E}(\mathbf{r}) = \mathbf{E}^0(\mathbf{r}) + \frac{k_0^2 \Delta\epsilon V_{\mathrm{QD}} \mathbf{G}^{\mathrm{B}}(\mathbf{r}, \mathbf{r}_{\mathrm{QD}})}{1 - k_0^2 \Delta\epsilon M_{\alpha\alpha} + L_{\alpha\alpha} \frac{\Delta\epsilon}{\epsilon_{\mathrm{B}}}} \mathbf{E}^0(\mathbf{r}_{\mathrm{QD}}). \tag{5.8}$$

It is illustrative to arrive at this result also using the Dyson equation. In order to properly handle the divergence in the background Green's tensor in the limit $\mathbf{r} = \mathbf{r}_{\mathrm{QD}}$, we write the equation as

$$\begin{aligned} \mathbf{G}(\mathbf{r}_{\mathrm{QD}}, \mathbf{r}) = \mathbf{G}^{\mathrm{B}}(\mathbf{r}_{\mathrm{QD}}, \mathbf{r}) + k_0^2 \Delta\epsilon \lim_{\delta \to 0} \int_{V_{\mathrm{QD}} - \delta V} \mathbf{G}^{\mathrm{B}}(\mathbf{r}_{\mathrm{QD}}, \mathbf{r}') \mathbf{G}(\mathbf{r}', \mathbf{r}) \mathrm{d}\mathbf{r}' \\ - \mathbf{L} \frac{\Delta\epsilon}{\epsilon_{\mathrm{B}}} \mathbf{G}(\mathbf{r}_{\mathrm{QD}}, \mathbf{r}), \end{aligned} \tag{5.9}$$

where the integration is over the QD volume except for an infinitesimal exclusion volume centered on $\mathbf{r}' = \mathbf{r}_{\mathrm{QD}}$. The Green's tensor $\mathbf{G}(\mathbf{r}', \mathbf{r})$ varies little over the extend of the QD, and in the dipole approximation we evaluate it at $\mathbf{r}' = \mathbf{r}_{\mathrm{QD}}$ to arrive at the expression for the Green's tensor

$$\mathbf{G}(\mathbf{r}_{\mathrm{QD}}, \mathbf{r}) = \frac{\mathbf{G}^{\mathrm{B}}(\mathbf{r}_{\mathrm{QD}}, \mathbf{r})}{1 - k_0^2 \Delta\epsilon M_{\alpha\alpha} + L_{\alpha\alpha} \frac{\Delta\epsilon}{\epsilon_{\mathrm{B}}}}. \tag{5.10}$$

Given the Green's tensor for the scattering structure including the QD, the electric field at point $\mathbf{r}$ is calculated through the explicit equation [55]

$$\mathbf{E}(\mathbf{r}) = \mathbf{E}^0(\mathbf{r}) + k_0^2 \Delta\epsilon \int_{V_{\mathrm{QD}}} \mathbf{G}(\mathbf{r}, \mathbf{r}') \mathbf{E}^0(\mathbf{r}') \mathrm{d}\mathbf{r}',$$

where, in the dipole approximation, we evaluate the integrand at $\mathbf{r}' = \mathbf{r}_{\mathrm{QD}}$ and pull it outside the integral to arrive at Eq. (5.8).

The analysis illustrates how the Dyson equation in the form of Eq. (5.9) is the counterpart to the Lippmann-Schwinger equation. This is not surprising, since we may interpret the columns of the Green's tensor $\mathbf{G}(\mathbf{r}, \mathbf{r}')$ as the electric field at the point $\mathbf{r}$ due to a point source at the point $\mathbf{r}'$. In Eq. (5.9) we interchanged the arguments of the Green's tensor in order to make the equation for each of the columns of the Green's tensor match the form of Eq. (5.4). This was done in order to use the prescription of Yaghjian [59] for the evaluation of the integral.

The dipole approximation is crucial for the above derivations because it allows us to evaluate most of the integrands at $\mathbf{r}' = \mathbf{r}_{\mathrm{QD}}$. This means that we effectively work in a real cavity model in which the Green's tensor is evaluated at the point in the center of the QD (or any other point inside the QD). Due to the divergence in the background Green's tensor this does not vary slowly across the QD, and so we have to keep it giving rise to the $\mathbf{M}$ and $\mathbf{L}$ terms in Eqs. (5.8) and (5.10).

As discussed above, the shape of the exclusion volume does not play a role since it is balanced by the $\mathbf{M}$ term. Obviously, if we neglect the $\mathbf{M}$ term the shape of the principal volume does matter. In this case the spherical exclusion volume is most reasonable since for any QD with 3 finite dimensions we can perform the $\mathbf{M}$ term integral in two steps. First, we integrate to a sphere of dimension R_{I} that is fully contained in the volume of the QD as illustrated in Fig. 5.9. This results in a term similar to Eq. (5.7) but with R exchanged for R_{I}. Next, we integrate the background Green's tensor over the remaining part of the QD. This integral has no divergence and hence can be evaluated to arbitrary accuracy. Since the $\mathbf{M}$ term with spherical exclusion volume is small for a spherical QD it is likely to be small for any shape of QD as long as the sizes are comparable.

Application and discussion

Based on the introductory example, we now use the Dyson equation to investigate the effect of scattering due to the inclusion of the QDs themselves. We start by considering the case $\mathbf{r}_{\mathrm{QD}} = \mathbf{r}_1$ entering the self interactions in Eq. (2.44). Substituting into Eq. (5.10) we get

$$\mathbf{G}_1^{\mathrm{B}}(\mathbf{r}_1, \mathbf{r}) = \frac{\mathbf{G}_0^{\mathrm{B}}(\mathbf{r}_1, \mathbf{r})}{1 + \frac{1}{3}\frac{\Delta\epsilon}{\epsilon_{\mathrm{B}}}} = \frac{3\epsilon_{\mathrm{B}}}{2\epsilon_{\mathrm{B}} + \epsilon_{\mathrm{QD}}}\mathbf{G}_0^{\mathrm{B}}(\mathbf{r}_1, \mathbf{r}), \tag{5.11}$$

where we have ignored the small contribution due to the $\mathbf{M}$ term and we have adopted the notation convention that $\mathbf{G}_N^{\mathrm{B}}(\mathbf{r}, \mathbf{r}')$ denotes the Green's tensor for the system including the passive scattering from N dots. Eq. (5.11) is consistent with the calculations of the Green's tensor of a small particle in the limit of zero radius [125].

In the case of observation points that do not coincide with any QD, the Dyson equation along with Eq. (5.11) can be used to calculate $\mathbf{G}_1^{\mathrm{B}}(\mathbf{r}, \mathbf{r}')$ as

$$\begin{aligned}\mathbf{G}_1^{\mathrm{B}}(\mathbf{r}, \mathbf{r}') &= \mathbf{G}_0^{\mathrm{B}}(\mathbf{r}, \mathbf{r}') + \mathbf{G}_0^{\mathrm{B}}(\mathbf{r}, \mathbf{r}_1) k_0^2 \Delta\epsilon_{\mathrm{QD}} V_{\mathrm{QD}} \mathbf{G}_1^{\mathrm{B}}(\mathbf{r}_1, \mathbf{r}') \\ &= \mathbf{G}_0^{\mathrm{B}}(\mathbf{r}, \mathbf{r}') + \mathbf{G}_0^{\mathrm{B}}(\mathbf{r}, \mathbf{r}_1) k_0^2 \Delta\epsilon_{\mathrm{QD}} V_{\mathrm{QD}} \frac{3\epsilon_{\mathrm{B}}}{2\epsilon_{\mathrm{B}} + \epsilon_{\mathrm{QD}}} \mathbf{G}_0^{\mathrm{B}}(\mathbf{r}_1, \mathbf{r}'),\end{aligned} \tag{5.12}$$

where V_{QD} denotes the volume of the QD. In the limit of vanishing QD volumes we recover $\mathbf{G}_1^{\mathrm{B}}(\mathbf{r}, \mathbf{r}') = \mathbf{G}_0^{\mathrm{B}}(\mathbf{r}, \mathbf{r}')$ indicating that in this approximation the background Green's tensor is unaltered by the inclusion of the QDs unless any (or both) of the observation points coincide with a QD.

Using the above procedure, we can now add an additional QD to the system as

$$\mathbf{G}_2^{\mathrm{B}}(\mathbf{r}_2, \mathbf{r}) = \frac{3\epsilon_{\mathrm{B}}}{2\epsilon_{\mathrm{B}} + \epsilon_{\mathrm{QD}}}\mathbf{G}_1^{\mathrm{B}}(\mathbf{r}_2, \mathbf{r}) = \begin{cases} \frac{3\epsilon_{\mathrm{B}}}{2\epsilon_{\mathrm{B}} + \epsilon_{\mathrm{QD}}}\mathbf{G}_0^{\mathrm{B}}(\mathbf{r}_2, \mathbf{r}) & \mathbf{r} \neq \mathbf{r}_1 \\ \left(\frac{3\epsilon_{\mathrm{B}}}{2\epsilon_{\mathrm{B}} + \epsilon_{\mathrm{QD}}}\right)^2 \mathbf{G}_0^{\mathrm{B}}(\mathbf{r}_2, \mathbf{r}_1) & \mathbf{r} = \mathbf{r}_1, \end{cases}$$

where we have implicitly assumed that the permittivity of the two QDs are the same.

The above analysis derives directly from the Dyson equation in the dipole approximation after dropping the $\mathbf{M}$ terms. In the case of $\mathbf{r} \neq \mathbf{r}_1$, the above expression for $\mathbf{G}_2^{\mathrm{B}}(\mathbf{r}_2, \mathbf{r})$ is consistent with Refs. [126, 127].

The rate of spontaneous emission from a point source is proportional to the imaginary part of $\mathbf{G}^{\mathrm{B}}(\mathbf{r}_1, \mathbf{r}_1)$, but in this limit we can no longer directly apply the prescription of Yaghjian for the evaluation of the scattering integral. Nevertheless, if we set $\mathbf{r} = \mathbf{r}_2$ in the above expression for $\mathbf{G}_2^{B}(\mathbf{r}_2, \mathbf{r})$ the rate of decay as obtained from Eq. (2.44) is consistent with the Glauber-Lewenstein real-cavity model for the local-field correction factor to the rate of spontaneous decay [128, 129]. This is not surprising, since the dipole approximation dictates that the Green's tensor be evaluated at the center of the QD, as discussed above, and hence a real cavity model is really implicit in this simple theory.

The above analysis and discussion suggests that our method is of use in the evaluation of additional scattering contributions to the Green's tensor for $\mathbf{r} \neq \mathbf{r}'$, whereas it is not entirely justified that we can apply it to the local problem $\mathbf{r} = \mathbf{r}'$. However, the small refractive index contrast between the InAs QDs and the GaAs background material means that local field corrections are negligible and we will ignore them in this work. For calculations on other material systems, however, local field effects may be of importance. In this case the simple procedure outlined in this section may be of value.

5.4 Decay dynamics

In this section we use the numerical calculations of the Green's tensor from section 5.2 as a basis for the general Dyson equation approach of section 5.3. We consider the decay dynamics of a QD at the point $\mathbf{r}_1 = K_{\mathbf{r}}$ within the PC slab in Fig. 5.1 with $L = 6a$. We shall refer to this as QD 1. From the analysis of section 5.2.2, especially Fig. 5.4, we expect that the QD will couple to other QDs in the crystal, and we therefore place an additional QD (QD 2) at the point $\mathbf{r}_2 = M_{\mathbf{r}}$.

For the analysis we work in an all light picture where we solve for the expectation value of the electric field intensity operator at the detector position $\mathbf{r}_{\mathrm{d}} = (0, 0, 3.3a)$ above the Γ point and outside the membrane. From the discussion in section 2.4.4, the solution to the equations of motion in the frequency domain is given as

$$\mathbf{E}(\mathbf{r}_{\mathrm{d}}, \omega) = \mathbf{G}^{(2)}(\mathbf{r}_{\mathrm{d}}, \mathbf{r}_1, \omega)\mathbf{S}_1(\omega), \tag{5.13}$$

where, comparing to Eq. (2.44), we have replaced $\mathbf{G}^{(1)}(\mathbf{r}_{\mathrm{d}}, \mathbf{r}_1)$ with $\mathbf{G}^{(2)}(\mathbf{r}_{\mathrm{d}}, \mathbf{r}_1)$ as given in Eq. (5.2) to account for the extra scattering off QD 2.

As discussed in section 5.3, the Green's tensor may be interpreted as consisting of a direct term and a scattering term. The direct term depends on the LDOS at $K_\mathbf{r}$ as well as the propagator from this point to the detector. The scattering term, on the other hand, depends on the LDOS at both $K_\mathbf{r}$ and $M_\mathbf{r}$ as well as the propagator between the two positions and the propagator from $M_\mathbf{r}$ to the detector. Fig. 5.10 shows the magnitude of the propagators from the QD positions to the detector as a function of frequency. The curves are somewhat monotonous and do not reflect the resonances of the modes of the photonic crystallite. We note that the off-diagonal elements of the propagators vanish, so that the polarization of the light at the detector position reflects the orientation of the emitter at either of the two points.

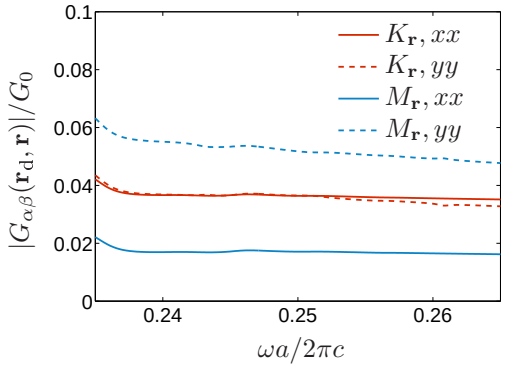

Propagators at $\omega a/2\pi c = 0.26$	
$\mathrm{IM}\{G_{yy}(\mathbf{r}_1,\mathbf{r}_1)\}$	3.29
$\mathrm{IM}\{G_{yy}(\mathbf{r}_2,\mathbf{r}_2)\}$	6.60
$G_{yy}(\mathbf{r}_1,\mathbf{r}_2)$	$0.32 - 2.23i$
$G_{yy}(\mathbf{r}_\mathrm{d},\mathbf{r}_1)$	$0.03 + 0.01i$
$G_{yy}(\mathbf{r}_\mathrm{d},\mathbf{r}_2)$	$0.05 + 0.02i$
$G_{xy}(\mathbf{r}_1,\mathbf{r}_2)$	$0.86 - 3.94i$

Figure 5.10: Left: Absolute values of the propagators between the detector at the position $\mathbf{r}_d = (0, 0, 3.3a)$ (outside the slab above the Γ point) and the points $\mathbf{r}_1$ and $\mathbf{r}_2$. Both the G_{xx} and the G_{yy} elements are shown. The xy components are vanishingly small and are not shown. Right: Explicit values of the propagators of interest for the calculation at $\omega = \omega_1$. All propagators are in units of $G_0(\omega) = n\omega/(6\pi c)$, corresponding to the imaginary part of the projected Green's tensor in the homogeneous material.

The two QDs are assumed to have nearly identical resonance frequencies, so that $\omega_2 = \omega_1 + \Delta\omega$, where $\omega_1 = 1.65{\times}10^{15}\,\mathrm{s}^{-1}$ is the resonance frequency of QD 1. The frequency is chosen so that $\omega_1 a/2\pi c = 0.26$, corresponding to peak 3 in Fig. 5.3. In addition, we consider the QDs to have dipole moments of equal magnitude

$$d_1 = d_2 = 1.00 \times 10^{-28}\,\mathrm{C\,m},$$

which is consistent with Ref. [5].

5.4.1 Decay dynamics in the time-domain

We consider the experimental condition in which QD 1 is excited at $t = 0$ and decays under the emission of a single photon. The initial condition is thus $|\Psi(t = 0)\rangle = b_1^\dagger(0)|\mathcal{F}\rangle$. The time dependent dynamics of the coupled QDs may be obtained from the inverse Fourier transform of the spectrum, Eq. (5.13). Appendix G discusses the inverse transform in detail. Note, that although the propagators show rich behavior as a function of frequency they may be considered slowly varying within the bandwidth associated with the decay dynamics. Indeed, a decay time of 1 ns corresponds to a bandwidth of $\Delta\omega_{\mathrm{BW}} = 10^9\,\mathrm{s}^{-1}$ which, in the scaled frequencies, corresponds to $\Delta\omega_{\mathrm{BW}}a/2\pi c = 1.5 \times 10^{-7}$. Therefore, the pole approximation is valid for the evaluation of the transforms in accordance with the Wigner-Weisskopf approximation in sections 2.4.3 and 4.2.3. The electric field operator at the position of the detector is given as the sum of a direct term and a scattering term as

$$\mathbf{E}(\mathbf{r}_{\mathrm{d}}, t) = \mathbf{E}^{\mathrm{D}}(\mathbf{r}_{\mathrm{d}}, t) + \mathbf{E}^{\mathrm{S}}(\mathbf{r}_{\mathrm{d}}, t),$$

in which the scattering term itself consists of two terms; one term, $\mathbf{E}_2^{\mathrm{S}}$, that scatters off QD 2 before arriving at the detector and another term, $\mathbf{E}_{21}^{\mathrm{S}}$, that first scatters off QD 2 and then back to QD 1 before arriving at the detector. In order to illustrate the role of the electromagnetic propagator we first consider the case where both QDs are polarized in the y-direction and secondly the case where QD 1 is polarized in the x direction and QD 2 is polarized in the y-direction.

Two emitters with the same polarization

Both QDs have equal dipole moments pointing in the y-direction. The relevant electromagnetic propagators are shown in Figs. 5.5 and 5.10. Fig. 5.11 shows the time dependent expectation value of the intensity operator at the detector position,

$$\langle I(\mathbf{r}_{\mathrm{d}}, t)\rangle = \left\langle \mathbf{E}^+(\mathbf{r}_{\mathrm{d}}, t) \cdot \mathbf{E}^-(\mathbf{r}_{\mathrm{d}}, t)\right\rangle,$$

where $\mathbf{E}^+(\mathbf{r}_{\mathrm{d}}, t)$ and $\mathbf{E}^-(\mathbf{r}_{\mathrm{d}}, t)$ are positive and negative frequency parts of the field, respectively, as discussed in Appendix G. For reference, we also show the intensity expectation value in the case of QD 1 only.

The influence of QD 2 changes qualitatively the decay of QD 1 as measured through the intensity at the detector position. The change in the emission process can be interpreted as the result of absorption and reemission at QD 2 (for the $\mathbf{E}_2^{\mathrm{S}}$ term) and at both QD 2 and then at QD1 (the $\mathbf{E}_{21}^{\mathrm{S}}$ term) of the light that is originally emitted at QD 1. The process is a genuine coherent quantum mechanical phenomenon in which only a single photon is emitted. In particular, the interference at the detector is the interference of the photon with itself.

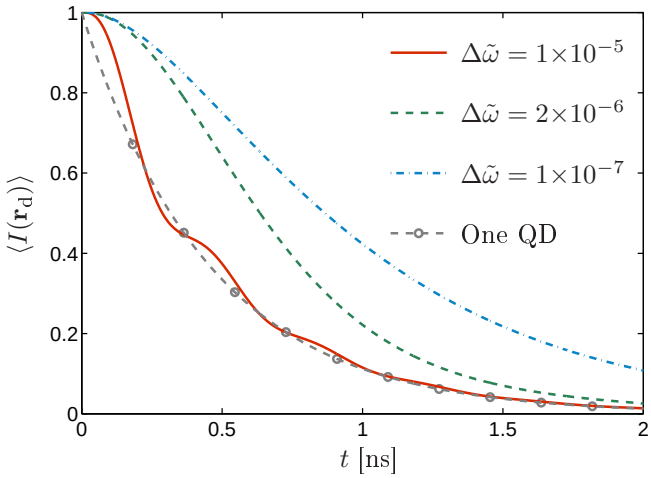

Figure 5.11: Intensity at the position $\mathbf{r}_d$ of the light emitted from QD 1 at position $K_\mathbf{r}$ with a second QD at the position $M_\mathbf{r}$ with relative detuning $\Delta\tilde{\omega} = \Delta\omega/\omega_1$ as indicated (red, green and blue lines). For reference, we show also the case of a single QD only (gray dashed line). The intensity is normalized to the intensity of the single QD case at $t = 0$.

In order to illustrate the effect of the additional terms due to QD 2, we show in Fig. 5.12, for each of the three detunings the spectra belonging to the three scattering channels. The spectra are given as

$$S(\omega) = \langle \mathbf{E}^-(-\omega)\cdot\mathbf{E}^+(\omega)\rangle = \langle (\mathbf{E}^+(\omega))^\dagger\cdot\mathbf{E}^+(\omega)\rangle,$$

and we have normalized them simply to the maximum value of the spectrum in the single QD case. Although not directly observable in practice, we show the spectra belonging to each of the three scattering channels individually, as this allows a better understanding of the influence of each of the three terms. In addition to the spectra, we show also the corresponding time domain dynamics. For each of the three channels, we plot the absolute square of the electric field at the detector position. For the largest detuning $\Delta\tilde{\omega} = 10^{-5}$ we have multiplied the spectra and the intensities related to the two scattering channels by a factor of 60 in order to make them visible in the figures. At this detuning the splitting of the spectrum is visible as is the resulting decaying oscillations. The frequency of the oscillations is related to the difference in resonance frequency of the two QDs - for small differences in the resonance frequencies the frequency of the oscillations increases, and eventually the time-dependence of the term $\mathbf{E}_2^\mathrm{S}$ becomes linear in t, cf. Eq. (G.5). Consequently, the time-dependence of $|\mathbf{E}_2^\mathrm{S}(\mathbf{r}_\mathrm{d}, t)|^2$ becomes quadratic for small times and increases

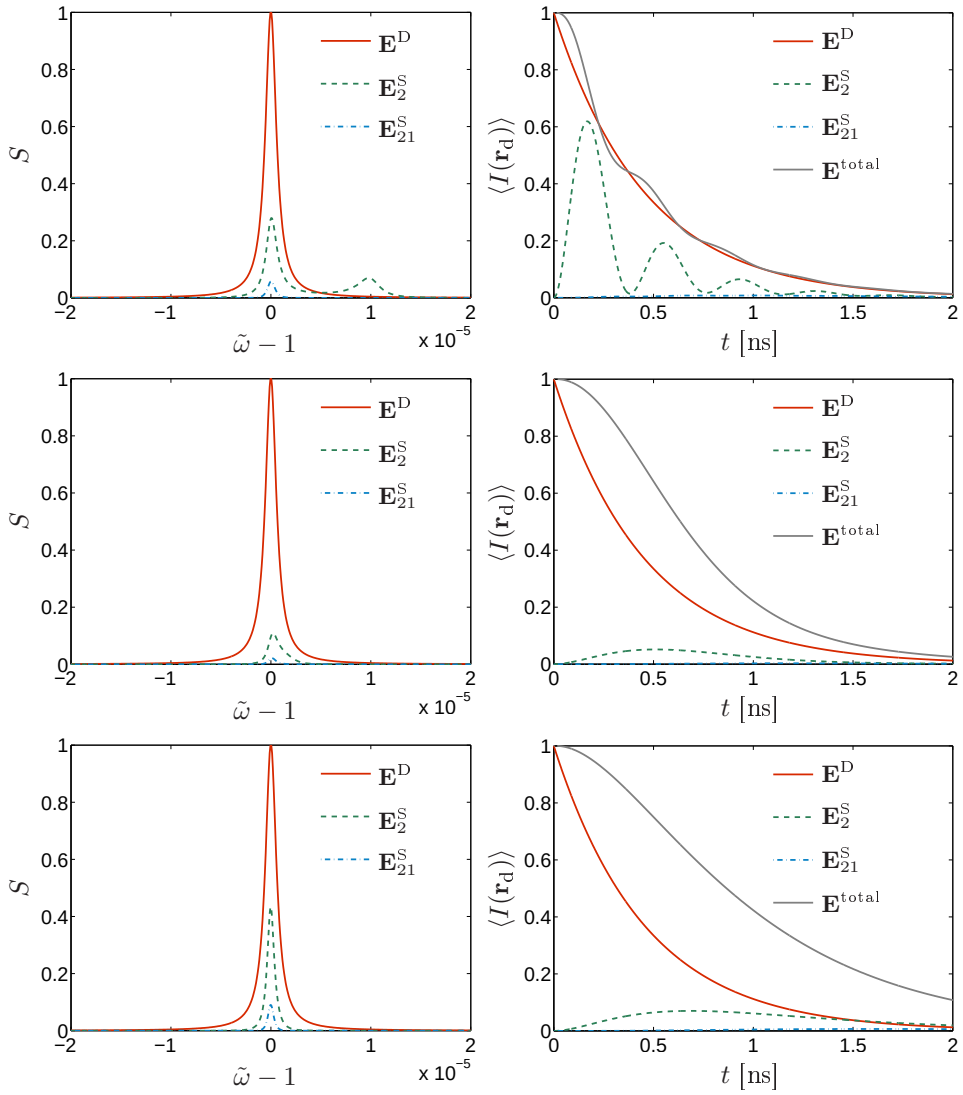

Figure 5.12: Spectra (left) and decay curves (right) corresponding to the three different decay channels in the two QD case: the direct term $\mathbf{E}^D$ (red solid lines) and the scattering terms $\mathbf{E}_2^S$ (green dashed line) and $\mathbf{E}_{21}^S$ (blue dashed-dotted line). Results are shown for the three different detunings $\Delta\tilde{\omega} = 10^{-5}$ (top), $\Delta\tilde{\omega} = 2\times10^{-6}$ (center), $\Delta\tilde{\omega} = 10^{-7}$ (bottom), where $\tilde{\omega} = \omega/\omega_1$. The curves corresponding to the scattering channels have been multiplied by 60 for the case of $\Delta\tilde{\omega} = 10^{-5}$. In addition, the full decay curves are shown in gray. These are identical to the curves in Fig. 5.11.

until eventually the decaying exponential factor takes over. The relatively small difference in resonance frequencies is the reason that no oscillations are visible in the $\mathbf{E}_2^{\mathrm{S}}$ terms for the two smaller detunings.

Emitters with orthogonal polarization

We now change the system by rotating the dipole moment of QD 1 to the x-direction. In addition, a polarization filter is introduced so that only y-polarized light is observed at the detector. Since the off-diagonal elements of the propagators out of the slab are vanishing, the only way the x-polarized QD 1 can emit y-polarized light above the slab is by scattering off QD 2.

Fig. 5.13 shows the intensity of y-polarized light at the detector position as a function of time. There is no direct coupling from QD 1 to the detector and the intensity expectation value is qualitatively different from that of the y-polarized emitter due to the process of absorption and reemission from QD 2. Effectively, only the scattering term $\mathbf{E}_2^{\mathrm{S}}$ is non-vanishing, and comparing to Fig. 5.12 we recognize a clear similarity although the scattering term is much larger in this case. The larger coupling between the orthogonal dipoles may be directly understood from the in-plane field vectors in Fig. 5.6 in which the electric field lines circle the central air hole, thus favoring the orthogonal emitters.

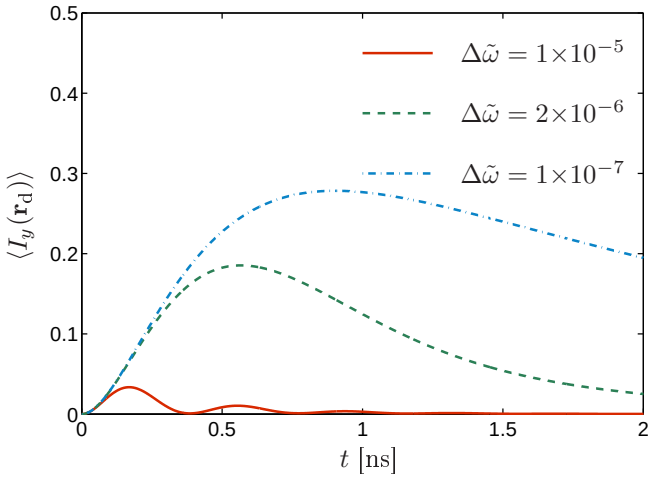

Figure 5.13: Intensity of y-polarized light at the position $\mathbf{r}_d$ emitted from QD 1 at position $K_\mathbf{r}$ with dipole moment in the x-direction. The intensity is normalized as in Fig. 5.11.

5.5 Conclusion

We have investigated multiple QD decay dynamics in photonic crystal slabs. Working in an all light picture, the analysis has illustrated how QDs, in addition to sources of light, may act as resonant scatterers for light within the crystal.

As an example material system we have focused on PC slabs. Calculation of the Green's tensor for passive PC slabs was handled with FDTD to provide both local and non-local Green's tensors as a function of frequency at specific locations in the crystal. Based on the band structure as well as spatial fourier analysis, scattering properties of the crystal was shown to be related to pseudo modes or resonances due to the finite size of the crystallite.

The additional scattering due to QDs in the PC may be included in a Green's tensor description of the PC. We have described a self-consistent Dyson equation approach which allows for inclusion of QDs in the model in an intuitive and physically appealing way. The model allows for a direct interpretation in terms of different scattering channels by which light emitted at one QD may travel to the detector either directly or by scattering off other QDs. It is similar to the use of the CDA for scattering calculations, and we have discussed how some insight into local field corrections can be gained from this simple model.

Based on the numerical Green's tensor calculations a model system consisting of two QDs inside the PC slab was constructed using the self-consistent Dyson equation approach. The scattering properties of the QDs were shown to have a profound effect on the expectation value of the electric field intensity operators at the detector position outside the crystal. The effect may be interpreted as resonant excitation and subsequent emission at one QD of the light that was originally emitted from the other QD. By deliberate coupling of the two QDs through the modes of the PC slab it was illustrated how this effect may be exploited to emit light of opposite polarization than that of the emitter.

The method that we have presented is perfectly general and is based only on the Green's tensor of the passive background material. We have illustrated the method with the example of two QDs, but the simple form of the Dyson equation approach allows for an easy extension of the method to many QDs. The resonant scattering of light off other QDs in the sample is likely to be important in experiments aiming at measuring properties of single QDs, since it could influence the measured light in an uncontrolled way. On the other hand, it offers additional possibilities in terms of light propagation control that may be of interest in applications.

Chapter 6

Conclusion

Steady improvements in quality and control of PCs and QDs have resulted in a number of beautiful solid state quantum optics experiments. Many of these explore effects that may be of practical importance also outside of the laboratory.

The design and development of future optical components rely heavily on adequate descriptions of light propagation in micro and nanostructured environments. Although the governing differential equations have been known for over a century, analytical solutions are available only for a limited number of highly symmetrical problems. Therefore, in most cases of practical interest, numerical methods are employed. Ideally, the numerical method should be accurate enough to capture all relevant physics and allow for understanding the different scattering channels; yet it should be fast enough to ensure acceptable runtimes for practically relevant structures.

During the work in this PhD project we have developed a new method for the solution of the Lippmann-Schwinger integral equation for use in electric field scattering calculations. The method is a hybrid between the well established Rayleigh multipole methods and so-called method of moments calculations. The combination of the two approaches allows for a very fast convergence in terms of number of basis functions while at the same time allowing calculations with scatterers of arbitrary shape and non-homogeneous background. We have formulated the method in the general case, and we have given details and examples of the implementation in two dimensions. The method is not limited to micro- and nanophotonic structures and may well find applications in other areas of electromagnetic scattering calculations.

Central to the work in this project has been spontaneous emission of light from QDs. We have discussed how variations in the LDOS may lead to the suppression or enhancement of the rate of spontaneous emission, and how even the qualitative

behavior of the decay dynamics may be changed. In particular, if an emitter is tuned very close to the sharp edge of the band gap of a photonic crystal the emitter may undergo a so-called fractional decay, where the coupling to modes of very low group velocity leads to a situation in which some of the energy is preserved and some is lost to the environment. In order to quantify the phenomenon we have discussed how one can assign a degree of fractional decay to a given decay curve. Our calculations show that the effect will be visible only if the product of the coupling strength and the slope in the LDOS curve is sufficiently high. In the inverse opal photonic crystals the limiting form of the LDOS near the band edge can be shown to be a square root and so, in principle, could lead to this counter intuitive decay. Whether it is possible to manufacture a crystal of high enough purity and subsequently place a quantum dot inside it at the correct location is still an open question. In the calculations we used an analytical expression to the band edge LDOS in Si inverse opals to find the optimum position in the crystal for the observation. The analytical expression allowed for the inclusion of absorptive material loss in the model which was shown to be a limiting factor. In addition, we have discussed how the stabilization of the system during measurements may be very difficult because the effect is visible only in a very narrow frequency interval for the PCs in this study.

QDs not only act as sources of light but also inevitably scatter light in the material. We have described a self-consistent Dyson equation approach by which QDs can be added iteratively as perturbations to the background Green's tensor for the material. In order to obtain a suitable background Green's tensor, we used FDTD calculations providing both local and non-local properties of light scattering in the crystal. It was shown how many properties of the Green's tensor may be understood from electromagnetic resonances in the structure that can be interpreted as modes of the system. By application of a Dyson equation approach based on the numerical Green's tensor it was shown how the presence of a second QD inside the PC slab may act to qualitatively change the decay dynamics. This effect may be of importance in experiments and could be utilized for advanced control of light propagation in micro- and nanostructured media.

Whether in quantum optical communications, solar cells, lasers or other devices, technologies based on solid state quantum optics exploit fascinating quantum mechanical aspects of the light-matter interaction. With steady improvements in the manufacturing of both quantum dots and photonic crystals these technologies will likely form important parts of future optoelectronics industries.

Appendix A

The Green's tensor in homogeneous media

This appendix summarizes the explicit expressions for the electromagnetic Green's tensor in homogeneous media in which the waves are characterized by a wave number $k_{\mathrm{B}} = n_{\mathrm{B}} k_0$, where n_{B} is the refractive index and $k_0 = c/\omega$.

1D

In one dimension the light travels along the x-axis with the field oriented along the z-direction. The scattering calculation in this case is a scalar problem. The one dimensional Green's function is given as

$$\mathbf{G}^{\mathrm{B}}_{1\mathrm{D}}(x, x') = \frac{i}{2k_{\mathrm{B}}} \exp(ik_{\mathrm{B}}|x - x'|). \tag{A.1}$$

2D

In two dimensions the light travels in the xy-plane, $\mathbf{r} = (x, y)$, and the vector equation decouples into two independent equations for the Transverse Electric (TE) and the Transverse Magnetic (TM) polarizations. In the case of TE polarization, the electric field is oriented in the xy-plane, whereas, for TM polarization the electric field is oriented along the z-axis, and the scattering calculation is essentially a scalar problem. The two dimensional Green's tensor is given as

$$\mathbf{G}^{\mathrm{B}}_{2\mathrm{D}}(\mathbf{r}, \mathbf{r}') = \left(\mathbf{I} + \frac{\nabla\nabla}{k_{\mathrm{B}}^2}\right) \frac{i}{4} H_0(k_{\mathrm{B}}|\mathbf{r} - \mathbf{r}'|), \tag{A.2}$$

where H_0 is the Hankel function of the first kind of order 0. Second derivatives for the general cylindrical wavefunctions $\partial_\alpha \partial_\beta \{Z_\lambda(kr) \exp(i\lambda\varphi)\}$ are provided in

appendix B.2. Since the system is invariant along the z-axis, the differentiation in this direction vanishes and the Green's tensor reduces to the form

$$\mathbf{G}^{\mathrm{B}}_{2\mathrm{D}} = \begin{pmatrix} G_{xx} & G_{xy} & 0 \\ G_{yx} & G_{yy} & 0 \\ 0 & 0 & G_{zz} \end{pmatrix},$$

illustrating the decoupling of the two polarizations. Explicit expressions for the elements of the Green's tensor are given in Ref. [55] and follow from Eq. (A.2) and the expressions in appendix B.2,

$$G_{xx}(\mathbf{r},\mathbf{r}') = \frac{i}{4}\sin^2(\theta)H_0(k_{\mathrm{B}}R) + \frac{i}{4}\frac{\cos(2\theta)}{k_{\mathrm{B}}R}H_1(k_{\mathrm{B}}R), \tag{A.3a}$$

$$G_{xy}(\mathbf{r},\mathbf{r}') = \frac{i}{8}\sin(2\theta)H_2(k_{\mathrm{B}}R), \tag{A.3b}$$

$$G_{yx}(\mathbf{r},\mathbf{r}') = G_{xy}(\mathbf{r},\mathbf{r}'), \tag{A.3c}$$

$$G_{yy}(\mathbf{r},\mathbf{r}') = \frac{i}{4}\cos^2(\theta)H_0(k_{\mathrm{B}}R) - \frac{i}{4}\frac{\cos(2\theta)}{k_{\mathrm{B}}R}H_1(k_{\mathrm{B}}R) \tag{A.3d}$$

$$G_{zz}(\mathbf{r},\mathbf{r}') = \frac{i}{4}H_0(k_{\mathrm{B}}R), \tag{A.3e}$$

in which (R,θ) are cylindrical coordinates of $\mathbf{r}'$ with respect to $\mathbf{r}$ and H_n is the Hankel function of the first kind of order n.

3D

In three dimensions the light travels in any of the three directions, and in general we cannot decouple the different polarizations. The three dimensional Green's tensor is given as

$$\mathbf{G}^{\mathrm{B}}_{3\mathrm{D}}(\mathbf{r},\mathbf{r}') = \left(\mathbf{I} + \frac{\nabla\nabla}{k_{\mathrm{B}}^2}\right)\frac{\exp(ik_{\mathrm{B}}|\mathbf{r}-\mathbf{r}'|)}{4\pi|\mathbf{r}-\mathbf{r}'|} \tag{A.4}$$

and we note that

$$\frac{\exp(ik_{\mathrm{B}}|\mathbf{r}-\mathbf{r}'|)}{4\pi|\mathbf{r}-\mathbf{r}'|} = \frac{ik_{\mathrm{B}}}{4\pi}h_0(k_{\mathrm{B}}|\mathbf{r}-\mathbf{r}'|),$$

where $h_0(r)$ is the spherical Hankel function of the first kind of order 0. Eq. (A.4) may be written explicitly as [55, 50]

$$\left(1 + \frac{ik_{\mathrm{B}}R - 1}{k_{\mathrm{B}}^2R^2} + \frac{3 - 3ik_{\mathrm{B}}R - k_{\mathrm{B}}^2R^2}{k_{\mathrm{B}}^2R^4}\mathbf{RR}\right)\frac{\exp(ik_{\mathrm{B}}R)}{4\pi R},$$

where $\mathbf{R} = \mathbf{r} - \mathbf{r}'$ and $R = |\mathbf{R}|$.

Appendix B

Miscellaneous cylinder function results

In this appendix we list a number of results for cylinder functions and cylindrical wavefunctions that have proven useful in the derivations.

B.1 Addition theorems for multipole expansions

The expansion of the Lippmann-Schwinger equation in chapter 3, and especially the calculation of matrix elements, relies heavily on the use of cylindrical wavefunctions. A number of addition theorems exist for cylindrical wavefunctions which may simplify the calculations considerably. Of special interest in this work is the Jacobi-Anger identity and the Graf addition theorem [51]. Below we summarize the results in forms suitable for the present application.

B.1.1 Jacobi-Anger identity

For a plane wave traveling at an angle θ with respect to the x axis, the expansion in terms of cylindrical wavefunctions is given by the Jacobi-Anger identity,

$$e^{i\,k_0 r\,\cos(\varphi-\theta)} = \sum_{n=-\infty}^{\infty} i^n e^{-i\,n\,\theta} J_n(k_0 r) e^{i\,n\,\varphi}, \tag{B.1}$$

in which (r, φ) are cylindrical coordinates and J_n is the Bessel function of order n.

B.1.2 Graf's addition theorem

The Graf addition theorem may be used to express the cylindrical wavefunctions in one local coordinate system in terms of cylindrical wavefunctions in a different local coordinate system.

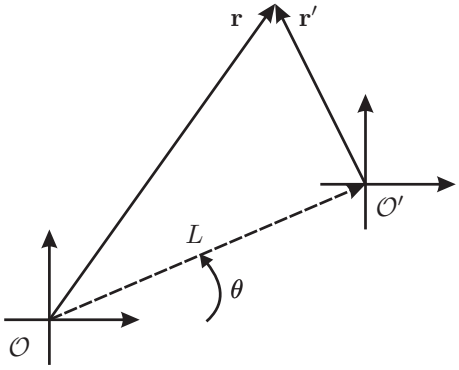

Figure B.1: Sketch of relative coordinates as used in the expression for Graf's addition theorem.

We consider the cylindrical coordinates $\mathbf{r} = (r, \varphi)$ and $\mathbf{r}' = (r', \varphi')$, centered at two different positions $\mathcal{O}$ and $\mathcal{O}'$, respectively, where (L, θ) denote the coordinates of $\mathcal{O}'$ with respect to $\mathcal{O}$ as shown in Fig. B.1. Using this notation we express the Graf addition theorem as

$$Z_n(kr)e^{in(\varphi-\theta)} = \sum_{\mu=-\infty}^{\infty} Z_{n+\mu}(kL)J_\mu(kr')(-1)^\mu e^{i\mu(\theta-\varphi')}, \tag{B.2}$$

where Z_n is a solution to Bessel's differential equation for integer n. If $Z_n = J_n$, the expansion is valid for all values of r', otherwise it is valid only for $r' < L$.

B.2 Derivatives for cylindrical wavefunctions

Ref. [51] provides general derivatives for the cylindrical wavefunctions $Z_\lambda(kr)\exp(i\lambda\varphi)$, in which (r, φ) are cylindrical coordinates and Z_λ is a solution to Bessel's differential equation for integer λ. Below we summarize the results for the double derivatives that enter the matrix elements in chapter 3:

$$\frac{\partial^2}{\partial x^2}\left\{Z_\lambda(kr)e^{i\lambda\varphi}\right\} = \frac{k^2}{4}\Big\{Z_{\lambda+2}(kr)e^{i(\lambda+2)\varphi} + Z_{\lambda-2}(kr)e^{i(\lambda-2)\varphi} - 2Z_\lambda(kr)e^{i\lambda\varphi}\Big\}, \tag{B.3}$$

$$\frac{\partial^2}{\partial y^2}\left\{Z_\lambda(kr)e^{i\lambda\varphi}\right\} = -\frac{k^2}{4}\Big\{Z_{\lambda+2}(kr)e^{i(\lambda+2)\varphi} + Z_{\lambda-2}(kr)e^{i(\lambda-2)\varphi} + 2Z_\lambda(kr)e^{i\lambda\varphi}\Big\}, \tag{B.4}$$

$$\frac{\partial^2}{\partial x\partial y}\left\{Z_\lambda(kr)e^{i\lambda\varphi}\right\} = -i\frac{k^2}{4}\Big\{Z_{\lambda+2}(kr)e^{i(\lambda+2)\varphi} - Z_{\lambda-2}(kr)e^{i(\lambda-2)\varphi}\Big\}. \tag{B.5}$$

B.3 Special integrals involving Bessel functions

Below we summarize, for easy reference, a few results that are important in connection with this work:

$$\int_0^R J_n(k_{\mathrm{R}}r)J_n(k_{\mathrm{B}}r)r\mathrm{d}r = \frac{R\left(k_{\mathrm{B}}J_n(k_{\mathrm{R}}R)J_n'(k_{\mathrm{B}}R) - k_{\mathrm{R}}J_n'(k_{\mathrm{R}}R)J_n(k_{\mathrm{B}}R)\right)}{k_{\mathrm{R}}^2 - k_{\mathrm{B}}^2}, \tag{B.6}$$

for $k_{\mathrm{R}} \neq k_{\mathrm{B}}$. In the case $k_{\mathrm{R}} = k_{\mathrm{B}} = k$ we have the result:

$$\int_0^R \left(J_n(kr)\right)^2 r\mathrm{d}r = \frac{R^2}{2}\left(\left(J_n'(kR)\right)^2 + (1 - \frac{n^2}{k^2R^2})\left(J_n(kR)\right)^2\right). \tag{B.7}$$

From Eqs. (3.9), (3.10) and (3.12) we have the relation:

$$\int_0^\infty H_0(k_{\mathrm{B}}r)J_0(k_{\mathrm{R}}r)r\mathrm{d}r = \frac{-2i}{\pi(k_{\mathrm{R}}^2 - k_{\mathrm{B}}^2)}, \tag{B.8}$$

for $k_{\mathrm{R}} \neq k_{\mathrm{B}}$.

Appendix C

Practical evaluation of matrix elements

C.1 Calculation of $I_\mu^{\alpha\beta}$

In this appendix we evaluate the integral

$$I_\mu^{\alpha\beta} = \int_{P-\delta A} G_{\alpha\beta}^{\mathrm{B}}(0,\mathbf{R}) J_\mu(k_{\mathrm{R}} R)(-1)^\mu e^{-i\mu\theta} \mathrm{d}\mathbf{R},$$

which enters the expression for $\mathcal{A}^{\alpha\beta}$ in Section 3.4.1.

For TM polarization, $(\alpha,\beta) = (z,z)$, the angular integration is nonzero only for $\mu = 0$ and the resulting integral may be evaluated by comparing to the Mie scattering result as discussed in section 3.4.1.

For TE polarization, the integrand has a pole at the origin, so we rewrite this integral in a form more suitable for numerical quadrature. Although the procedure is the same, the resulting integrals differ slightly, depending on which of the elements of the Green's tensor we consider (see Ref. [55] for explicit expressions for the

elements). For I_μ^{xx} we get

$$\begin{aligned}
I_\mu^{xx} &= \frac{i}{4}\int_0^\infty\int_0^{2\pi}\left\{\sin^2\theta H_0(k_\mathrm{B}R)+\frac{\cos(2\theta)}{k_\mathrm{B}R}H_1(k_\mathrm{B}R)\right.\\
&\quad\left.+\frac{2i}{\pi}\frac{\cos(2\theta)}{k_\mathrm{B}^2R^2}\right\}J_\mu(k_\mathrm{R}R)(-1)^\mu e^{-i\mu\theta}R\mathrm{d}\theta\mathrm{d}R\\
&\quad-\frac{i}{4}\lim_{\delta R\to 0}\int_{\delta R}^\infty\int_0^{2\pi}\frac{2i}{\pi}\frac{\cos(2\theta)}{k_\mathrm{B}^2R^2}J_\mu(k_\mathrm{R}R)(-1)^\mu e^{-i\mu\theta}R\mathrm{d}\theta\mathrm{d}R\\
&=\frac{i\pi}{4}\int_0^\infty\left\{(-\frac{1}{2}\delta_{\mu,-2}+\delta_{\mu,0}-\frac{1}{2}\delta_{\mu,2})H_0(k_\mathrm{B}R)\right.\\
&\quad\left.+(\delta_{\mu,-2}+\delta_{\mu,2})\left(\frac{H_1(k_\mathrm{B}R)}{k_\mathrm{B}R}+\frac{2i}{\pi k_\mathrm{B}^2R^2}\right)\right\}J_\mu(k_\mathrm{R}R)\,R\mathrm{d}R\\
&\quad+\frac{1}{2}\lim_{\delta R\to 0}\int_{\delta R}^\infty(\delta_{\mu,-2}+\delta_{\mu,2})\frac{J_\mu(k_\mathrm{R}R)}{k_\mathrm{B}^2R^2}R\mathrm{d}R,
\end{aligned}$$

where $\delta_{\mu,\lambda}$ is the Kronecker delta. The first integral is now well behaved and may be directly evaluated, whereas for the second integral we may use the identity

$$\lim_{\delta R\to 0}\int_{\delta R}^\infty\frac{J_2(k_\mathrm{R}R)}{k_\mathrm{B}^2R^2}R\mathrm{d}R=\frac{1}{2k_\mathrm{B}^2}.$$

In a similar way we rewrite the expressions for I_μ^{yy} and I_μ^{xy} as follows:

$$\begin{aligned}
I_\mu^{yy} &= \frac{i\pi}{4}\int_0^\infty\left\{(\frac{1}{2}\delta_{\mu,-2}+\delta_{\mu,0}+\frac{1}{2}\delta_{\mu,2})H_0(k_\mathrm{B}R)\right.\\
&\quad\left.-(\delta_{\mu,-2}+\delta_{\mu,2})\left(\frac{H_1(k_\mathrm{B}R)}{k_\mathrm{B}R}+\frac{2i}{\pi k_\mathrm{B}^2R^2}\right)\right\}J_\mu(k_\mathrm{R}R)\,R\mathrm{d}R\\
&\quad-\frac{1}{4k_\mathrm{B}^2}(\delta_{\mu,-2}+\delta_{\mu,2}).
\end{aligned}$$

$$\begin{aligned}
I_\mu^{xy} &= -\frac{\pi}{4}\int_0^\infty(\delta_{\mu,-2}-\delta_{\mu,2})\left(\frac{1}{2}H_2(k_\mathrm{B}R)+\frac{2i}{\pi k_\mathrm{B}^2R^2}\right)J_\mu(k_\mathrm{R}R)\,R\mathrm{d}R\\
&\quad+\frac{i}{4k_\mathrm{B}^2}(\delta_{\mu,-2}-\delta_{\mu,2}).
\end{aligned}$$

C.2 Simplification of matrix element calculations

Evaluation of the matrix elements may be substantially simplified and may typically be reduced to the evaluation of a number of integrals of dimension at most two. We first describe a general procedure for the integration and apply it to the specific

case of a square scatterer in section C.2.1. Subsequently, we illustrate the utility of the procedure in the calculation of matrix element for TM polarization in section C.2.2.

Although we focus on square scatterers in TM polarization, the procedure may be extended directly to TE polarization as well as to scatterers of any shape for which the angle can be expressed as a function of the radius in cylindrical coordinates.

C.2.1 A procedure for integrating across a square domain

In general, the integrals for the calculation of the matrix elements may be written as

$$I_A = \int_A f(r) e^{ix\varphi} r \mathrm{d}\varphi \mathrm{d}r, \tag{C.1}$$

in which $f(r)r$ is any integrable function of the radial coordinate and $x \in \mathbb{Z}$. A denotes the area of integration which may be a sub domain of a scatterer. In the case of a square scatterer, the matrix elements may be naturally split into a sum of four such integrals differing only by a phase factor:

$$I_A = \left(1 + e^{i\pi x/2} + e^{i\pi x} + e^{i3\pi x/2}\right) \int_{-\pi/4}^{\pi/4} \int_0^{R(\varphi)} f(r) e^{ix\varphi} r \mathrm{d}r \mathrm{d}\varphi, \tag{C.2}$$

in which

$$R = \frac{R_0}{\cos(\pi/4 - \varphi)}$$

expresses the perimeter of the square in terms of the angle, cf. Fig. C.1. Using the identity

$$\sum_{k=0}^{N-1} e^{i2\pi xk/N} = \begin{cases} N, & \text{for } x = pN,\ p \in \mathbb{Z} \\ 0, & \text{otherwise,} \end{cases}$$

we realize that the integral is nonzero only for certain values of x. Due to the simple angular dependence, we further simplify the integral by changing the order of integration and expressing the limits for the angular integration as a function of radius:

$$I_A = 4 \int_0^R f(r) g_x(r) r \mathrm{d}r,$$

where, for $x \in \mathbb{Z}$, we have

$$g_x(\varphi) = \begin{cases} 2\,\Phi(r), & \text{for } x = 0 \\ 2x^{-1} \sin(x\Phi(r)), & \text{otherwise,} \end{cases} \tag{C.3}$$

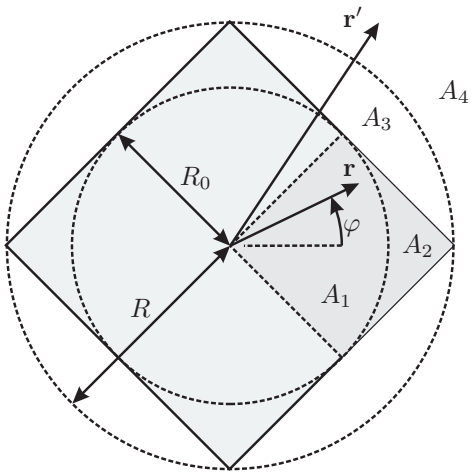

Figure C.1: The integration across a square scatterer is reformulated in terms of a number of integrals across a quarter of the square (indicated by the dark gray shading).

with

$$\Phi(r) = \begin{cases} \pi/4, & \text{for } r < R_0 \\ \pi/4 - \arccos\left(R_0/r\right), & \text{for } R_0 < r < R. \end{cases}$$

C.2.2 Example calculations

As an example of the utility of the above approach, we apply the procedure to simplify the integrals in the case of TM polarization. Example results for the calculation of the TM Green's tensor for a collection of square scatterers are presented in section 3.5.2.

Self-term

Using the procedure of section 3.4.1, the matrix element is first written as $G^{zz}_{mn} = \mathcal{A}^{zz}_{mn} - \mathcal{B}^{zz}_{mn}$, where

$$\begin{aligned} \mathcal{A}^{zz}_{mn} &= \int_D J_m(k_\mathrm{R} r) J_n(k R_r) e^{i(n-m)\varphi} r \mathrm{d}\varphi \mathrm{d}r \times \frac{i\pi}{2} \int_0^\infty H_0(k_\mathrm{B} r) J_0(k_\mathrm{R} r) r \mathrm{d}r \\ &= \int_D J_m(k_\mathrm{R} r) J_n(k R_r) e^{i(n-m)\varphi} r \mathrm{d}\varphi \mathrm{d}r \times \frac{1}{(k_\mathrm{R}^2 - k_\mathrm{B}^2)}. \end{aligned}$$

Comparing to Eq. (C.1) we identify $f(r) = J_m(k_\mathrm{R} r) J_n(k_\mathrm{R} r)$ and $x = n - m$. Thus we see that $\mathcal{A}^{zz}_{mn}$ is non-zero only for $n - m = 4p$ with $p \in \mathbb{Z}$. In this case we

rewrite the integral as a one-dimensional integral as

$$\mathcal{A}_{mn}^{zz} = \frac{4}{(k_{\mathrm{R}}^2 - k_{\mathrm{B}}^2)} \int_0^R J_m(k_{\mathrm{R}} r) J_n(k_{\mathrm{R}} r) g_{n-m}(r) r \mathrm{d}r,$$

which we may easily evaluate using numerical quadrature. For the $\mathcal{B}_{mn}^{zz}$ term the integration over $\mathbf{r}'$ is split depending on the sign of $r - r'$. Eq. (3.10) is written as

$$b_{mn}^{zz}(\mathbf{r}, \mathbf{r}') = K_m K_n \frac{i}{4} \sum_\mu J_m(k_{\mathrm{R}} r) J_\mu(k_{\mathrm{B}} r) e^{i(\mu - m)\varphi} H_\mu(k_{\mathrm{B}} r') J_n(k_{\mathrm{R}} r') e^{i(n-\mu)\varphi'},$$

for $r' > r$, and we have used the relation $Z_{-m} = (-1)^m Z_m$. Similarly, Eq. (3.11) is written as

$$b_{mn}^{zz}(\mathbf{r}, \mathbf{r}') = K_m K_n \frac{i}{4} \sum_\mu J_m(k_{\mathrm{R}} r) H_\mu(k_{\mathrm{B}} r) e^{i(\mu - m)\varphi} J_\mu(k_{\mathrm{B}} r') J_n(k_{\mathrm{R}} r') e^{i(n-\mu)\varphi'},$$

which holds for $r' < r$.

In addition, it is convenient to split up the integration depending on the sign of $r' - R$ and to split up the integration over r as well, depending on the sign of $r - R_0$. In this way we end up with a total of 5 integrals for $\mathcal{B}_{mn}^{zz}$. As we shall see, three of these integrals reduce to products of one-dimensional integrals whereas the last two may be expressed as two-dimensional integrals.

Case I: $r < R_0$ and $r' < R$

The integration over $\mathbf{r}$ is non-zero only for $\mu = m$ in which case the integral is written as

$$\mathcal{B}_{mn}^{\mathrm{I}} = K_m K_n \frac{i\pi}{2} \int_0^{R_0} J_m(k_{\mathrm{R}} r) J_m(k_{\mathrm{B}} r) r \mathrm{d}r \int H_m(k_{\mathrm{B}} r') J_n(k_{\mathrm{R}} r') e^{i(n-m)\varphi'} \mathrm{d}\mathbf{r}',$$

where the integration over $\mathbf{r}'$ is now over all points outside the square for which $r' < R$. Based on the discussion in section C.2.1, we realize that this integral is non-zero only for $n - m = 4p$, $p \in \mathbb{Z}$, in which case it can be written in terms of a single integral across the domain A_3 in Fig. C.1.

Case II: $r < R_0$ and $r' > R$

The integral is now over two circular domains and is non-zero only for $\mu = m = n$ in which case we get

$$\mathcal{B}_{mm}^{\mathrm{II}} = i\pi^2 K_m K_n \int_0^{R_0} J_m(k_{\mathrm{R}} r) J_m(k_{\mathrm{B}} r) r \mathrm{d}r \int_R^\infty H_m(k_{\mathrm{B}} r') J_m(k_{\mathrm{R}} r') r' \mathrm{d}r'.$$

Case III: $r > R_0$ **and** $r' > R$

The integration over $\mathbf{r}'$ is nonzero only for $\mu = n$ and the integral is written as

$$\mathcal{B}^{\mathrm{III}}_{mn} = K_m K_n \frac{i\pi}{2} \int J_m(k_{\mathrm{R}} r) J_n(k_{\mathrm{B}} r) e^{i(n-m)\varphi} \mathrm{d}\mathbf{r} \int_R^\infty H_n(k_{\mathrm{B}} r') J_n(k_{\mathrm{R}} r') r' \mathrm{d}r',$$

where the integration over $\mathbf{r}$ is now over all points within the square for which $r < R$. Similar to Case I, we may realize that the integral is non-zero only for $n - m = 4p,\ p \in \mathbb{Z}$ in which case we can recast it in terms of a single integral over A_2.

Case IV: $r > R_0$ **and** $r' < R$ **and** $r' < r$

The integral is written as

$$\begin{aligned}\mathcal{B}^{\mathrm{IV}}_{mn} = K_m K_n \frac{i}{4} \sum_\mu \int J_m(k_{\mathrm{R}} r) H_\mu(k_{\mathrm{B}} r) e^{i(\mu-m)\varphi} \mathrm{d}\mathbf{r} \\ \times \int J_\mu(k_{\mathrm{B}} r') J_n(k_{\mathrm{R}} r') e^{i(n-\mu)\varphi} \mathrm{d}\mathbf{r}',\end{aligned}$$

where now the integration over $\mathbf{r}$ is over all points within the square for which $r > R_0$, and the integration over $\mathbf{r}'$ is over all points outside the square for which $r' < r$. The integrands depend non-trivially on both φ and φ'. For both integrals, however, we can use the discussion in section C.2.1 to conclude that for $(p, q) \in \mathbb{Z}^2$ we must have

$$\mu - m = 4p \ \wedge\ n - \mu = 4q \quad \Rightarrow \quad n - m = 4(p+q) = 4s, \quad s \in \mathbb{Z}$$

in which case the two integrals may be recast in terms of single integrals over A_2 and (part of) A_3 respectively. Unfortunately, the difference in the expression for the integrands depending on the sign of $r - r'$ means that r will have to enter in the upper limit of integration for r', effectively coupling the two integrations. For $n - m = 4s,\ s \in \mathbb{Z}$, we thus have

$$\begin{aligned}\mathcal{B}^{\mathrm{IV}}_{mn} = 4iK_m K_n \sum_p \int_{R_0}^R J_m(k_{\mathrm{R}} r) H_{m+4p}(k_{\mathrm{B}} r) g_{4p}(r) r \\ \times \int_{R_0}^r J_{m+4p}(k_{\mathrm{B}} r') J_n(k_{\mathrm{R}} r') g'_{4(s-p)}(r') r' \mathrm{d}r' \mathrm{d}r,\end{aligned}$$

where $g_x(r)$ is given in Eq. (C.3) and $g'_x(r')$ derives from integrating $\exp(ix\varphi')$ within the limits of A_3 set by r':

$$g'_x(r') = \begin{cases} \exp(ix\pi/4)\ 2\Phi'(r'), & \text{for } x = 0 \\ \exp(ix\pi/4)\ \frac{2}{x}\sin(x\Phi'(r')), & \text{otherwise,} \end{cases}$$

with $\Phi'(r') = \arccos(R_0/r)$.

Case V: $r > R_0$ **and** $r' < R$ **and** $r' > r$

The integral is written as

$$\mathcal{B}^{\mathrm{V}}_{mn} = K_m K_n \frac{i}{4} \sum_{\mu} \int J_m(k_{\mathrm{R}} r) J_\mu(k_{\mathrm{B}} r) e^{i(\mu - m)\varphi} \mathrm{d}\mathbf{r} \times \int H_\mu(k_{\mathrm{B}} r') J_n(k_{\mathrm{R}} r') e^{i(n-\mu)\varphi} \mathrm{d}\mathbf{r}',$$

and an analysis similar to case IV reveals that the integral is nonzero only for $n - m = 4p,\ p \in \mathbb{Z}$ in which case we can recast it in terms of a two single integrals over A_2 and (the rest of) A_3. Again, however, these integrals are coupled, since r will enter as the lower limit of integration for r':

$$\mathcal{B}^{\mathrm{V}}_{mn} = 4iK_m K_n \sum_p \int_{R_0}^{R} J_m(k_{\mathrm{R}} r) J_{4p-m}(k_{\mathrm{B}} r) g_{4p}(r) r \times \int_{R_0}^{r} H_{4p-m}(k_{\mathrm{B}} r') J_n(k_{\mathrm{R}} r') g'_{4(s-p)}(r') r' \mathrm{d}r' \mathrm{d}r.$$

In both the cases IV and V, a sum over p remains. The terms in the sum, however, drop rapidly to zero as the orders of the Bessel and Hankel functions increase.

Scattering terms

For the scattering terms, Eq. (3.13) is written for TM polarization as

$$\begin{aligned} G^{zz}_{mn} =& \frac{i}{4} \sum_{\mu,\lambda} H_{\mu+\lambda}(k_{\mathrm{B}} L)(-1)^{\mu+\lambda} e^{i(\mu+\lambda)\theta} \\ &\times \int_{D_m} K_m J_m(k_m r) J_\lambda(k_{\mathrm{B}} r) e^{i(\lambda - m)\,\varphi} \mathrm{d}\mathbf{r} \\ &\times \int_{D_n} K_n J_\mu(k_{\mathrm{B}} r') J_n(k_n r') e^{i\,(n-\mu)\,\varphi'} \mathrm{d}\mathbf{r}', \end{aligned} \tag{C.4}$$

where now the two domains of integration is separated in space and we can apply the procedure of section C.2.1 to each of the two integrations separately. From this we conclude that for $(p, q) \in \mathbb{Z}^2$ only terms with $\lambda - m = 4p$ and $n - \mu = 4q$ are non-zero. Note, however, that the sums over both μ and λ remain in the final expression. As in cases IV and V for the self-terms, the terms drop rapidly with increasing $|\lambda|$ and $|\mu|$.

Appendix D

Local density-of-states in homogeneous media

Homogeneous media are characterized by the linear dispersion

$$\omega \;=\; \frac{c}{n}|\mathbf{k}|, \tag{D.1}$$

in which $n = \sqrt{\epsilon_{\mathrm{r}}}$ is the refractive index. The modes are plane waves indexed by $\mu = (\mathbf{k}, p)$, where $\mathbf{k}$ and p are wave vectors and polarizations, respectively. The waves are normalized according to Eq. (2.7) as

$$\mathbf{f}_\mu(\mathbf{r}) \;=\; \frac{e^{\,i\,\mathbf{k}\,\cdot\,\mathbf{r}}}{\sqrt{\epsilon_{\mathrm{r}}\,V}}\mathbf{e}_\mu,$$

where V is the normalization volume. The expression for the projected LDOS, Eq. (2.8), then reads

$$\rho_{\mathrm{hom}}(\omega, \mathbf{r}) = \sum_\mu |\mathbf{e}_x \cdot \mathbf{e}_\mu|^2 \, |\frac{e^{i\,\mathbf{k}\,\cdot\,\mathbf{r}}}{\sqrt{\epsilon_{\mathrm{r}}\,V}}|^2 \, \delta(\omega - \omega_{\mathbf{k}}). \tag{D.2}$$

In order to evaluate the LDOS we convert the sum over wave vectors into an integral as

$$\sum_{\mathbf{k}} \to \int_{\Omega_{\mathbf{k}}} \frac{V}{(2\pi)^3}\,\mathrm{d}\mathbf{k},$$

where $\Omega_{\mathbf{k}}$ is the volume of the reciprocal space. Defining a coordinate system so that $\mathbf{e}_x = \hat{\mathbf{z}}$, we may choose one polarization to be orthogonal to $\mathbf{e}_x$ as shown in figure D.1. The projection of the other polarization is given as $\mathbf{e}_x \cdot \mathbf{e}_{\mu 1} = \cos(\pi/2 - \theta) = \sin\theta$.

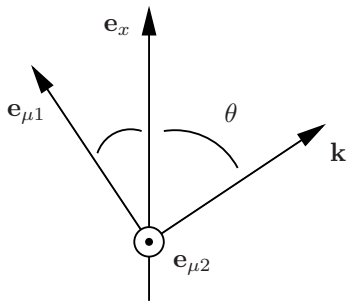

Figure D.1: Sketch illustrating the projection of the EM field onto the direction $\mathbf{e}_x$.

Rewriting the integral using polar coordinates we get the projected LDOS:

$$\begin{aligned}\rho_{\mathrm{hom}}(\omega,\mathbf{r}) &= \frac{1}{(2\pi)^3}\int_0^{2\pi}\int_0^{\pi}\int_0^{\infty} \sin^2\theta \left|\frac{e^{i\,\mathbf{k}\cdot\mathbf{r}}}{\sqrt{\epsilon_{\mathrm{r}}}}\right|^2 \delta(\omega-\omega_{\mathbf{k}})\,\sin\theta\,k^2\mathrm{d}k\,\mathrm{d}\theta\,\mathrm{d}\phi. \\ &= \frac{1}{(2\pi)^2}\int_0^{\pi}\int_0^{\infty} \sin^3\theta\,\frac{1}{n^2}\,\delta(\omega-\omega_{\mathbf{k}})\,\left(\frac{n\,\omega_{\mathbf{k}}}{c}\right)^2\,\mathrm{d}\theta\,\frac{\partial k}{\partial\omega}\,\mathrm{d}\omega \\ &= \frac{n\,\omega^2}{3\pi^2c^3}. \end{aligned} \tag{D.3}$$

This is the LDOS that should be used to describe spontaneous emission from an emitter in a homogeneous medium, even if the orientation of the dipole moment of the emitter is random, since we can always choose the $\hat{\mathbf{z}}$ axis to lie along $\mathbf{e}_x$ and end up with the same result.

D.1 Alternative derivation

It is illustrative to derive Eq. (D.3) in an alternative way based on Eq. (4.14). Again, we work with the coordinate system in Fig. D.1 in which $\mathbf{e}_x = \mathbf{e}_z$ and we have chosen one of the polarizations to be orthogonal to $\mathbf{e}_x$. The integration is carried out over surfaces of constant frequency which, given the homogeneous medium dispersion in Eq. (D.1), are concentric spheres centered on the origin. The integral is calculated as

$$\begin{aligned}\rho_{\mathrm{hom}}(\omega) &= \frac{V}{(2\pi)^3}\int_0^{2\pi}\int_0^{\pi}\frac{\sin^2\theta}{|\nabla_{\mathbf{k}}\omega(\mathbf{k})|}\frac{1}{n^2V}\,\left(\frac{n}{c}\omega\right)^2\,\sin\theta\,\mathrm{d}\theta\,\mathrm{d}\varphi \\ &= \frac{n\,\omega^2}{(2\pi)^3c^3}\int_0^{2\pi}\int_0^{\pi}\sin^3\theta\,\mathrm{d}\theta\,\mathrm{d}\varphi \\ &= \frac{n\,\omega^2}{3\pi^2c^3}. \end{aligned} \tag{D.4}$$

Appendix E

The Coupling parameter β

The parameter β is defined in section 4.2.3 as

$$\beta = \frac{q^2 p^2}{6\hbar m_0^2 \pi^2 \epsilon_0 c^3}. \tag{E.1}$$

Note that β is dimensionless and is related to the vacuum decay rate at the (angular) frequency ω_x as

$$\Gamma_0(\omega_x) = 2\pi\omega_x\beta. \tag{E.2}$$

A formulation in terms of β, Eq. (E.1), is natural when recasting the equations in dimensionless form. Note that β includes also a factor of $1/3\pi^2c^3$ from the projected LDOS of free space. The parameter β is not identical to the parameter called β in the article by Nipun Vats *et al.* [62]. We will refer to the parameter in Ref. [62] as β_{NV}. We used the same letter because they appear at the same place in the equations, but whereas β is dimensionless, β_{NV} is not. Indeed, using the relation

$$d^2 = \frac{q^2 p^2}{\omega_x^2 m_0^2}, \tag{E.3}$$

where d is the dipole moment, we may write β as

$$\beta = \frac{\omega_x^2 d^2}{6\pi^2 \hbar \epsilon_0 c^3},$$

and we see that

$$\beta = \frac{2}{c^3}\beta_{\mathrm{NV}}.$$

E.1 Relation to oscillator strength

As discussed above, the dimensionless parameter β is convenient from the point of view that it arises naturally when recasting the equations of motion in dimensionless form. It is a measure of the light-matter coupling strength, and it is related directly to the decay rate in free space through Eq. (E.2). However, other people use other measures for the light-matter coupling strength such as the oscillator strength. The oscillator strength is defined as (see eg. Ref. [61] or the supporting information for Ref. [112]):

$$f_{\mathrm{eg}} = \frac{2m_0\omega_x d^2}{3\hbar q^2}.$$

Comparing to Eq. (E.1) and using Eq. (E.3) we see that

$$\beta = \frac{q^2\omega_x}{4m_0\pi^2\epsilon_0 c^3} f_{\mathrm{eg}} = 2.99\times10^{-24}\,\mathrm{s}\times\omega_x f_{\mathrm{eg}}. \tag{E.4}$$

In Fig. 1 of Ref. [111], the energy is shown as a function of radius. Choosing a radius of $r = 2.5\,\mathrm{nm}$ we read off the energy $\hbar\omega_x = 1.2\mathrm{eV}$. The oscillator strength is shown as function of radius in Fig. 3 of Ref. [111]. At $r = 2.5\,\mathrm{nm}$ we read off an oscillator strength of $f_{\mathrm{eg}}^{\mathrm{InAs}} = 1.7$. Inserting in Eq. (E.4) we get

$$\beta = 2.99\times10^{-24}\,\mathrm{s}\times\frac{1.2\,\mathrm{eV}}{\hbar}1.7 = 9.3\times10^{-9}\approx10^{-8}.$$

In Ref. [112] the authors fit a theoretical curve to experimental data to get the emission energy (in eV) as a function of quantum dot diameter d (in nm):

$$E_{\mathrm{PbSe}}(d) = 0.278 + \frac{1}{0.016d^2 + 0.209d + 0.45}$$

The oscillator strength is shown as a function of diameter in Fig. 4(e) of Ref. [112]. Reading off an approximate slope for the linear fit, we write the oscillator strength as a function of diameter d (in nm) as

$$f_{\mathrm{eg}}^{\mathrm{PbSe}}(d) \approx \frac{29}{9}d.$$

Using these relations, we see that quantum dots of diameter $d = 4.5$ have an energy of $E_{\mathrm{PbSe}}(4.5) = 0.86\,\mathrm{eV}$ and an oscillator strength of $f_{\mathrm{eg}}^{\mathrm{PbSe}}(4.5) = 14.5$. Inserting in Eq. E.4 we get

$$\beta = 2.99\times10^{-24}\,\mathrm{s}\times\frac{0.86\,\mathrm{eV}}{\hbar}14.5 = 5.66\times10^{-8}.$$

Appendix F

Local density-of-states from dispersion surfaces

At the X-point the Brillouin zone is invariant under rotations of $\pi/2$ and π around the axis from the Γ point to the X point. Therefore, the limiting forms of the dispersion surfaces at these points are ellipsoids. Working in a coordinate system centered on the X-point, the dispersion surface is expanded as

$$\omega' \;=\; \frac{1}{2}\left(\omega_{xx}k_x^2 + \omega_{yy}k_y^2 + \omega_{zz}k_z^2\right),$$

or equivalently

$$1 \;=\; \left(\frac{k_x}{a}\right)^2 + \left(\frac{k_y}{b}\right)^2 + \left(\frac{k_z}{c}\right)^2, \tag{F.1}$$

where $a = \sqrt{2\omega'/\omega_{xx}}$ and similarly for b and c and $\omega' = \omega - \omega_{\mathrm{BE}}$. The absolute value of the gradient is given as

$$|\nabla_{\mathbf{k}}\omega| \;=\; \sqrt{\omega_{xx}^2k_x^2 + \omega_{yy}^2k_y^2 + \omega_{zz}^2k_z^2}, \tag{F.2}$$

where, due to the symmetry of the Brillouin zone, two of the curvatures ω_{ii} will be equal. Which, however, depend on which of the 6 X points we consider. Due to the ellipsoidal shapes of the dispersion surfaces, the differential area element $\mathrm{d}A$ depends on the coordinates. We may express the vector $\mathbf{k}$ on the dispersion surface as

$$\mathbf{k}(\theta,\varphi) \;=\; (a\,\sin\theta\,\cos\varphi\,,\, b\,\sin\theta\,\sin\varphi\,,\, c\,\cos\theta), \tag{F.3}$$

and the differential area element is then given as $\mathrm{d}A = |\mathbf{k}_\theta \times \mathbf{k}_\varphi|\,\mathrm{d}\theta\,\mathrm{d}\varphi$, where the subscripts refer to partial differentiation. Carrying out the derivatives and the cross

product we get

$$|\mathbf{k}_\theta \times \mathbf{k}_\varphi|^2 \;=\; b^2 \sin^2\theta \,\left(a^2\cos^2\theta + c^2\sin^2\theta\right).$$

Note, that for spherical dispersion surfaces we have $a = b = c$ and the expression reduces to $\mathrm{d}A = a^2|\sin\theta|\,\mathrm{d}\theta\,\mathrm{d}\varphi$, cf. Eq. (D.4). At any X point we may in general choose a local coordinate system at $\mathbf{k} = \mathbf{k}_0$, so that in this coordinate system we have $a = b \neq c$. Using these coordinates, the area element is given as

$$\mathrm{d}A \;=\; a^2|\sin\theta|\sqrt{\cos^2\theta + \frac{c^2}{a^2}\sin^2\theta} \;=\; \frac{2\,\omega'}{\omega_{xx}}\,|\sin\theta|\sqrt{\cos^2\theta + \frac{\omega_{xx}}{\omega_{zz}}\sin^2\theta}.$$

Further, using Eq. (F.3), the absolute value of the gradient, Eq. (F.2) may be expressed as

$$|\nabla_{\mathbf{k}}\omega(\mathbf{k})| \;=\; \sqrt{2\omega'\,\omega_{zz}}\sqrt{\cos^2\theta + \frac{\omega_{xx}}{\omega_{zz}}\sin^2\theta},$$

so that the LDOS is given as

$$\begin{aligned}\rho_x(\omega',\mathbf{r}) \;&=\; \sum_{n=1}^{6}\frac{V}{(2\pi)^3}\int_S \frac{I_n(\theta,\varphi,\mathbf{r})}{|\nabla_{\mathbf{k}}\omega(\mathbf{k})|}\mathrm{d}A \\ &=\; \sum_{n=1}^{6}\frac{V}{(2\pi)^3}\sqrt{\frac{2\,\omega'}{\omega_{xx}^2\,\omega_{zz}}}\int_{\theta_{min}}^{\theta_{max}}\int_{\varphi_{min}}^{\varphi_{max}} I_n(\theta,\varphi,\mathbf{r})\,|\sin\theta|\,\mathrm{d}\theta\,\mathrm{d}\varphi, \qquad \text{(F.4)}\end{aligned}$$

where the sum is now over the 6 X points and $I_n(\theta,\varphi,\mathbf{r}) = |\mathbf{e}_x\cdot\mathbf{f}_{\mu,n}(\mathbf{r})|^2$ denotes the projected electric field at the n'th X point. The X points are located in the center of the Brillouin zone edges and the integration limits are simply $\theta \in [0,\pi/2], \varphi \in [0,2\pi]$. To first order we simply set $I_n(\theta,\varphi,\mathbf{r}) = I_{n,0}(\mathbf{r})$ so that the LDOS is given as

$$\begin{aligned}\rho_x(\omega',\mathbf{r}) =\; &\sum_{n=1}^{6}\frac{V}{(2\pi)^3}\sqrt{\frac{2\,\omega'}{\omega_{xx}^2\,\omega_{zz}}}\,I_{n,0}(\mathbf{r})\int_0^{\pi/2}\int_0^{2\pi}|\sin\theta|\,\mathrm{d}\varphi\,\mathrm{d}\theta \\ =\; &\frac{I_0(\mathbf{r})}{(2\pi)^2}\sqrt{\frac{2\,\omega'}{\omega_{xx}^2\,\omega_{zz}}}, \qquad \text{(F.5)}\end{aligned}$$

in which

$$I_0(\mathbf{r}) = V\sum_{n=1}^{6}|\mathbf{e}_x\cdot\mathbf{f}_{\mu,n}(\mathbf{r})|^2.$$

Appendix G

Time dependence of coupled quantum dot dynamics

In this appendix we calculate the time dependent dynamics of coupled QDs as the Fourier transforms of the solutions to Heisenberg's equations of motion in the frequency domain.

From Fig. 5.8 and Eq. (5.2) we may interpret the field at the detector as the sum of contributions from two scattering channels. Therefore, it is instructive to consider first the case of a single QD. This is done in section G.1, and in section G.2 we consider the full system of two QDs.

G.1 The single quantum dot case

To calculate the electric field at the detector position, $\mathbf{r}_\mathrm{d}$, we follow Ref. [48] and rewrite Eq. (2.44) as

$$\mathbf{E}(\mathbf{r}_\mathrm{d},\omega) = \frac{(\omega_1^2-\omega^2)\,\mathbf{G}^\mathrm{B}(\mathbf{r}_\mathrm{d},\mathbf{r}_1,\omega)\mathbf{e}_1}{\omega_1^2-\omega^2-i2\omega_1 X_1(\omega)} S_1(\omega)\left[\frac{b(0)}{(\omega-\omega_1)}+\frac{b^\dagger(0)}{(\omega+\omega_1)}\right],$$

where $S_x(\omega) = id_x\omega^2/\epsilon_0 c^2$ and

$$X_x(\omega) = \mathrm{Im}\{\mathbf{e}_x\mathbf{G}^\mathrm{B}(\mathbf{r}_x,\mathbf{r}_x,\omega)\mathbf{e}_x\}\frac{d_x^2\omega^2}{\hbar\epsilon_0 c^2}.$$

At the (angular) frequencies of interest, X_1 is small compared to ω_1. Therefore, we expect the poles to be found close to $\omega = \pm\omega_1$ and we insert this in the small term to find

$$\Omega_\pm^2 = \omega_1^2 - i2\omega_1 X_1(\pm\omega_1).$$

We can now solve for $\Omega_\pm$ as

$$\Omega_\pm = \pm\omega_1\sqrt{1 - i\frac{2}{\omega_1}X_1(\pm\omega_1)} \approx \pm\omega_1 - iX_1(\omega_1), \tag{G.1}$$

where we have used the identity $\mathbf{G}(\mathbf{r},\mathbf{r},-\omega) = (\mathbf{G}(\mathbf{r},\mathbf{r},\omega))^*$, so that both poles have negative imaginary parts. The expression for the electric field operator is now rewritten and expanded in partial fractions as

$$\begin{aligned}
\mathbf{E}(\mathbf{r}_\mathrm{d},\omega) &= \frac{\mathbf{G}^\mathrm{B}(\mathbf{r}_\mathrm{d},\mathbf{r}_1,\omega)\mathbf{e}_1 S_1(\omega)}{(\omega-\Omega_+)(\omega-\Omega_-)}\left[(\omega+\omega_1)b(0) + (\omega-\omega_1)b^\dagger(0)\right]. \\
&= \frac{\mathbf{G}^\mathrm{B}(\mathbf{r}_\mathrm{d},\mathbf{r}_1,\omega)\mathbf{e}_1 S_1(\omega)}{\Omega_+-\Omega_-}\left(\frac{1}{\omega-\Omega_+} - \frac{1}{\omega-\Omega_-}\right) \\
&\quad\times\left[(\omega+\omega_1)b(0) + (\omega-\omega_1)b^\dagger(0)\right]. \\
&= \frac{\mathbf{G}^\mathrm{B}(\mathbf{r}_\mathrm{d},\mathbf{r}_1,\omega)\mathbf{e}_1 S_1(\omega)}{2\omega_1}\left(\frac{1}{\omega-\omega_1+iX_1(\omega_1)} - \frac{1}{\omega+\omega_1+iX_1(\omega_1)}\right) \\
&\quad\times\left[(\omega+\omega_1)b(0) + (\omega-\omega_1)b^\dagger(0)\right].
\end{aligned}$$

The term proportional to $b^\dagger(0)$ has a vanishing residue at the positive frequency pole. Therefore, the positive frequency part of the electric field may be calculated as

$$\begin{aligned}
\mathbf{E}^+(\mathbf{r}_\mathrm{d},t) &= \frac{1}{2\pi}\int_{-\infty}^{\infty}\frac{1}{2\omega_1}\frac{\mathbf{G}^\mathrm{B}(\mathbf{r}_\mathrm{d},\mathbf{r}_1,\omega)\mathbf{e}_1 S_1(\omega)}{\omega-\omega_1+iX_1(\omega_1)}(\omega+\omega_1)b(0)e^{-i\omega t}\mathrm{d}\omega \\
&= -iS_1(\omega_1)\mathbf{G}^\mathrm{B}(\mathbf{r}_\mathrm{d},\mathbf{r}_1,\omega_1)\mathbf{e}_1 e^{-i\Omega_+ t}\Theta(t)\,b(0),
\end{aligned} \tag{G.2}$$

where $\Theta(t)$ denotes the Heaviside step-function, and where we have simply evaluated the numerator at $\omega=\omega_1$. This is well justified although the Green's tensor in PCs (and hence the numerator) varies with ω in a highly non-trivial way, since the variations with frequency are slow compared to X_1. We can in principle include the rest of the spectrum (by numerical evaluation of the integral), but the major contribution to the dynamics stems form the pole term and so we focus on this.

Likewise, the negative frequency part is written as

$$\mathbf{E}^-(\mathbf{r}_\mathrm{d},t) = -iS_1(\omega_1)\left(\mathbf{G}^\mathrm{B}(\mathbf{r}_\mathrm{d},\mathbf{r}_1,\omega_1)\right)^*\mathbf{e}_1 e^{-i\Omega_- t}\Theta(t)\,b^\dagger(0) \tag{G.3}$$

and we note that $\mathbf{E}^-(\mathbf{r}_\mathrm{d},t) = (\mathbf{E}^+(\mathbf{r}_\mathrm{d},t))^\dagger$, so that $\mathbf{E}(\mathbf{r}_\mathrm{d},t) = \mathbf{E}^+(\mathbf{r}_\mathrm{d},t)+\mathbf{E}^-(\mathbf{r}_\mathrm{d},t)$ is Hermitian. Given the initial condition $|\Psi(t=0)\rangle = b^\dagger(0)|\mathcal{F}\rangle$, we can now calculate the expectation value of the intensity operator

$$\langle I(\mathbf{r}_\mathrm{d},t)\rangle = \langle\mathbf{E}^+(\mathbf{r}_\mathrm{d},t)\cdot\mathbf{E}^-(\mathbf{r}_\mathrm{d},t)\rangle = S_1(\omega_1)^2|\mathbf{G}^\mathrm{B}(\mathbf{r}_\mathrm{d},\mathbf{r}_1,\omega_1)\mathbf{e}_1|^2\,e^{-2X_1(\omega_1)t},$$

which shows an exponential decay with the decay rate $\Gamma = 2X_1(\omega_1)$, as expected.

Last, we test the validity of the assumption that X_1 is small compared to ω_1. For $\lambda_1 = 980\,\mathrm{nm}$ we have $\omega_1 = 1.92 \times 10^{15}\,\mathrm{s}^{-1}$ and given typical QD radiative decay rates in a homogeneous medium on the order of 1 ns we get

$$\frac{X_1(\omega_1)}{\omega_1} \approx \frac{0.5 \times 10^9\,\mathrm{s}^{-1}}{1.92 \times 10^{15}\,\mathrm{s}^{-1}} \approx 2.5 \times 10^{-7},$$

which underscores the validity of the approximations made.

G.2 Two quantum dots

Including an additional QD in the structure, we have from Eq. (5.2) :

$$\begin{aligned}\mathbf{E}(\mathbf{r}_\mathrm{d}) &= \Big(\mathbf{G}^{(1)}(\mathbf{r}_\mathrm{d},\mathbf{r}_1) + \mathbf{G}^{(1)}(\mathbf{r}_\mathrm{d},\mathbf{r}_2)\mathbf{U}_2\mathbf{G}^{(2)}(\mathbf{r}_2,\mathbf{r}_1)\Big)\,\mathbf{S}_1 \\ &= \mathbf{E}^\mathrm{D}(\mathbf{r}_\mathrm{d}) + \mathbf{E}^\mathrm{S}(\mathbf{r}_\mathrm{d}).\end{aligned}$$

The first term is exactly the direct term and we interpret the second term as arising from scattering off QD 2 before arriving at the detector, cf. Fig. 5.8.

Introducing the notation

$$G_{ab} = \mathbf{e}_a\mathbf{G}^\mathrm{B}(\mathbf{r}_a,\mathbf{r}_b)\mathbf{e}_b,$$

we rewrite the expression for the scattered field in terms of the background Green's tensors as

$$\begin{aligned}\mathbf{E}^\mathrm{S}(\mathbf{r}_\mathrm{d}) = &\frac{\mathbf{G}^\mathrm{B}(\mathbf{r}_\mathrm{d},\mathbf{r}_2)\mathbf{e}_2U_2G_{21}S_1}{(1-G_{11}U_1)(1-G_{22}U_2)-G_{21}U_1G_{12}U_2} \\ &+ \frac{\mathbf{G}^\mathrm{B}(\mathbf{r}_\mathrm{d},\mathbf{r}_1)\mathbf{e}_2U_1G_{12}U_2G_{21}S_1}{(1-G_{11}U_1)\big((1-G_{11}U_1)(1-G_{22}U_2)-G_{21}U_1G_{12}U_2\big)},\end{aligned}$$

from which we see that the scattered field itself consists of two terms; one term, $\mathbf{E}_2^\mathrm{S}$, that scatters off QD 2 before arriving at the detector and another term, $\mathbf{E}_{21}^\mathrm{S}$, that first scatters off QD 2 and then back to QD 1 before arriving at the detector.

Calculation of $\mathbf{E}_2^\mathrm{S}(\mathbf{r}_\mathrm{d},t)$

Similar to the calculations for the direct term, we rewrite $\mathbf{E}_2^\mathrm{S}(\mathbf{r}_\mathrm{d},t)$ as

$$\mathbf{E}_2^\mathrm{S}(\mathbf{r}_\mathrm{d},\omega) = \frac{(\omega_1^2-\omega^2)\mathbf{G}^\mathrm{B}(\mathbf{r}_\mathrm{d},\mathbf{r}_2,\omega)\mathbf{e}_2 2\omega_2 J_{21}(\omega)S_1(\omega)}{(\omega_1^2-\omega^2-2\omega_1X_1(\omega))(\omega_2^2-\omega^2-2\omega_2X_2(\omega))-4\omega_1\omega_2J_{21}(\omega)J_{12}(\omega)},$$

where $J_{ab} = U_a G_{ab}$ is different by a factor of d_a/d_b from the similar parameter in Ref. [48].

Unlike Ref. [48] we will allow for a detuning of the resonance frequencies of the two dots, so that $\omega_2 = \omega_1 + \Delta\omega$. In this case, the poles Ω appear as the solutions to the equation

$$(\omega_1^2 - \Omega^2)^2 + b(\omega_1^2 - \Omega^2) + c = 0,$$

where the parameters b and c are given as

$$b = -2\omega_1 \left(X_1 + X_2 - \Delta\omega - \frac{\Delta\omega(\Delta\omega - 2X_2)}{2\omega_1} \right)$$
$$c = 4\omega_1^2 \left(X_1 X_2 - X_1 \Delta\omega - J_{12}J_{21} - \frac{X_1 \Delta\omega(\Delta\omega - 2X_2)}{2\omega_1} - \frac{\Delta\omega}{\omega_1} J_{12}J_{21} \right).$$

The equation may be directly solved to yield two positive frequency poles and two negative frequency poles,

$$\Omega_1 = \omega_1 + \gamma_1 - i\frac{\Gamma_1}{2} \tag{G.4a}$$
$$\Omega_2 = \omega_2 + \gamma_2 - i\frac{\Gamma_2}{2} \tag{G.4b}$$
$$\Omega_3 = -\omega_1 + \gamma_3 - i\frac{\Gamma_3}{2} \tag{G.4c}$$
$$\Omega_4 = -\omega_2 + \gamma_4 - i\frac{\Gamma_4}{2}, \tag{G.4d}$$

where now both γ_n and Γ_n are small compared to ω_1 or ω_2. As in the one QD case, all poles have negative imaginary parts. Unlike the one QD case, however, the real parts are shifted slightly from the values of the bare frequencies due to the interaction term. For $J_{12} = J_{21} = 0$ we recover the poles from the one QD case with real parts equal to $\pm\omega_1$ and $\pm\omega_2$. In the case of zero detuning we recover the results of Ref. [48]. The $\mathbf{E}_2^{\mathrm{S}}$ term is now written as

$$\mathbf{E}_2^{\mathrm{S}}(\mathbf{r}_{\mathrm{d}}, \omega) = \frac{-(\omega^2 - \omega_1^2)\mathbf{G}^{\mathrm{B}}(\mathbf{r}_{\mathrm{d}}, \mathbf{r}_2, \omega)\mathbf{e}_2 2\omega_2 J_{21}(\omega) S_1(\omega)}{(\omega - \Omega_1)(\omega - \Omega_2)(\omega - \Omega_3)(\omega - \Omega_4)} \left[\frac{b(0)}{(\omega - \omega_1)} + \frac{b^\dagger(0)}{(\omega + \omega_1)} \right],$$
$$= -\mathbf{G}^{\mathrm{B}}(\mathbf{r}_{\mathrm{d}}, \mathbf{r}_2, \omega)\mathbf{e}_2 2\omega_2 J_{21}(\omega) S_1(\omega) \left\{ \sum_{n=1}^{4} \frac{\alpha_n}{\omega - \Omega_n} \right\}$$
$$\times \left[(\omega + \omega_1) b(0) + (\omega - \omega_1) b^\dagger(0) \right],$$

where

$$\alpha_n = \prod_{\substack{m=1 \\ m \neq n}}^{4} \frac{1}{\Omega_n - \Omega_m}.$$

Similar to the one QD case, the terms proportional to $b^\dagger(0)$ have vanishing residue at the positive frequency poles Ω_1 and Ω_2, and the terms proportional to $b(0)$ have vanishing residues at the negative frequency poles Ω_3 and Ω_4. Therefore, we may write for the positive frequency part:

$$\begin{aligned}\mathbf{E}_2^{\mathrm{S}+}(\mathbf{r}_\mathrm{d},t) &= -\frac{1}{2\pi}\int_{-\infty}^{\infty}\left\{\frac{\alpha_1}{\omega-\Omega_1}+\frac{\alpha_2}{\omega-\Omega_2}\right\}\mathbf{G}^\mathrm{B}(\mathbf{r}_\mathrm{d},\mathbf{r}_2,\omega)\mathbf{e}_2 2\omega_2 J_{21}(\omega)S_1(\omega)\\ &\quad\times(\omega+\omega_1)b(0)e^{-i\omega t}\mathrm{d}\omega\\ &= i2\omega_2\sum_{n=1}^{2}\alpha_n\mathbf{G}^\mathrm{B}(\mathbf{r}_\mathrm{d},\mathbf{r}_2,\Omega_n)\mathbf{e}_2 J_{21}(\Omega_n)S_1(\Omega_n)(\Omega_n+\omega_1)b(0)e^{-i\Omega_n t}.\end{aligned}$$

As in the one QD case we have $\mathbf{E}_2^{\mathrm{S}-}(\mathbf{r}_\mathrm{d},t)=(\mathbf{E}_2^{\mathrm{S}+}(\mathbf{r}_\mathrm{d},t))^\dagger$.

It is illustrative to consider the behavior of $\mathbf{E}_2^{\mathrm{S}+}(\mathbf{r}_\mathrm{d},t)$ for small detunings $\Delta\omega$ compared to ω_1. In this case we may substitute ω_1 for Ω_n in the slowly varying functions $\mathbf{G}^\mathrm{B}(\mathbf{r}_\mathrm{d},\mathbf{r}_2,\Omega_n)$, $J_{21}(\Omega_n)$ and $S_1(\Omega_n)$. We may further substitute $2\omega_1$ for $(\Omega_n-\Omega_3)$ and $(\Omega_n-\Omega_4)$ to arrive at the somewhat simpler expression

$$\begin{aligned}\mathbf{E}_2^{\mathrm{S}+}(\mathbf{r}_\mathrm{d},t) &\approx i\frac{\omega_2}{\omega_1}\mathbf{G}^\mathrm{B}(\mathbf{r}_\mathrm{d},\mathbf{r}_2,\omega_1)\mathbf{e}_2 J_{21}(\omega_1)S_1(\omega_1)b(0)\frac{e^{-i\Omega_1 t}-e^{-i\Omega_2 t}}{\Omega_1-\Omega_2}\\ &= i\frac{\omega_2}{\omega_1}\mathbf{G}^\mathrm{B}(\mathbf{r}_\mathrm{d},\mathbf{r}_2,\omega_1)\mathbf{e}_2 J_{21}(\omega_1)S_1(\omega_1)b(0)\left(t+\mathcal{O}(t^2)\right),\end{aligned}\qquad(\mathrm{G}.5)$$

which shows that for small detunings $\Delta\omega$ compared to ω_1 the time dependence is linear in t for small times . At longer times, the exponential decay due to the imaginary parts of the exponents dominates the time dependence.

Calculation of $\mathbf{E}_{21}^{\mathrm{S}}(\mathbf{r}_\mathrm{d},t)$

Following a similar approach as for the $\mathbf{E}_2^{\mathrm{S}}(\mathbf{r}_\mathrm{d},t)$ term we first write

$$\begin{aligned}\mathbf{E}_{21}^{\mathrm{S}}(\mathbf{r}_\mathrm{d},\omega) &= \frac{(\omega^2-\omega_1^2)\mathbf{G}^\mathrm{B}(\mathbf{r}_\mathrm{d},\mathbf{r}_1,\omega)\mathbf{e}_1 J_{12}(\omega)2\omega_1 J_{21}(\omega)2\omega_2}{(\omega-\Omega_+)(\omega-\Omega_-)(\omega-\Omega_1)(\omega-\Omega_2)(\omega-\Omega_3)(\omega-\Omega_4)}\\ &\quad\times S_1(\omega)\left[\frac{b(0)}{(\omega-\omega_1)}+\frac{b^\dagger(0)}{(\omega+\omega_1)}\right],\end{aligned}$$

where $\Omega_\pm$ are given in Eq. (G.1) and Ω_n are given in Eqs. (G.4). Defining $\Omega_0=\Omega_+$ and $\Omega_5=\Omega_-$ we may write the expression compactly as

$$\begin{aligned}\mathbf{E}_{21}^{\mathrm{S}}(\mathbf{r}_\mathrm{d},\omega) &= \mathbf{G}^\mathrm{B}(\mathbf{r}_\mathrm{d},\mathbf{r}1,\omega)\mathbf{e}_1 J_{12}(\omega)2\omega_1 J_{21}(\omega)2\omega_2\left\{\sum_{n=0}^{5}\frac{\alpha_n}{\omega-\Omega_n}\right\}\\ &\quad\times S_1(\omega)\left[(\omega+\omega_1)b(0)+(\omega-\omega_1)b^\dagger(0)\right],\end{aligned}$$

with

$$\alpha_n = \prod_{\substack{m=0 \\ m\neq n}}^{5} \frac{1}{\Omega_n - \Omega_m}.$$

As before, the terms proportional to $b(0)$ have vanishing residue at the negative frequency poles, and so we may write

$$\begin{aligned}
\mathbf{E}_{21}^{\mathrm{S}+}(\mathbf{r}_\mathrm{d}, t) &= \frac{1}{2\pi}\int_{-\infty}^{\infty}\sum_{n=0}^{2}\frac{\alpha_n}{\omega-\Omega_n}\mathbf{G}^\mathrm{B}(\mathbf{r}_\mathrm{d},\mathbf{r}_1,\omega)\mathbf{e}_1 J_{12}(\omega)2\omega_1 J_{21}(\omega)2\omega_2 \\
&\quad\times S_1(\omega)(\omega+\omega_1)b(0)e^{-i\omega t}\mathrm{d}\omega \\
&= -i4\omega_1\omega_2\sum_{n=0}^{2}\alpha_n\mathbf{G}^\mathrm{B}(\mathbf{r}_\mathrm{d},\mathbf{r}_1,\Omega_n)\mathbf{e}_1 J_{12}(\Omega_n)J_{21}(\Omega_n). \\
&\quad\times S_1(\Omega_n)(\Omega_n+\omega_1)b(0)e^{-i\Omega_n t}. \qquad \text{(G.6)}
\end{aligned}$$

Since $|\Omega_n| - \omega_1$ is small compared to ω_1 we may again substitute ω_1 for Ω_n in the slowly varying terms as well as substitute $2\omega_1$ for $(\omega_n - \Omega_3)$, $(\omega_n - \Omega_4)$ and $(\omega_n - \Omega_5)$. In this way we write

$$\begin{aligned}
\mathbf{E}_{21}^{\mathrm{S}+}(\mathbf{r}_\mathrm{d}, t) &\approx -i\frac{\omega_2}{\omega_1}\mathbf{G}^\mathrm{B}(\mathbf{r}_\mathrm{d},\mathbf{r}1,\omega_1)\mathbf{e}_1 J_{12}(\omega_1)J_{21}(\omega_1)\sum_{n=0}^{2}e^{-i\Omega_n t}\prod_{\substack{m=0\\m\neq n}}^{2}\frac{1}{\Omega_n-\Omega_m} \\
&= i\frac{\omega_2}{\omega_1}\mathbf{G}^\mathrm{B}(\mathbf{r}_\mathrm{d},\mathbf{r}1,\omega_1)\mathbf{e}_1 J_{12}(\omega_1)J_{21}(\omega_1)\left(t^2+\mathcal{O}(t^3)\right). \qquad \text{(G.7)}
\end{aligned}$$

Comparing to $\mathbf{E}_2^{\mathrm{S}+}(\mathbf{r}, t$, Eq. (G.5), we see that $\mathbf{E}_{21}^{\mathrm{S}+}$ may be important for the dynamics, since $J_{21}(\omega_1)t^2$ may be is smaller than t, but not negligible, within the lifetime of typical quantum dots.

Appendix H

Finite difference time-domain calculations

In this appendix we discuss details concerning the FDTD calculations of the electric field Green's tensor in section 5.2. The basic idea behind the approach derives directly from the interpretation of the Green's tensor $\mathbf{G}(\mathbf{r}, \mathbf{r}', \omega)$ as the electric field at the position $\mathbf{r}$ due to a point source at position $\mathbf{r}'$, as discussed in section 2.2.1. From Eq. (2.12) we get an expression for the Green's tensor in the frequency domain. Since FDTD is a time-domain method, we apply a Fourier transform to arrive at a final expression, suitable for FDTD calculations:

$$\mathbf{G}(\mathbf{r}, \mathbf{r}', \omega) = \frac{\epsilon_0 \mathbf{E}(\mathbf{r}, \omega)}{k_0^2 \mathbf{d}(\omega)} = \frac{\epsilon_0}{k_0^2} \frac{\mathrm{FFT}\{\mathbf{E}(\mathbf{r}, t)\}}{\mathrm{FFT}\{\mathbf{d}(t)\}}, \tag{H.1}$$

in which FFT denotes the Fast Fourier Transform, and $\mathbf{E}(\mathbf{r}, t)$ is the electric field at point $\mathbf{r}$ from the dipole $\mathbf{d}(t)$ located at $\mathbf{r}'$.

H.1 Implementation

The calculations were carried out using the commercial FDTD software FDTD solutions from Lumerical Inc. In FDTD we defined a dipole point source, $\mathbf{P}_{\mathrm{ex}}(\mathbf{r}, t) = \mathbf{d}(t)\delta(\mathbf{r} - \mathbf{r}_0)$, with time-dependent dipole moment $\mathbf{d}(t)$. We excited the system with a pulse at time t_0 and evolved the system in time, recording at every time step the values of the electric field at pre-defined detector positions within the calculation domain.

The calculation domain was defined as in Fig. 5.1 with Perfectly Matched Layers (PML) as boundaries. The crystallite was fully contained within the calculation

domain with a few calculation cells of spacing between the outermost air holes and the boundary. The membrane extended through the PMLs, so that the model in effect consisted of an infinite membrane with a single crystallite. An averaging of the refractive index was used for cells along the edge of air holes.

Source

We used a Gaussian pulse,

$$\mathbf{d}_0(t) = \mathbf{e}_0 A \exp\left(\frac{-(t-t_0)^2}{2\sigma^2}\right) \sin\left(\omega_0(t-t_0)\right),$$

with a frequency $\omega_0 = 1.922{\times}10^{15}\,\mathrm{s}^{-1}$ (corresponding to 980 nm as used in Ref. [23]) and oscillating in the direction $\mathbf{e}_0$. The parameter A ensures that the δ-function is properly normalized. In a straight forward numerical implementation, the dipole moment $\mu(\omega)$ would be taken to be constant over a single cell and the delta function would be a Kronecker delta. Thus, for the dipole in cell n we would have

$$\mathbf{P}_{\mathrm{num}}(t) = \delta_{m,n}\frac{\mathbf{d}(t)}{V_{\mathrm{cell}}},$$

from which we see that the volume of the cell needs to be properly accounted for in order to use Eq. (H.1) directly. For the calculations we used $\sigma = 3.89{\times}10^{-15}\,\mathrm{s}$, corresponding to a bandwidth of $\Delta\omega_{\mathrm{BW}} = 6.06{\times}10^{14}\,\mathrm{s}^{-1}$. From Eq. (H.1) we expect the numerical Green's tensor to be independent of the exact shape of the pulse as long as the bandwidth is sufficiently large. We have verified that the calculated LDOS is independent of the center frequency within the bandwidth of the initial pulse.

Discretization

In FDTD the space is discretized into Yee cells. These are in general parallelepipeds, and for the calculations on photonic crystals we chose Δx_i so that the lattice constant of the PC in the direction x_i was an integer number of Δx_i. As a rule of thumb, we chose the discretization in media of refractive index n_{R} sufficiently small that $\lambda_0/n_{\mathrm{R}} < 20\Delta x_i$. The time discretization is intimately linked to the space discretization through the Courant stability condition,

$$c\Delta t \leq \frac{1}{\sqrt{1/\Delta x^2 + 1/\Delta y^2 + 1/\Delta z^2}},$$

where c is the speed of light. Typically, we worked close to the maximum time step and chose

$$c\Delta t = 0.99\frac{\Delta}{\sqrt{3}},$$

where $\Delta = \max\{\Delta x, \Delta y, \Delta z\}$. Working with smaller Yee cells results in less numerical dispersion at the price of larger calculation times. Due to the FDTD algorithm, the total runtime for simulations will typically scale linearly with both the number of grid points and the number of time steps, so that

$$T \approx k_T N_{\text{cells}} \times N_{\text{time}},$$

where the constant $k_T \approx 1\,\mu$s for the computer used for the calculations in this work.

H.2 Accuracy

In order to assess the reliability of the calculations we compare the numerical FDTD Green's tensor to analytical results for bulk media. The left panel of Fig. H.1 shows the relative error on the LDOS in a bulk medium of refractive index $n_{\text{R}} = 3.52$ as a function of normalized frequency. The bandwidth of the source is indicated by the dashed curve. Results are shown for different choices of discretization, illustrating how the discretization controls the error as expected.

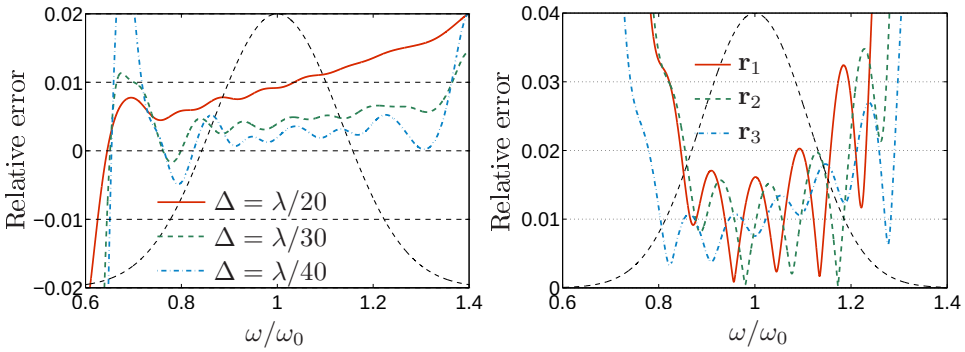

Figure H.1: Left: Relative error in the LDOS calculations $(Im\{G_{xx}^{num}(0,0)\} - Im\{G_{xx}(0,0)\})/Im\{G_{xx}(0,0)\}$ *as a function of normalized frequency and for different discretizations* Δ *as indicated. Right: Relative error on the non-local elements* $|G_{xx}^{num}(0,\mathbf{r}) - G_{xx}(0,\mathbf{r})|/|G_{xx}(0,\mathbf{r})|$*, for the points* $\mathbf{r}_1 = (\lambda, 0, 0)$*,* $\mathbf{r}_2 = (\lambda, \lambda, 0)$ *and* $\mathbf{r}_1 = (0, \lambda, 0)$*.*

In order to assess the reliability of non-local calculations, we show in the right panel of Fig. H.1 the relative error on the $G_{xx}(0,\mathbf{r})$ element of the Green's tensor for three different positions relative to the origin and for $\Delta = \lambda/30$. The figure shows a slightly larger relative error than for the LDOS calculations.

Whereas the homogeneous material are the simplest to handle analytically, they are likely among the hardest material systems for this kind of Green's tensor calculations using FDTD, since ideally there are no reflections. In practice there will always be tiny reflections from the PMLs at the calculation domain boundaries, but for the PC calculations these were likely much smaller than the response of the system due to the scattering in the PC itself. The error in the homogeneous material case therefore represents the worst case error, and as a conservative estimate we expect the relative error in the calculations to be less than 5%.

Bibliography

[1] Stobbe, S., Johansen, J., Kristensen, P. T., Hvam, J. M. & Lodahl, P. *Frequency dependence of the radiative decay rate of excitons in self-assembled quantum dots: Experiment and theory.* Physical Review B **80**, 155307 (2009).

[2] Lakowicz, J. R. *Principles of Fluorescence Spectroscopy, third edition* (Springer, 2006).

[3] Purcell, E. M. *Spontaneous Emission Probabilities at Radio Frequencies.* Physical Review **69**, 681 (1946).

[4] Drexhage, K. H. *Influence of a dielectric interface on fluorescence decay time.* Journal of Luminescence **1,2**, 693–701 (1970).

[5] Johansen, J., Stobbe, S., Nikolaev, I. S., Lund-Hansen, T., Kristensen, P. T., Hvam, J. M., Vos, W. L. & Lodahl, P. *Size dependence of the wavefunction of self-assembled InAs quantum dots from time-resolved optical measurements.* Physical Reviw B **77**, 073303 (2008).

[6] Saleh, B. E. A. & Teich, M. C. *Fundamentals of Photonics* (Wiley-Interscience, 1991).

[7] Bykov, V. P. *Spontaneous emission from a medium with a band spectrum.* Soviet Journal of Quantum Electronics **4**, 861–871 (1975).

[8] Yablonovitch, E. *Inhibited spontaneous emission in solid-state physics and electronics.* Physical Review Letters **58**, 2059–2062 (1987).

[9] John, S. *Strong localization of photons in certain disordered dielectric superlattices.* Physical Review Letters **58**, 2486–2489 (1987).

[10] Wijnhoven, J. E. G. J. & Vos, W. L. *Preparation of Photonic Crystals Made of Air Spheres in Titania.* Science **281**, 802–804 (1998).

[11] Aoki, K., Miyazaki, H., Hirayama, H., Inoshita, K., Baba, T., Sakoda, K., Shinya, N. & Aoyagi, Y. *Microassembly of semiconductor three-dimensional photonic crystals.* Nature materials **2**, 117–121 (2003).

[12] Yablonovitch, E., Gmitter, T. J. & Leung, K. M. *Photonic band structure: The face-centered-cubic case employing nonspherical atoms.* Physical Review Lett. **67**, 2295–2298 (1991).

[13] Cuisin, C., Chelnokov, A., Decanini, D., Peyrade, D., Chen, Y. & Lourtioz, J. M. *Sub-micrometre dielectric and metallic yablonovite structures fabricated from resist templates.* Optical and Quantum Electronics **34**, 13–26 (2002).

[14] Einstein, A. *Zur Quantentheorie der Strahlung.* Physikalische Zeitschrift **12**, 121–128 (1917).

[15] Dirac, P. A. M. *The Quantum Theory of the Emission and Absorption of Radiation.* Proceedings of the Royal Society of London **114**, 243–265 (1927).

[16] Weisskopf, V. & Wigner, E. *Berechnung der natürlichen Linienbreite auf Grund der Diracschen Lichttheorie.* Zeitschrift für Physik **63**, 54–73 (1930).

[17] Sprik, R., van Tiggelen, B. A. & Lagendijk, A. *Optical emission in periodic dielectrics.* Europhysics Letters **35**, 265–270 (1996).

[18] Claude Weisbuch, R. H. & Stanley, R. P. *Spontaneous emission and laser oscillations in microcavities* (CRC Press, 2000).

[19] Nabiev, R. F., Yeh, P. & Sanchez-Mondragon, J. J. *Dynamics of the spontaneous emission of an atom into the photon-density-of-states gap: Solvable quantum-electrodynamical model.* Physical Review A **47**, 3380–3384 (1993).

[20] John, S. & Quang, T. *Spontaneous emission near the edge of a photonic band gap.* Physical Review A **50**, 1764–1769 (1994).

[21] Lodahl, P., van Driel, A. F., Nikolaev, I. S., Irman, A., Overgaag, K., Vanmaekelbergh, D. & Vos, W. L. *Controlling the dynamics of spontaneous emission from quantum dots by photonic crystals.* Nature **430**, 654–657 (2004).

[22] Fujita, M., Takahashi, S., Tanaka, Y., Asano, T. & Noda, S. *Simultaneous Inhibition and Redistribution of Spontaneous Light Emission in Photonic Crystals.* Science **308**, 1296–1298 (2005).

[23] Julsgaard, B., Johansen, J., Stobbe, S., Stolberg-Rohr, T., Sünner, T., Kamp, M., Forchel, A. & Lodahl, P. *Decay dynamics of quantum dots influenced by the local density of optical states of two-dimensional photonic crystal membranes.* Applied Physics Letters **93**, 094102 (2008).

[24] Vahala, K. J. *Optical microcavities.* Nature **424**, 839–846 (2003).

[25] Gérard, J. M., Sermage, B., Gayral, B., Legrand, B., Costard, E., & Thierry-Mieg, V. *Enahnced Spontaneous Emission by Quantum Boxes in a Monolithic Optical Microcavity.* Physical Review Letters **81**, 1110–1113 (1998).

[26] Yoshie, T., Scherer, A., Hendrickson, J., Khitrova, G., Gibbs, H. M., Rupper, G., Ell, C., Shchekin, O. B. & Deppe, D. G. *Vacuum Rabi splitting with a single quantum dot in a photonic crystal nanocavity.* Nature **432**, 200–203 (2004).

[27] Reithmaier, J. P., Sek, G., Löffler, A., Hofmann, C., Kuhn, S., Reitzenstein, S., Keldysh, L. V., Kulakovskii, V. D., Reinecke, T. L. & Forchel, A. *Strong coupling in a single quantum dot-semiconductor microcavity system.* Nature **432**, 197–200 (2004).

[28] Hennessy, K., Badolato, A., Wigner, M., Greace, D., Atatüre, M., gulde, S., Fält, S., Hu, E. L. & Imamoglu, A. *Quantum nature of a strongly coupled single quantum dot-cavity system.* Nature **445**, 896–899 (2007).

[29] Næsby, A., Suhr, T., Kristensen, P. T. & rk, J. M. *Influence of pure dephasing on emission spectra from single photon sources.* Physical Review A **78**, 045802 (2008).

[30] Auffèves, A., Besga, B., Gérard, J.-M. & Poizat, J.-P. *Spontaneous emission spectrum of a two-level atom in a very-high-Q cavity.* Physical Review A **77**, 063833 (2008).

[31] Laussy, F. P., del Valle, E. & Tejedor, C. *Luminescence spectra of quantum dots in microcavities. I. Bosons.* Physical Review B **79**, 235325 (2009).

[32] Bennett, C. H., Bessette, F., Brassard, G., Salvail, L. & Smolin, J. A. *Experimental Quantum Cryptography.* Journal of Cryptology **5**, 3–28 (1992).

[33] Kimble, H. J. *The quantum internet.* Nature **453**, 1023–1030 (2008).

[34] Intallura, P. M., Ward, M. B., Karimov, O. Z., Yuan, Z. L., See, P., Shields, A. J., Atkinson, P. & Ritchie, D. A. *Quantum key distribution using a triggered quantum dot source emitting near 1.3 mu m.* Applied Physics Letters **91**, 161103 (2007).

[35] Rao, V. S. C. M. & Hughes, S. *Single Quantum Dot Spontaneous Emission in a Finite-Size Photonic Crystal Waveguide: Proposal for an Efficient "On Chip" Single Photon Gun.* Physical Review Letters **99**, 193901 (2007).

[36] Lecamp, G., Lalanne, P. & Hugonin, J. P. *Very Large Spontaneous-Emission beta Factors in Photonic-Crystal Waveguides.* Physical Review Letters **99**, 023902 (2007).

[37] Lund-Hansen, T., Stobbe, S., Julsgaard, B., Thyrrestrup, H., Sünner, T., Kamp, M., Forchel, A. & Lodahl, P. *Experimental Realization of Highly Efficient Broadband Coupling of Single Quantum Dots to a Photonic Crystal Waveguide.* Physical Review Letters **101**, 113903 (2008). URL `http://link.aps.org/abstract/PRL/v101/e113903`.

[38] Ekert, A. K. *Quantum cryptography based on Bell's theorem.* Phys. Rev. Lett. **67**, 661–663 (1991).

[39] Jennewein, T., Simon, C., Weihs, G., Weinfurter, H. & Zeilinger, A. *Quantum Cryptography with Entangled Photons.* Phys. Rev. Lett. **84**, 4729–4732 (2000).

[40] Pittman, T. B., Shih, Y. H., Strekalov, D. V. & Sergienko, A. V. *Optical imaging by means of two-photon quantum entanglement.* Physical Review A **52**, R3429–R3432 (1995).

[41] Lugiato, L. A., Gatti, A. & Brambilla, E. *Quantum imaging.* Journal of Optics B **4**, S176–S183 (2002).

[42] Bennett, C. H., Brassard, G., Crépeau, C., Jozsa, R., Peres, A. & Wootters, W. K. *Teleporting an unknown quantum state via dual classical and Einstein-Podolsky-Rosen channels.* Phys. Rev. Lett. **70**, 1895–1899 (1993).

[43] Knill1, E., Laflamme, R. & Milburn, G. J. *A scheme for efficient quantum computation with linear optics.* Nature **409**, 46–52 (2001).

[44] OŠBrien, J. L., Pryde, G. J., White, A. G., Ralph, T. C. & Branning, D. *A scheme for efficient quantum computation with linear optics.* Nature **426**, 264–267 (2003).

[45] Pathak, P. K. & Hughes, S. *Cavity-assisted fast generation of entangled photon pairs through the biexciton-exciton cascade.* Physical Review B **80**, 155325 (2009).

[46] Stevenson, R. M., Thompson, R. M., Shields, A. J., Farrer, I., Kardynal, B. E., Ritchie, D. A. & Pepper, M. *Quantum dots as a photon source for passive quantum key encoding.* Physical Review B (R) **66**, 081302 (2002).

[47] Levine, H. & Schwinger, J. *On the theory of diffraction by an aperture in an infinite plane screen. I.* Physical Review **8**, 958–974 (1948).

[48] Wubs, M., Suttorp, L. G. & Lagendijk, A. *Multiple-scattering approach to interatomic interactions and superradiance in inhomogeneous dielectrics.* Physical Review A **70**, 053823 (2004).

[49] Tai, C.-T. *Dyadic Green Functions in Electromagnetic Theory* (IEEE Press, 1994).

[50] Novotny, L. & Hecht, B. *Principles of Nano Optics* (Cambridge University Press, 2006).

[51] Martin, P. *Multiple Scattering. Interaction of time-harmonic waves with N obstacles* (Cambridge University Press, 2006).

[52] Li, L.-W., Kooi, P.-S., Leong, M.-S. & Yeo, T.-S. *Electromagnetic Dyadic Green's Function in Spherically Multilayered Media.* IEEE Transactions on Microwave Theory and Techniques **42**, 2302 (1994).

[53] Paulus, M., Gay-Balmaz, P. & Martin, O. J. F. *Accurate and efficient computation of the Green's tensor for stratified media.* Physical Review E **62**, 5797–5807 (2000).

[54] Paulus, M. & Martin, O. J. F. *Green's tensor technique for scattering in two-dimensional stratified media.* Physical Review E **63**, 066615 (2001).

[55] Martin, O. J. F. & Piller, N. B. *Electromagnetic scattering in polarizable backgrounds.* Physical Review E **58**, 3909–3915 (1998).

[56] Hughes, S. & Yao, P. *Theory of quantum light emission from a strongly-coupled single quantum dot photonic crystal cavity system.* Optics Express **17**, 3322 (2009).

[57] Yao, P. & Hughes, S. *Macroscopic entanglement and violation of Bell's inequalities between two spatially separated quantum dots in a planar photonic crystal system.* Optics Express **17**, 11505 (2009).

[58] Arfken, G. B. & Weber, H. J. *Mathematical Methods for Physicists, fifth edition* (Academic Press, 2001).

[59] Yaghjian, A. D. *Electric Dyadic Green's Functions in the Source Region.* Proceedings IEEE **68**, 248–263 (1980).

[60] Vogel, W., Welsch, D.-G. & Wallentowitz, S. *Quantum Optics An Introduction, Second editoin* (Wiley, 2001).

[61] Craig, D. P. & Thirunamachandran, T. *Molecular Quantum Electrodynamics* (Dover, 1984).

[62] Vats, N., John, S. & Busch, K. *Theory of fluorescence in photonic crystals.* Physical Review A **65**, 043808 (2002).

[63] Gerry, C. C. & Knight, P. L. *Introductory Quantum Optics* (Cambridge Univesity Press, 2005).

[64] Joannopoulos, J. D., Johnson, S. G., Winn, J. N. & Meade, R. D. *Photonic Crystals - Molding the Flow of Light, second edition.* (Princeton University Press, 2008).

[65] Tavlove, A. *Computational Electromagnetics: The Finite-difference time-domain method* (Artech House, 1995).

[66] Sullivan, D. M. & Citrin, D. S. *Determining quantum eigenfunctions in three-dimensional nanoscale structures.* Journal of Applied Physics **97**, 104305 (2005).

[67] Rao, V. S. C. M. & Hughes, S. *Single quantum-dot Purcell factor and β factor in a photonic crystal waveguide.* Physical Review B **75**, 205437 (2007).

[68] Koenderink, A. F., Kafesaki, M., Soukoulis, C. M. & Sandoghdar, V. *Spontaneous emission rates of dipoles in photonic crystal membranes.* Journal of the Optical Society of America B **23**, 1196–1206 (2006).

[69] Leung, K. M. & Liu, Y. F. *Full vector wave calculation of photonic band structures in face-centered-cubic dielectric media.* Physical Review Letters **65**, 2646–2649 (1990).

[70] Johnson, S. G. & Joannopoulos, J. D. *Block-iterative frequency-domain methods for Maxwell's equations in a planewave basis.* Opt. Express **8**, 173–190 (2001).

[71] Johnson, S. G., Fan, S., Villeneuve, P. R., Joannopoulos, J. D. & Kolodziejski, L. A. *Guided modes in photonic crystal slabs.* Physical Review B **60**, 5751–5758 (1999).

[72] Busch, K. & John, S. *Photonic band gap formation in certain self-organizing systems.* Physical Review E **58**, 3896–3908 (1998).

[73] Wang, R., Wang, X.-H., Gu, B.-Y. & Yang, G.-Z. *Local density of states in three-dimensional photonic crystals: Calculation and enhancement effects.* Physical Review B **67**, 155114 (2003).

[74] Nikolaev, I. S., Vos, W. L. & Koenderink, A. F. *Accurate calculation of the local density of optical states in inverse-opal photonic crystals.* Journal of the Optical Society of America B **26**, 987/997 (2009).

[75] Hafner, C. *The Generalized Multipole Technique for Computational Electromagnetics* (Artech House, 1990).

[76] White, T. P., Kuhlmey, B. T., McPhedran, R. C., Maystre, D., Renversez, G., de Sterke, C. M. & Botten, L. C. *Multipole method for microstructured optical fibers. I. Formulation.* Journal of the Optical Society of America B **19**, 2322–2330 (2002).

[77] White, T. P., Kuhlmey, B. T., McPhedran, R. C., Maystre, D., Renversez, G., de Sterke, C. M. & Botten, L. C. *Multipole method for microstructured optical fibers. I. Formulation: errata.* Journal of the Optical Society of America B **20**, 1581–1581 (2003).

[78] Kuhlmey, B. T., White, T. P., Renversez, G., Maystre, D., Botten, L. C., de Sterke, C. M. & McPhedran, R. C. *Multipole method for microstructured optical fibers. II. Implementation and results.* Journal of the Optical Society of America B **19**, 2331–2340 (2002).

[79] Campbell, S., McPhedran, R. C., de Sterke, C. M. & Botten, L. C. *Differential multipole method for microstructured optical fibers.* Journal of the Optical Society of America B **21**, 1919–1928 (2004).

[80] Asatryan, A. A., Busch, K., McPhedran, R. C., Botten, L. C., de Sterke, C. M. & Nicorovici, N. A. *Two-dimensional Green tensor and local density of states in finite-sized two-dimensional photonic crystals.* Waves in Random Media **13**, 9–25 (2003).

[81] Fussell, D. P., McPhedran, R. C. & de Sterke, C. M. *Three-dimensional Green's tensor, local density of states, and spontaneous emission in finite two-dimensional photonic crystals composed of cylinders.* Physical Review E **70**, 066608 (2004).

[82] Wang, X., Zhang, X.-G., Yu, Q. & Harmon, B. N. *Multiple-scattering theory for electromagnetic waves.* Physical Review B **47**, 4161–4167 (1993).

[83] Yannopapas, V. & Vitanov, N. V. *Electromagnetic Green's tensor and local density of states calculations for collections of spherical scatterers.* Physical Review B **75**, 115124 (2007).

[84] Peterson, A. F., Ray, S. L. & Mittra, R. *Computational Methods for Electromagnetics* (IEEE Press, 1998).

[85] Jørgensen, E., Volakis, J., Meincke, P. & Breinbjerg, O. *Higher order hierarchical Legendre basis functions for electromagnetic modeling.* IEEE Transactions on Antennas and Propagation **52**, 2985–2995 (2004).

[86] Purcell, E. M. & Pennypacker, C. R. *Scattering and absorption of light by nonspherical dielectric grains.* The Astrophysical Journal **186**, 705–714 (1973).

[87] Draine, B. T. & Flatau, P. J. *Discrete-dipole approximation for scattering calculations.* Journal of the Optical Society of America A **11**, 1491–1499 (1994).

[88] Paulus, M. & Martin, O. J. F. *Scattering experiments with a diving cylinder.* Optics Express **9**, 303–311 (2001).

[89] Zhao, L.-M., Wang, X.-H., Gu, B.-Y. & Yang, G.-Z. *Green's function for photonic crystal slabs.* Physical Review E **72**, 026614 (2005).

[90] Martin, O. J. F., Gerard, C. & Dereux, A. *Generalized Field Propagator for Electromagnetic Scattering and Light Confinement.* Physical Review Letters **74**, 526–529 (1995).

[91] Martin, O. J. F., Dereux, A. & Gerard, C. *Iterative scheme for computing exactly the total field propagating in dielectric structures of arbitrary shape.* Journal of the Optical Society of America A **11**, 1073–1080 (1994).

[92] Martin, O. J. F., Gerard, C., Smith, D. R. & Schultz, S. *Generalized Field Propagator for Arbitrary Finite-Size Photonic Band Gap Structures.* Physical Review Letters **82**, 315–318 (1999).

[93] Šolín, P. *Partial Differential Equations and the Finite Element Method* (Wiley Interscience, 2006).

[94] Cowan, A. R. & Young, J. F. *Optical bistability involving photonic crystal microcavities and Fano line shapes.* Physical Review E **68**, 046606 (2003).

[95] Hughes, S. *Quantum emission dynamics from a single quantum dot in a planar photonic crystal nanocavity.* Optics Letters **30**, 1393–1395 (2005).

[96] Hughes, S. *Coupled-Cavity QED Using Planar Photonic Crystals.* Physical Review Letters **98**, 083603 (2007).

[97] Ballentine, L. E. *Quantum Mechanics* (World Scientific, 1998).

[98] Elliott, R. J. *Intensity of Optical Absorption by Excitons.* Physical Review **108**, 1384–1389 (1957).

[99] Dimmock, J. O. *Semiconductors and semimetals Vol. 3. Properties of III-V compounds* (Academic Press, 1967).

[100] Que, W. *Excitons in quantum dots with parabolic confinement.* Physical Review B **45**, 11036–11041 (1992).

[101] Melnik, R. V. N. & Willatzen, M. *Bandstructures of conical quantum dots with wetting layers.* Nanotechnology **15**, 1–8 (2004). URL `http://stacks.iop.org/0957-4484/15/1`.

[102] Markussen, T., Kristensen, P. T., Tromborg, B., Berg, T. W. & rk, J. M. *Influence of wetting-layer wave functions on phonon-mediated carrier capture into self-assembled quantum dots.* Physical Review B **74**, 195342 (2006).

[103] Sugawara, M. *Theory of spontaneous-emission lifetime of Wannier excitons in mesoscopic semiconductor quantum disks.* Physical Review B **51**, 10743–10754 (1995).

[104] Scully, M. O. & Zubairy, M. S. *Quantum Optics* (Cambridge University Press, 1997).

[105] Wubs, M., Suttorp, L. G. & Lagendijk, A. *Multipole interaction between atoms and their photonic environment.* Physical Review A **68**, 013822 (2003).

[106] Jaynes, E. T. & Cummings, F. W. *Comparison of quantum and semiclassical radiation theories with application to the beam maser.* Proceedings of the IEEE **51**, 89–109 (1963).

[107] van de Hulst, H. C. *Light scattering by small particles* (Wiley, 1957).

[108] Watkins, D. S. *Fundamentals of matrix computations, second edition* (Wiley-Interscience, 2002).

[109] Bay, S., Lambropoulos, P. & Mølmer, K. *Atom-atom interaction in strongly modified reservoirs.* Physical Review A **55**, 1485–1496 (1997).

[110] Cheng, S.-C., Wu, J.-N., Tsai, M.-R. & Hsieh, W.-F. *Spontaneous emission near the band edge of a three-dimensional photonic crystal: a fractional calculus approach.* Journal of Physics: Condensed Matter **21**, 015503 (2009).

[111] Yu, P., Beard, M. C., Ellingson, R. J., Ferrere, S., Curtis, C., Drexler, J., Luiszer, F. & Nozik, A. J. *Absorption Cross-Section and Related Optical Properties of Colloidal InAs Quantum Dots.* Journal of Physical Chemistry B **109**, 7084Ű7087 (2005).

[112] Moreels, I., Lambert, K., Muynck, D. D., Vanhaecke, F., Poelman, D., Martins, J. C., Allan, G. & Hens, Z. *Composition and Size-Dependent Extinction Coefficient of Colloidal PbSe Quantum Dots.* Chemistry of Materials **19**, 6101–6106 (2007).

[113] Andreani, L. C., Panzarini, G. & Gérard, J.-M. *Strong-coupling regime for quantum boxes in pillar microcavities: Theory.* Physical Review B **60**, 13276–13279 (1999).

[114] Vats, N. & John, S. *Non-Markovian quantum fluctuations and superradiance near a photonic band edge.* Physical Review A **58**, 4168–4185 (1998).

[115] Li, Z.-Y. & Xia, Y. *Full vectorial model for quantum optics in three-dimensional photonic crystals.* Physical Review A **63**, 043817 (2001).

[116] Ashcroft, N. W. & Mermin, N. D. *Solid State Physics* (Harcourt College Publishers, 1976).

[117] McPhedran, R. C., Botten, L. C., McOrist, J., Asatryan, A. A., de Sterke, C. M. & Nicorovici, N. A. *Density of states functions for photonic crystals.* Physical Review E **69**, 016609 (2004).

[118] Mortensen, N. A., Ejsing, S. & Xiao, S. *Liquid-infiltrated phtotonic crystals: Ohmic dissipation and broadening of modes.* Journal of the European Optical Society - Rapid Publications **1**, 06032 (2006).

[119] Johnson, S. G., Ibanescu, M., Skorobogatiy, M. A., Weisberg, O., Joannopoulos, J. D. & Fink, Y. *Perturbation theory for Maxwell's equations with shifting material boundaries.* Physical Review E **65**, 066611 (2002).

[120] Krokhin, A. A. & Halevi, P. *Influence of weak dissipation on the photonic band structure of periodic composites.* Physical Review B **53**, 1205–1214 (1996).

[121] Gruner, T. & Welsch, D.-G. *Green-function approach to the radiation-field quantization for homogeneous and inhomogeneous Kramers-Kronig dielectrics.* Physical Review A **53**, 1818–1829 (1996).

[122] Dung, H. T., Knöll, L. & Welsch, D.-G. *Spontaneous decay in the presence of dispersing and absorbing bodies: General theory and application to a spherical cavity.* Physical Review A **62**, 053804 (2000).

[123] Keevers, M. & Green, M. *Extended infrared response of silicon solar cells and the impurity photovoltaic effect.* Solar Energy Materials and Solar Cells **41-42**, 195 – 204 (1996).

[124] Kim, S.-H., Kim, S.-K. & Lee, Y.-H. *Vertical beaming of wavelength-scale photonic crystal resonators.* Physical Review B **73**, 235117 (2006).

[125] Prosentsov, V. & Lagendijk, A. *The local density of states in finite size photonic structures, small particle approach.* Photonics and Nanostructures - Fundamentals and Applications **5**, 189–199 (2007).

[126] Tomaš, M. S. *Local-field corrections to the decay rate of excited molecules in absorbing cavities: The Onsager model.* Physical Review A **63**, 053811 (2001).

[127] Dung, H. T., Knöll, L. & Welsch, D.-G. *Efficiency of tunable band-gap structures for single-photon emission.* Physical Review A **69**, 063811 (2004).

[128] Glauber, R. J. & Lewenstein, M. *Quantum optics of dielectric media.* Physical Review A **43**, 467–491 (1991).

[129] Scheel, S., Knöll, L. & Welsch, D.-G. *Spontaneous decay of an excited atom in an absorbing dielectric.* Physical Review A **60**, 4094–4104 (1999).